

# NUMERICAL STUDIES OF DISK FORMATION AROUND LOW-MASS STARS

**Ka Ho Lam**

Hong Kong

B.Sc. Physics, The Chinese University of Hong Kong, 2015  
M.S. Astronomy, University of Virginia, 2018

A Dissertation Presented to the  
Graduate Faculty of the  
*University of Virginia*  
in Candidacy for the Degree of  
*Doctor of Philosophy*

Department of Astronomy

University of Virginia  
August 2022

Committee Members:

Zhi-Yun Li  
Shane W. Davis  
Robin T. Garrod  
David A. Nichols  
L. Ilseadore Cleeves

© Copyright by

Ka Ho Lam

All rights reserved

August 2022

# ABSTRACT

While playing an essential role in star formation and planet formation, the origin of circumstellar disks remains a matter of debate. In particular, circumstellar disks are frequently observed in reality, yet magnetic fields in simulations readily suppress them. In synergies with astronomical observations, analytical and numerical calculations enable us to investigate the process of disk formation from prestellar cores to tens of thousands of years after the birth of the protostars. However, the diversity of the involved astrophysical processes and the wide ranges of length scales over eight orders of magnitude have hindered our attempts to simulate the formation of disks. In this thesis, we first approach the problem with idealized simulations that capture the essential physics. It is followed by using synthetic observation to understand the physics behind actual radio observations of protostars with embedded disks. Lastly, we describe the tools that are built for current and future investigations.

In the first project, we systematically investigate the roles of turbulence and ambipolar diffusion (AD) in the accretion phase of star formation using magnetohydrodynamic (MHD) simulations. We find that both turbulence and AD promote disk formation. In the turbulent simulations, rotationally supported disks form with and without AD. However, the disks formed without AD are strongly magnetized and

short-lived. Turbulence also modifies the appearance of the magnetic field-induced pseudo-disks. The pseudo-disks are warped by turbulence while still staying coherent. In the simulations with AD, the magnetic flux is removed from the disks very efficiently, and the magnetic field lines are less pinched. It results in reduced magnetic braking and promotes disk formation. The disks formed with AD are highly unstable without turbulence. We conclude that turbulence and AD work in parallel to promote disk formation. We measure the plasma- $\beta$  of the disks formed in our simulations. The disks are much more strongly magnetized than commonly assumed in the literature for driving protoplanetary disk accretion.

By comparing radio observations of protostars in the Perseus molecular cloud and the synthetic observations using the previous simulations, we explain the depolarization observed on the disk scale and the alignment of the polarization to the minor axes of the disks. A model is constructed by considering the Larmor precession time-scale, or the grain alignment time-scale, with the gas damping time scale to determine whether the grains are aligned. The vector radiative transfer equation is solved analytically and applied to the simulation to obtain a synthetic polarimetry observation. To reproduce the observed trends, we conclude that both grain dealignment and dust self-scattering must be present.

In the last part of the thesis, we describe three modules implemented in **Athena++** to facilitate a range of current and future studies on star and disk formation. We implement the multipole expansion self-gravity solver to the code in spherical polar coordinates. Using the MacLaurin spheroid as a test, we find that the error converges as more terms in the multipole expansion are used. The error is less than 0.1% when a reasonable number of terms is included in the expansion. The general barotropic equation of state (EOS) and its applications are then discussed. A general form of the multi-power-law equation of state is derived and used to fit a realistic relationship

between temperature and density obtained using complex radiation MHD simulation. Lastly, we describe an implementation of sink particles treatment. This treatment keeps some of the strengths while improving the weaknesses of an existing implementation of sink particles. These modules are used in various projects by collaborators, including astrochemistry of hot cores and first cores, centrifugal barriers in protostellar collapse, and grain growth in disk formation, some of which are briefly described in the thesis.



## ACKNOWLEDGEMENTS

Time flies. I can still remember when Ci and I first got out of the Charlottesville airport six years ago, carrying five pieces of luggage. Of course, I was anxious about my future since all I could lean on was the person next to me. Yet, at the same time, I was also fantasizing about becoming a great scientist after graduating in five years. Well, quite obviously, it didn't work out in the end. It was so close, yet so far. Looking back, I wish I could have done so many things differently, but I also realize I have already achieved a lot. It wasn't my credits, though. I am just blessed to be surrounded by great people who helped me a lot along this journey.

I wanted to start by expressing my gratitude to my advisor, Li. Not only that he is knowledgeable, but he is also patient in teaching me everything. He is also caring and understanding. There had been a very long period when I was spending too much time preparing for job interviews. Even I know that my productivity was far from acceptable. However, he didn't complain once. All he did was support me only for the good of myself. I also messed up many things during my last few years due to procrastination, and I won't be able to graduate if he didn't help me keep track of everything. Thank you, Li.

I would also like to thank all my committee members for their understanding and support. Thank you for spending time reading this thesis that I sent out too late

and gathering together just for my defense. Especially, I wanted to thank Ilse, who agreed to join my committee at the last minute due to unexpected events.

All of my achievements wouldn't be possible if I weren't determined to start this journey. Thanks to everyone in ASIAA who lit up my passion eight years ago. Especially thanks to Ruben, who had been guiding me and helping me with my graduate school application. He had been my role model for a long time, until one point, I knew I couldn't be as great as him.

Thanks to David, Hannah, Luca, Robby, and Yiqing. Although I might not seem to enjoy it, I am still thankful that you guys would keep asking me out. Sometimes, I still miss the time when we gather and bonded together. And I hope we will reunite one day, maybe after I am more comfortable with socializing.

Thanks to everyone who once was in the department for the conversation that we had from time to time. And especially thanks to Bo, Che-Yu, Haifeng, Daniel, Dylan, and Yisheng. It was great collaborating with you. I hope you all have a great future.

Lastly, thank you to everyone that I love. Mom and Dad, although it is unlikely that you will read this, thank you for supporting all my decisions unconditionally, even if it is to leave you alone and fly to the other side of the planet to chase my dream. Thanks to my sisters and brother for taking care of all the issues at home while I am away. I miss all of you. Most importantly, thank you, Ci. It was great meeting you in Taipei eight years ago. Thank you for being around all the time and witnessing the whole journey unfold. Applying to graduate school together and knowing that you will be going to UVa together with me is one of the best moments that I have had in my life. I can't imagine how much worse my life would be without you by my side. Thank you for all the support and tolerance during the preparation of this thesis. Without you, it would never be finished. And thank you for continuing this adventure with me; it has been enchanting.

# TABLE OF CONTENTS

<b>Abstract</b>	<b>iii</b>
<b>Acknowledgements</b>	<b>vii</b>
<b>List of Figures</b>	<b>xx</b>
<b>List of Tables</b>	<b>xxi</b>
<b>I Introduction</b>	<b>1</b>
<b>1 Star Formation Theory</b>	<b>2</b>
1.1 Hydrodynamics . . . . .	4
1.1.1 Time-independent solutions . . . . .	5
1.1.2 Self-similar solutions . . . . .	6
1.2 Radiation Hydrodynamics . . . . .	9
<b>2 Disk Formation Theory</b>	<b>12</b>
2.1 Ideal Magnetohydrodynamics . . . . .	13
2.1.1 Magnetic Braking Catastrophe . . . . .	15
2.2 Non-ideal Magnetohydrodynamics . . . . .	17
<b>3 The Athena Family of Code</b>	<b>19</b>
<b>4 Polarization</b>	<b>21</b>
4.1 Grain Alignment . . . . .	21
4.2 Zeeman Effect . . . . .	23
<b>5 Thesis Overview</b>	<b>25</b>

<b>II</b>	<b>Numerical Simulations of Disk Formation</b>	<b>27</b>
<b>6</b>	<b>Disk Formation in Magnetized Dense Cores with Turbulence and Ambipolar Diffusion</b>	<b>28</b>
6.1	Introduction . . . . .	29
6.2	Problem Setup . . . . .	33
6.2.1	Governing equations . . . . .	33
6.2.2	Numerical method . . . . .	34
6.2.3	Model set-up and parameters . . . . .	36
6.2.4	Numerical code and zoom-in simulations . . . . .	39
6.3	Disk Formation in Ideal MHD: Turbulence . . . . .	40
6.3.1	Warped pseudo-disk . . . . .	43
6.3.2	Enhanced rotation by turbulence . . . . .	47
6.4	Disk Formation in Non-Ideal MHD: Ambipolar Diffusion . . . . .	52
6.4.1	Overview of results . . . . .	53
6.4.2	AD-induced diffusion-DEMS . . . . .	57
6.4.3	Ambipolar diffusion and disk formation . . . . .	63
6.5	Disk Formation with Turbulence and Ambipolar Diffusion . . . . .	66
6.6	Discussion . . . . .	73
6.6.1	How strongly magnetized are protostellar disks? . . . . .	73
6.6.2	Connection with previous work and future refinement . . . . .	80
6.7	Conclusion . . . . .	85
<b>7</b>	<b>The Transition of Polarized Dust Thermal Emission from the Protostellar Envelope to the Disk Scale</b>	<b>88</b>
7.1	Introduction . . . . .	89
7.2	Observational Motivation: Sharp Envelope–Disk Transition in Dust Polarization . . . . .	92
7.3	Condition for Magnetic Grain Alignment . . . . .	96
7.3.1	Larmor precession timescale . . . . .	96
7.3.2	Gas damping timescale . . . . .	98
7.3.3	Condition for magnetic alignment with superparamagnetic Inclusions . . . . .	98
7.4	Modeling Dust Polarization . . . . .	101
7.4.1	Model setup and synthetic observations . . . . .	101
7.4.2	Model results . . . . .	105
7.5	Discussion . . . . .	112
7.6	Summary . . . . .	114
	Appendix 7.A Deprojected Polarization Results for Individual Sources . .	117
	Appendix 7.B Strands in Polarization Fraction–Radius Histograms . . . .	121
	Appendix 7.C Extinction of Polarized Emission . . . . .	123

<b>III</b>	<b>Code Development</b>	<b>127</b>
<b>8</b>	<b>Self-gravity Solver – Multipole Expansion</b>	<b>128</b>
8.1	Mathematical Basis . . . . .	130
8.1.1	Expansion in spherical harmonics . . . . .	130
8.1.2	Implementation . . . . .	131
8.2	Potential of MacLaurin Spheroids . . . . .	132
8.2.1	Analytical solution . . . . .	132
8.2.2	Numerical results . . . . .	133
8.3	Application – Hot Cores . . . . .	135
8.3.1	Accretion phase . . . . .	136
8.3.2	Condensation phase . . . . .	139
8.3.3	Work enabled by self-gravity solver . . . . .	140
<b>9</b>	<b>General Barotropic Equations of State</b>	<b>143</b>
9.1	Implementation . . . . .	144
9.1.1	Stiffened equation of state . . . . .	144
9.1.2	Smoothed multi-power-law equation of state . . . . .	144
9.2	Application – Centrifugal Barrier . . . . .	147
9.2.1	Problem setup and results . . . . .	147
<b>10</b>	<b>Sink Particle Treatment</b>	<b>149</b>
10.1	Design Choice and Implementation . . . . .	150
10.1.1	Creation . . . . .	151
10.1.2	Merging . . . . .	152
10.1.3	Advection and accretion . . . . .	153
10.1.4	Refinement . . . . .	154
10.2	Application – Disk Formation . . . . .	154
<b>IV</b>	<b>Conclusion</b>	<b>159</b>
<b>11</b>	<b>Summary</b>	<b>160</b>
<b>12</b>	<b>Future Work</b>	<b>163</b>
	<b>References</b>	<b>165</b>



# LIST OF FIGURES

1.1	Solution and an approximation to the solution to the Lane–Emden equation. The solution, Bonnor–Ebert sphere (solid) features constant density near the center and $1/r^2$ falloff as the radius increases. The pseudo-Bonnor–Ebert sphere (dashed) provides a good approximation to the solution. . . . .	7
1.2	(Left) B, V, I band (0.44, 0.55, and 0.90 $\mu\text{m}$ ) image of Barnard 68 taken with the Very Large Telescope; (Right) Azimuthally averaged dust extinction profile of Barnard 68 (red circles) and the best-fit Bonnor–Ebert sphere (black solid line). Figures taken from Alves et al. (2001). . . . .	7
2.1	Illustration of magnetic (a) pressure force and (b) tension force. Figure adapted from (Thorne & Blandford, 2021). . . . .	15
4.1	Illustration of the polarization of background starlight (left) and dust thermal radiation (right) due to grain alignment. Figure adapted from Lazarian (2007). . . . .	23
4.2	Magnetic field orientation inferred from the polarization of dust thermal emission and background starlight toward Taurus (top left), Pipe (top right), Lupus I (bottom left), and Musca (bottom right) molecular clouds. The pattern shown in grayscale is the line integral convolution of the magnetic field orientation inferred by rotating the polarization of the dust thermal emission by $90^\circ$ . The black line segments show the magnetic field orientation inferred from the polarization of starlight. Figure taken from Soler et al. (2016). . . . .	24

- 6.1 Column density along  $z$ -axis of the zoom-in simulations of the three ideal MHD models with different levels of turbulence (left to right,  $\mathcal{M} = 0.0, 0.5$  and  $1.0$ ) when the sink particle has accreted  $0.1 M_{\odot}$  (upper row) and  $0.2 M_{\odot}$  (lower). The sink particle is marked by a cross. (See the supplementary material in the online journal for an animated version of the column density distribution for each model. Models M0.0AD0.0 and M1.0AD0.0 are also included in the animated version of Figs 6.6 and 6.11, respectively.) . . . . . 41
- 6.2 Turbulence-induced pseudo-disk warping. Plotted in the top row are the density distributions on a cylinder of radius  $r_{\text{cyl}} = 250$  AU at the epoch when  $M_* = 0.1 M_{\odot}$  for Model M0.0AD0.0 (panel a), M0.5AD0.0 (b), and M1.0AD0.0 (c) as a function of azimuthal angle  $\phi$  (from 0 to  $2\pi$ ) and height  $z$ , showing a more severe warping of the (dense) pseudo-disk by a stronger turbulence. The middle row is for Model M1.0AD0.0 at the same radius as in panel (c) but at different epochs [ $M_* = 0.05$  (d),  $0.15$  (e), and  $0.2 M_{\odot}$  (f)], showing the time evolution of the warped pseudo-disk. The bottom row is also for Model M1.0AD0.0 at the same epoch as in panel (c) but at different cylindrical radii [125 (g), 500 (h), and 1000 au (i)]. . . . . 45
- 6.3 3D view of the turbulence-warped pseudo-disk. Plotted is the isosurface of the normalized density  $\tilde{\rho} = 1$  at an epoch when the stellar mass  $M_* = 0.15 M_{\odot}$  for the ideal MHD sonic turbulence model M1.0AD0.0. The surface is colored by its height above or below the  $x$ - $y$  plane passing through the sink particle (i.e. its  $z$  value). . . . . 46
- 6.4 Distributions of the mass-weighted rotational (upper curves) and infall speeds (lower) in a wedge within  $45^\circ$  of the equatorial plane compared to the Keplerian (upper black dotted line) and free-fall (lower) profile at two representative epochs with stellar mass of  $M_* = 0.1$  (panel a) and  $0.2 M_{\odot}$  (b) for three ideal MHD models with turbulent Mach number of  $\mathcal{M} = 0.0$  (violet solid line),  $0.5$  (green dashed), and  $1.0$  (red dash-dotted). The vertical dotted line in each panel denotes roughly the radius of the sink region. . . . . 49

- 6.5 Reduction of the magnetic flux close to the accreting protostar by turbulence. Plotted are (a) the magnetic flux passing through a circle of 125 AU in radius on the equatorial plane as a function of stellar mass and (b) the dimensionless ratio of the mass enclosed by a sphere of 125 AU in radius (including the stellar mass) and the magnetic flux as a function of the enclosed mass for ideal MHD models of turbulence Mach number  $\mathcal{M} = 0.0$  (violet solid line), 0.5 (green dashed), and 1.0 (red dash-dotted). The dotted line in panel (b) denotes the initial value for the core as a whole  $\lambda_{\text{core}}$  and the upper and lower dashed lines denote, respectively, the mass-to-flux ratio expected under flux freezing in the limit that the stellar mass is accumulated along the (initially vertical) magnetic field lines ( $\lambda_{\text{cyl}}$ ) and that the core collapse into the star is strictly spherical or isotropic ( $\lambda_{\text{sph}}$ ). The star symbol denotes the time of sink particle formation for each model. . . . . 51
- 6.6 Column density along  $z$ -axis of the zoom-in simulations of all non-turbulent AD models with  $Q_{\text{A}} = 0.1\times, 0.3\times, 1\times, 3\times$  and  $10\times$  (left to right) the standard value when the sink particle has accreted 0.1, 0.15, 0.2, 0.25 and  $0.3 M_{\odot}$  (top to bottom). The sink particle is marked by a cross. (See the supplementary material in the online journal for an animated version of the column density distribution for each model.) 55
- 6.7 Distributions of the mass-weighted rotational (upper curves) and in-fall speeds (lower) on the equatorial plane compared to the Keplerian (upper black dotted) and free-fall (lower) profile at five representative epochs with stellar mass of  $M_{*} = 0.1$  (panel a), 0.15 (b), 0.2 (c), 0.25 (d) and  $0.3 M_{\odot}$  (e) for all non-turbulent AD models with  $Q_{\text{A}} = 0.1\times$  (violet solid line),  $0.3\times$  (blue dashed),  $1\times$  (green dash-dotted),  $3\times$  (yellow dash-double-dotted), and  $10\times$  (red dash-triple-dotted) the standard value. The vertical dotted line in each panel denotes roughly the radius of the sink region. . . . . 56
- 6.8 Distribution of the vertical magnetic field on the equatorial plane for the least diffusive model M0.0AD0.1 at the epochs when  $M_{*} = 0.10, 0.15, 0.2, 0.25, 0.3 M_{\odot}$ , showing a distinct strong-field plateau at early epochs, which is disrupted at later epochs. (See the supplementary material in the online journal for an animated version of the vertical magnetic field strength and column density distribution.) . . . . . 59

- 6.9 AD-induced magnetically dominated circumstellar structure in Model M0.0AD0.1 at a representative epoch when  $M_* = 0.15 M_\odot$ . Plotted are the distributions as a function of radius of (a) the azimuthally averaged vertical magnetic field strength ( $B_z$ ) on the equatorial plane, (b) ion and neutral infall speeds weighted by mass, and (c) the radial component of each of the force terms in the momentum equation (equation 6.2), including the flow acceleration (the solid line), magnetic force (dashed), gravity of the central object (dash-dotted), and the gas pressure gradient (dash-double-dotted). Note that a symmetrical log scale is used for the vertical axis of panel (c), where the range  $[-1, 1]$  is in linear scale to highlight the change of flow acceleration to positive values in the transition region around  $r \sim 100$  AU. . . . . 60
- 6.10 Effects of AD on the magnetic field strength and structure, and the magnetic braking efficiency. Plotted are the distributions of (a) the azimuthally averaged vertical magnetic field strength  $B_z$ , (b) the degree of pinching of the magnetic field lines (see equation 6.10 for a definition) in negative  $\phi$ -direction, and (c) the magnetic braking torque  $-\Gamma_z = (1/c)[(\mathbf{J} \times \mathbf{B}) \times \mathbf{r}]_z$ , on the equatorial plane at a representative epoch when  $M_* = 0.15 M_\odot$ . The curves in each panel correspond to the models with  $Q_A = 0.0$  (black solid line), 0.1 (violet dashed), 0.3 (blue dash-dotted), 1.0 (green dash-double-dotted), 3.0 (yellow dash-triple-dotted) and 10.0 (red dash-quadruple-dotted), respectively. 64
- 6.11 Column density along  $z$ -axis of the zoom-in simulations of five sonic-turbulent AD models with  $Q_A = 0.1\times, 0.3\times, 1\times, 3\times$  and  $10\times$  (left to right) the standard value when the sink particle has accreted 0.1, 0.15, 0.2 and  $0.25 M_\odot$  (top to bottom). The sink particle is marked by a cross. (See the supplementary material in the online journal for an animated version of the column density distribution of each model.) . 68
- 6.12 Distributions of the mass-weighted rotational (upper curves) and infall speeds (lower) in a wedge within  $45^\circ$  of the equatorial plane compared to the Keplerian (upper black dotted) and free-fall (lower) profile at five representative epochs with stellar mass of  $M_* = 0.1$  (panel a), 0.15 (b), 0.2 (c) and  $0.25 M_\odot$  (d) for all sonic turbulence AD models with  $Q_A = 0.1\times$  (violet solid line),  $0.3\times$  (blue dashed),  $1\times$  (green dash-dotted),  $3\times$  (yellow dash-double-dotted) and  $10\times$  (red dash-triple-dotted) the standard value. The vertical dotted line in each panel denotes roughly the radius of the sink region. . . . . 69
- 6.13 Turbulence-induced pseudo-disk warping with AD. Plotted are the density distributions on a cylinder of radius  $r_{\text{cyl}} = 250$  AU at the epoch when  $M_* = 0.1 M_\odot$  for Model M1.0AD0.1 (panel a), M1.0AD1.0 (b), and M1.0AD10.0 (c) as a function of azimuthal angle  $\phi$  and height  $z$ , showing a thicker pseudo-disk as the AD coefficient increases. . . . . 72

- 6.14 Distribution of the vertical magnetic field on the equatorial plane (top panels) and the column density (bottom panels) for the weak turbulence and weak AD model (M0.1AD0.1) at the epochs when  $M_* = 0.05, 0.1, 0.15, 0.2, 0.25 M_\odot$ , showing a distinct strong-field plateau at early epochs, which is disrupted at later epochs. (See the supplementary material in the online journal for an animated version of the vertical magnetic field strength and column density distribution.) . . . . . 73
- 6.15 Column density of cells identified as a part of the disk along  $z$ -axis of all non-turbulent AD models with  $Q_A = 0.0\times, 0.1\times, 0.3\times, 1\times, 3\times,$  and  $10\times$  (left to right) the standard value when the sink particle has accreted  $0.1, 0.15, 0.2, 0.25,$  and  $0.3 M_\odot$  (top to bottom). The sink particle is marked by a cross. The number of cells is written on the upper right corner. For those snapshots where either underdeveloped or well-developed disks (with more than 50 disk cells) are identified, the disk mass is shown below the disk cell number in the upper right corner, and the mass-to-flux ratio  $\lambda_d$ , total plasma- $\beta$ , and toroidal component  $\beta_t$  and poloidal component  $\beta_p$  of the plasma- $\beta$  are shown on the lower part of each panel. . . . . 81
- 6.16 Column density of cells identified as a part of the disk along  $z$ -axis of all sonic-turbulent AD models with  $Q_A = 0.0\times, 0.1\times, 0.3\times, 1\times, 3\times,$  and  $10\times$  (left to right) the standard value when the sink particle has accreted  $0.1, 0.15, 0.2,$  and  $0.25 M_\odot$  (top to bottom). The sink particle is marked by a cross. The number of cells is written on the upper right corner. For those snapshots where either underdeveloped disks or well-developed disks are identified, the disk mass is written on the upper right corner, and the mass-to-flux ratio  $\lambda_d$ , total plasma- $\beta$ , and toroidal component  $\beta_t$  and poloidal component  $\beta_p$  of  $\beta$  are written on the lower right corner of each panel. . . . . 82
- 7.1 Trends of observed polarization from envelope to disk scales. Plotted as functions of the deprojected distance from the center (normalized by  $R_{10\text{ percent}}$ ; see text for definition) are the combined distributions of the polarization fraction (*left*) and the orientation of the polarization B-vector (rotated from the E-vector by  $90^\circ$ ; *right*), for 8 of the 10 protostellar systems presented in Cox et al. (2018). The orientation of the polar plot is rotated so that the disk major axes align with the horizontal line. Also, the polar plot is mirror-imaged to reflect the degeneracy of polarization angles over  $180^\circ$ . The polarization fraction is color coded in both panels to highlight its increase from the disk to envelope scale. . . . . 94

- 7.2 (a) A 3D view of the density distribution and magnetic field lines of the simulated protostellar envelope–disk system that is used for the dust polarization modeling. Plotted are the iso-density surfaces at  $n_g = 10^7, 10^8, 10^9, 10^{10} \text{ cm}^{-3}$  (semi-transparent surfaces) and a sample of magnetic field lines, viewed at an angle of  $45^\circ$  to the rotation axis (as in the synthetic polarization maps in the bottom panel and in Fig. 7.3 below). (b) Polarization (B-)vectors (with length proportional to the polarization fraction) superposed on the color map of (mass) column density. . . . . 103
- 7.3 Comparing the four models of synthetic polarization considered in this study. Top to bottom: Model Xi-inf-NoSca, Xi-100-NoSca, Xi-2000-NoSca, and Xi-100-Sca (see Table 7.1 for model parameters). *Left-hand panels:* Maps of total intensity (with mask  $I > 5\sigma_I$ ), overplotted with polarization (B-)vectors (*green segments*), with length proportional to the polarization fraction. Gray contours show the masking boundaries  $P = 3\sigma_P$  adopted when calculating the scatter plots (*middle and right-hand panels*). Black open circles mark the locations of the protostar, and black dashed ellipses represent the disk defined by horizontal position angle and  $45^\circ$  inclination, with size comparable to the contour of 10 percent peak intensity). *Middle and right-hand panels:* scatter plots of polarization fraction (*middle*) and angle (*right*) in the corresponding envelope–disk system, as in Fig. 7.1. The polarization fraction is color coded in both panels. . . . . 106
- 7.4 Face-on view of the spatial distributions (in the  $x - y$  plane) of (a) volume density, (b) the magnetic field strength, and (c) the dimensionless gas alignment parameter  $\lambda$  (see equation 7.7), at the location along each  $z$ -sight line where the density is the highest. The small black circle highlights the location of the sink (stellar) particle in the simulation. Also plotted are the azimuthal average and range of the density and field strength (panel d) and gas alignment parameter  $\lambda$  (panel e) as a function of radius. Note that  $\lambda$  is larger in the disk than in the envelope, indicating that the condition for magnetic alignment is harder to satisfy in the former than in the latter. The grain alignment parameter adopted in Models Xi-100-NoSca and Xi-100-Sca ( $\xi = 100$ ) is shown as the lower dashed horizontal line in panel (e), and that in Model Xi-2000-NoSca ( $\xi = 2000$ ) as the upper dashed line. 110

- 7.A.1 Demonstration of the deprojection and renormalization effects on observation data, using Per 14 as the example. *Left*: total intensity map (in Jy per beam) and polarization (B-)vectors from ALMA Band 7 observation presented in Cox et al. (2018), with outflow directions indicated by blue and red arrows and beam in the lower left corner. The Gaussian-fitted 10 percent peak intensity contour (*purple ellipse*) and the inferred disk adopted in the deprojection process (radius =  $R_{10\text{ percent}}$  and inclination =  $45^\circ$ ; *black dashed ellipse*) are also marked. *Middle and right*: similar to Fig. 7.1 but for the original (*top*), deprojected (*middle*), and deprojected and normalized (*bottom*) data of Per 14. The polarization fraction is color coded, with the color bar shown on the right. . . . . 119
- 7.A.2 Summary of the ALMA Band 7 polarization observations towards the eight protostellar systems investigated in this study (with the exception of Per 14) and the deprojection results. Plotted are the ALMA Band 7 polarization B-vector map (*left column*) superposed on the dust continuum (background color map in Jy per beam with mask  $I > 5\sigma_I$ , outflow direction indicated by red and blue arrows and beam in the lower right corner), the scatter plots of the polarization fraction as a function of the normalized distance (*middle column*; darker color means more pixels), and the scatter plots of the B-vector orientations ( $0^\circ$  for north, *right column*) with the “disk plane” defined from the outflow direction marked as the dashed horizontal cyan line (i.e. the polar plots are rotated so that the position angle of the disk is horizontal). The polarization fraction is color coded, with the color bar shown on the right. . . . . 120
- 7.B.1 Illustration of the origin of the strands seen in the polarization fraction–radius histogram. Plotted are Models Xi-100-Sca with (*top*) and without (*bottom*) Gaussian beam smoothing (without masking) after deprojection. *Left*: 2D histogram of the polarization fraction–radius correlation. *Middle*: polarization fraction plotted against deprojected position angle  $\phi = \arctan 2(y, x)$  at  $r = 200$  (*red*), 250 (*green*) and 300 (*blue*). *Right*: ellipses of constant deprojected radii plotted on a map of azimuthal gradient of polarization fraction  $\partial p/r\partial\phi$ ; contours are at levels  $\pm 10^{-4} \text{ AU}^{-1}$ . The left/right triangle markers mark the region that has small gradient, which corresponds to the origin of the particular strand (see text). The beams used for smoothing are plotted in grey in the bottom-right corner. . . . . 122

8.2.1	L2-norm of the percentage error of the potential of MacLaurin spheroids computed with different $l_{\max}$ . The error of three spheroids with ellipticities $e = 0.9, 0.99, \text{ and } 0.999$ are shown in blue, orange, and green, respectively. The results using coarse and fine grids are shown with solid and dashed lines, respectively. . . . .	134
8.3.1	Snapshot of hot core simulation. The color on the top/bottom three panels shows the density/temperature at different scales. The points on the colored panels are the tracers. The color of the points denotes the tracer type with black, gray, and red representing mass-, space-, and gradient-tracers. The three panels on the right show the history of stellar mass (top), mass accretion rate (center), total luminosity (bottom solid), accretion luminosity (bottom dashed), and stellar luminosity (bottom dotted). . . . .	138
9.1.1	Temperature plotted as a function of density for different EOS fitted or obtained from simulations. The top panel show the “stiffened EOS” fitted from Masunaga et al. (1998) (blue) and “multi-power-law EOS” fitted from Tomida et al. (2013) (orange). The bottom panel shows an EOS obtained using realistic radiation magnetohydrodynamic simulation taken from Tomida et al. (2013). . . . .	145
10.2.1	Edge-on (left) and face-on (right) density slices across the sink particle showing the formation of a first core. The color shows the density in the unit of $5.94 \times 10^{-19} \text{ g cm}^{-3}$ . The sink particle representing the protostar is shown by a circle. . . . .	156
10.2.2	Edge-on (left) and face-on (right) density slices across the sink particle showing the onset of a rotationally supported disk. The color shows the density in the unit of $5.94 \times 10^{-19} \text{ g cm}^{-3}$ . The sink particle representing the protostar is shown by a circle. . . . .	157

# LIST OF TABLES

6.1	Model parameters and outcome. . . . .	38
7.1	Model parameters and outcome. . . . .	105
7.A.1	Deprojection parameters for individual sources. . . . .	121



# Part I

## Introduction

## CHAPTER 1

## STAR FORMATION THEORY

If we spend an hour driving, escape from the city lights, and look up into infinity, usually, we will start counting the thousands of stars that we see. But the longer we stare into it, the more stars appear until we notice a hazy band of light spanning across the whole sky.<sup>1</sup> What we are seeing is the Milky Way, composed of hundreds of billions of stars that our eyes cannot distinguish individually. Although people may find it distant, not only that stars form our galaxy, they are also the factories of the heavy elements that comprise our bodies. Most of the stars are in fact much less massive than our sun. With the advance in our understanding of the origin of stars, we currently know the whole formation process of low-mass stars begins from molecular clouds. Molecular clouds are turbulent, and these turbulent motions redistribute gas and dust unevenly. Thus, high-density regions known as prestellar cores form. As the prestellar cores condense further, they collapse under their own gravity and protostars form at the centers of the cores. Happening in parallel is the rotation of the cores induced by the random motions inherited from their parent clouds. Due to the conservation of angular momentum, the rotation speeds up as the

---

<sup>1</sup>If you are in the northern/southern hemisphere, give it a try in the summer/winter!

cores contract. Eventually, centrifugal forces, which increase faster than gravitational forces as the core collapses, provide enough support and cause the cores to flatten and form circumstellar disks. The accretion phase as well as other later phases quickly follow as the material continues to be accreted from the disks to the central protostars.

While the above picture captures the essence of star formation processes, many details are missing, and star formation remains one of the least understood astrophysical processes. To draw a complete picture, analytical and numerical calculations are often required. However, it is made difficult, if not impossible, by the large range of scale and wide range of physical processes involved. Beginning from giant molecular clouds, to prestellar cores, circumstellar disks, and finally to stars, they have length scales of  $10^6$ ,  $10^4$ ,  $10^2$ , and  $10^{-2}$  AU, respectively; a dynamic range of eight orders of magnitude. Meanwhile, different physical processes including (but not limited to) hydrodynamics, gravitation, electromagnetism, and radiative transfer dominate different phases of the whole process but we are still far from capable of including most processes in a single calculation.

Although technology is quickly catching up, it is usually the simplest and the most idealized model that yields the most intuition. Therefore, in the following, we will start with the most essential physics and then add more pieces to the puzzle in the hope of getting closer to the complete picture. Note that astrophysical fluid dynamics and star formation are wide and deep topics. This introduction is only scratching the surface and is written in a way that builds the basis just enough for understanding the thesis.

## 1.1 HYDRODYNAMICS

Astrophysical flows are well described by compressible Navier-Stokes equations. They are composed of the continuity equation

$$\frac{\partial \rho}{\partial t} + \nabla \cdot (\rho \mathbf{v}) = 0, \quad (1.1)$$

and the momentum equations

$$\frac{\partial \rho \mathbf{v}}{\partial t} + \nabla \cdot (\rho \mathbf{v} \mathbf{v} + P) = -\rho \nabla \Phi_g, \quad (1.2)$$

where  $\rho$  is the gas (or fluid) mass density,  $\mathbf{v}$  is the velocity,  $P$  is the pressure, and  $\Phi_g$  is the gravitation potential caused by the gas itself. In general, the pressure is a function of both the mass density and the internal energy density, which requires solving an additional energy equation. However, for the reasons that will be discussed in the next section, the temperature of molecular clouds is nearly constant at  $\sim 10$  K, corresponding to an isothermal sound speed  $c_s$  of  $\sim 0.2 \text{ km s}^{-1}$ . Therefore, for simplicity, we will adopt the isothermal equation of state (EOS), i.e.

$$P = \rho c_s^2. \quad (1.3)$$

The gravitational potential can be obtained by solving Poisson's equation

$$\nabla^2 \Phi_g = 4\pi G \rho. \quad (1.4)$$

While the detailed numerical method for solving equation (1.4) will be presented in Chapter 8, it can be treated as a given quantity in the current context.

Prestellar cores can be modeled as a sphere of self-gravitating gas. Assuming all quantities are spherically symmetric, we can write them in terms of only radial distance  $r$  and time  $t$ . In this case, the equations become

$$\begin{aligned}\frac{\partial \rho}{\partial t} + \frac{1}{r^2} \frac{\partial (r^2 \rho v_r)}{\partial r} &= 0, \\ \frac{\partial v_r}{\partial t} + v_r \frac{\partial v_r}{\partial r} &= -\frac{c_s^2}{\rho} \frac{\partial \rho}{\partial r} - \frac{\partial \Phi_g}{\partial r}, \\ \frac{1}{r^2} \frac{\partial}{\partial r} \left( r^2 \frac{\partial \Phi_g}{\partial r} \right) &= 4\pi G \rho.\end{aligned}\tag{1.5}$$

In the following, we will discuss a solution for hydrostatic isothermal cores in Subsection 1.1.1 and a self-similar solution for isothermal flow in Subsection 1.1.2, respectively.

### 1.1.1 Time-independent solutions

The solution for hydrostatic cores can be obtained by substituting  $v_r = 0$  and  $\partial/\partial t = 0$ . After rearranging, the momentum equation becomes

$$\frac{1}{\rho} \frac{d\rho}{dr} = -\frac{1}{c_s^2} \frac{d\Phi_g}{dr},\tag{1.6}$$

which, if  $\Phi_g(r=0) = 0$  is assumed, results in

$$\begin{aligned}\rho &= \rho_c e^{-\Phi_g/c_s^2}, \\ \frac{1}{r^2} \frac{d}{dr} \left( r^2 \frac{d\Phi_g}{dr} \right) &= 4\pi G \rho_c e^{-\Phi_g/c_s^2},\end{aligned}\tag{1.7}$$

where  $\rho_c = \rho(r=0)$  is the central density. Finally, we can obtain the Lane–Emden equation

$$\frac{1}{\xi^2} \frac{d}{d\xi} \left( \xi^2 \frac{d\psi}{d\xi} \right) = e^{-\psi}\tag{1.8}$$

by defining

$$\psi \equiv \frac{\Phi_g}{c_s^2}, \quad \xi \equiv \left( \frac{4\pi G \rho_c}{c_s^2} \right)^{1/2} r. \quad (1.9)$$

The solution to the Lane–Emden equation as shown with a solid line in Fig. 1.1 is known as the Bonnor–Ebert sphere (Bonnor 1956; Ebert 1955), characterized by the constant density at small radii and the approximately  $1/r^2$  density falloff. It is not just a theoretical calculation that exists on paper. In fact, the density structure of Barnard 68 (Fig. 1.2) inferred from infrared observations shows a remarkable agreement with the theoretical solution (Alves et al. 2001). Also note that this solution can very well be approximated by the so-called pseudo-Bonnor–Ebert sphere  $\rho/\rho_c = (1 + \xi^2/2)^{-1}$  shown with dashed line in Fig. 1.1 and both profiles are frequently adopted as the initial conditions of numerical simulations (e.g. Chapter 6).

### 1.1.2 Self-similar solutions

Bonnor–Ebert sphere is not the only solution to the Lane–Emden equation; it can be shown that  $\rho \propto 1/r^2$  also satisfies the equation. In fact, this profile, which is known as singular isothermal sphere (Shu 1977), is a special case of a solution to a more general problem. If we start again from equations (1.5) and follow Shu (1977), we can write another quantity  $M$ , the total mass inside a certain radius, in terms of density:

$$\frac{\partial M}{\partial r} = 4\pi r^2 \rho. \quad (1.10)$$

The equations to be solved become

$$\begin{aligned} \frac{\partial M}{\partial t} + u \frac{\partial M}{\partial r} &= 0, & \frac{\partial \rho}{\partial t} + \frac{1}{r^2} \frac{\partial (r^2 \rho u)}{\partial r} &= 0, \\ \frac{\partial u}{\partial t} + u \frac{\partial u}{\partial r} &= -\frac{c_s^2}{\rho} \frac{\partial \rho}{\partial r} - \frac{GM}{r^2}. \end{aligned} \quad (1.11)$$

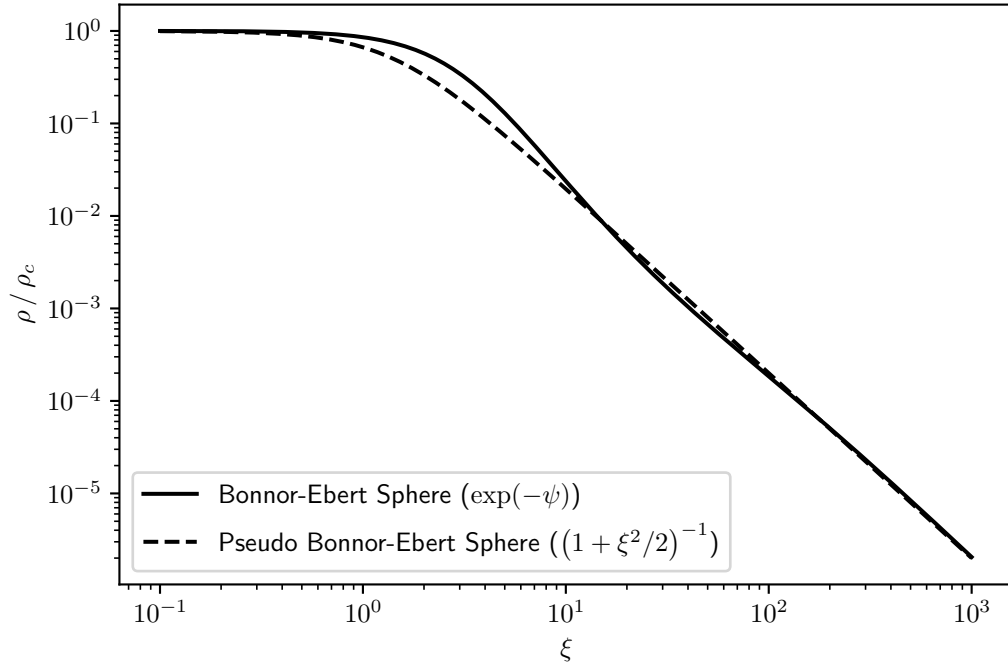


Figure 1.1: Solution and an approximation to the solution to the Lane–Emden equation. The solution, Bonnor–Ebert sphere (solid) features constant density near the center and  $1/r^2$  falloff as the radius increases. The pseudo-Bonnor–Ebert sphere (dashed) provides a good approximation to the solution.

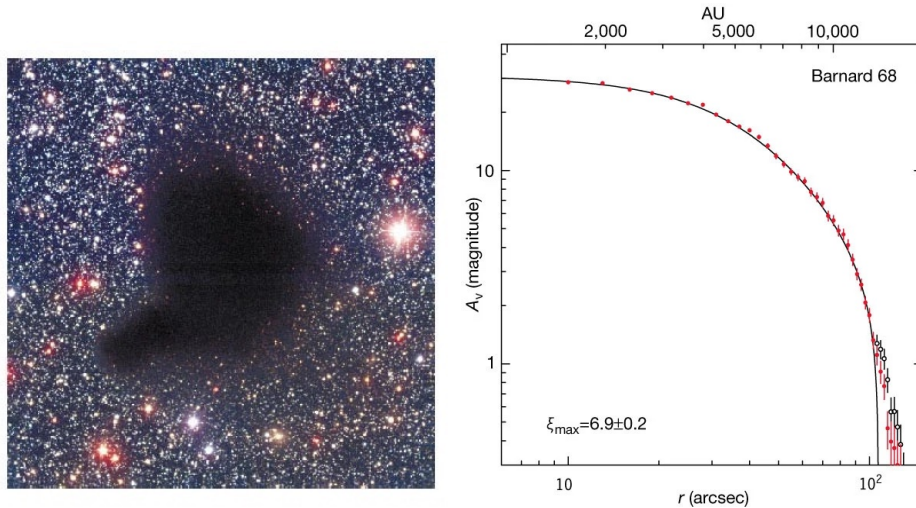


Figure 1.2: (Left) B, V, I band ( $0.44$ ,  $0.55$ , and  $0.90 \mu\text{m}$ ) image of Barnard 68 taken with the Very Large Telescope; (Right) Azimuthally averaged dust extinction profile of Barnard 68 (red circles) and the best-fit Bonnor–Ebert sphere (black solid line). Figures taken from Alves et al. (2001).

We can then non-dimensionalize the quantities using

$$x = \frac{r}{c_s t}, \quad M = \frac{c_s^3 t}{G} m(x), \quad \rho = \frac{1}{4\pi G t^2} \alpha(x), \quad u = c_s v(x). \quad (1.12)$$

After some manipulation, one should get

$$\begin{aligned} m &= x^2 \alpha(x - v), \\ [(x - v)^2 - 1] v' &= \left[ \alpha(x - v) - \frac{2}{x} \right] (x - v), \\ [(x - v)^2 - 1] \frac{1}{\alpha} \alpha' &= \left[ \alpha - \frac{2}{x} (x - v) \right] (x - v), \end{aligned} \quad (1.13)$$

which can be solved using power series of  $1/x$  to obtain asymptotic solutions for  $x \gg 1$ :

$$\begin{aligned} \alpha &= Ax^{-2} - \frac{A(A-2)}{2} x^{-4} + \dots, \\ v &= -(A-2)x^{-1} + \frac{(A-2)(A-6)}{6} x^{-3} + \dots. \end{aligned} \quad (1.14)$$

Finally, we can find that, by substituting  $t \rightarrow 0$ , the initial density is indeed proportional to  $1/r^2$  with an initial zero velocity. Since the solution is written in terms of  $x$ , a dimensionless quantity, the solution is self-similar. There are lots of interesting properties of the solution. The constant  $A$  determines whether the profile is stable against gravitational collapse: the solution describes an inside-out collapse with an expansion wave propagating at the isothermal sound speed when  $A > 2$ . By putting  $r \rightarrow 0$ ,  $M$  represents the mass of the central ‘‘protostar’’, which increases linearly with time. When  $A$  is just above the critical value 2, the solution has an accretion rate of  $0.975 c_s^3/G = 1.85 \times 10^{-6} M_\odot \text{ yr}^{-1} (c_s/0.2 \text{ km s}^{-1})^3$ , implying an lower limit on rate an actual star accretes. Also, the constant accretion rate is sometimes a useful property. In Section 8.3, we describe one of the applications that uses a singular isothermal sphere as the initial condition.

## 1.2 RADIATION HYDRODYNAMICS

In the last section, we assume the pressure is always proportional to the density, which is equivalent to an isothermal assumption. In this section, we will relax the restriction and reestablish why and when it is a valid approximation.

Recall that pressure should be a function of density and internal energy. Obtaining the internal energy requires solving the energy equation. An energy equation reads

$$\frac{\partial E}{\partial t} + \nabla \cdot [(E + P) \mathbf{v}] = -\rho \mathbf{v} \cdot \nabla \Phi_g + \mathcal{H} - \Lambda, \quad (1.15)$$

where  $E = e + \rho v^2/2$  is the total energy density of the fluid with  $e$  as the internal energy density, and  $\mathcal{H}$  and  $\Lambda$  are the heating and cooling terms, respectively. In molecular clouds and prestellar cores, the main source of heating is cosmic-ray heating while molecular lines and dust (thermal) radiation are responsible for the cooling. In prestellar cores, the density is high enough for dust and gas to be well-coupled (Goldsmith 2001) and dust cooling usually dominates. The dust cooling time-scale at 10 K is  $\sim 10^2$ – $10^3$  year, much shorter than the mechanical time-scale (e.g. the free-fall time of prestellar cores is  $\sim 10^4$ – $10^5$  year), so it is safe to ignore the mechanical heating/cooling terms when determining the equilibrium temperature, and it is safe to simply consider the balance between  $\mathcal{H}$  and  $\Lambda$ . Compared to that of cosmic-ray heating, the temperature dependence of dust radiation cooling is very steep ( $\propto T^4$ ); even if the gas temperature is only slightly out of equilibrium, the heating and cooling terms would be greatly unbalanced and the temperature would return to equilibrium within a short time-scale.

The argument above, however, only holds when the prestellar cores are optically thin to their own radiation. As the core contracts, the density as well as the optical

depth increases, which makes cooling inefficient. As a result, an adiabatic core forms at the center. With the enhanced gas pressure, the adiabatic core would be able to support itself against gravity. Hence, it is also known as the first hydrostatic core. As the central temperature increases and reaches about 2000 K, dissociation of hydrogen molecules, an endothermic process, begins, which weakens the thermal support and triggers the second collapse. Once the dissociation completes, the gas temperature rises rapidly again, the ionization of hydrogen begins, and the second hydrostatic core, or the protostellar core, forms.

Simulating the adiabatic cores requires solving additional equations as radiation becomes significant. The radiative transfer equation is

$$\frac{\partial I_\nu}{\partial t} + c\mathbf{n} \cdot \nabla I_\nu = S_\nu(I_\nu, \mathbf{n}), \quad (1.16)$$

where  $S_\nu(I_\nu, \mathbf{n})$  is the source term encompassing both absorption and emission. This equation is notorious for being hard to solve because of the dependence of specific intensity  $I_\nu$  on not only location, but also direction angle and frequency. Nonetheless, one can reduce its complexity by taking the grey approximation or by integrating over frequency, assuming local thermal equilibrium is attained. We end up with the radiation hydrodynamic equations

$$\begin{aligned} \frac{\partial \rho}{\partial t} + \nabla \cdot (\rho \mathbf{v}) &= 0, \\ \frac{\partial \rho \mathbf{v}}{\partial t} + \nabla \cdot (\rho \mathbf{v} \mathbf{v} + P) &= -\rho \nabla \Phi_g - \mathbf{G}_r, \\ \frac{\partial E}{\partial t} + \nabla \cdot [(E + P) \mathbf{v}] &= -\rho \mathbf{v} \cdot \nabla \Phi_g - G_r^0 + \rho \epsilon_{\text{CR}}, \\ \frac{\partial I}{\partial t} + c\mathbf{n} \cdot \nabla I &= S(I, \mathbf{n}) \end{aligned} \quad (1.17)$$

after including radiative force  $\mathbf{G}_r$  and net heating/cooling rate  $G_r^0$  that couple the

radiation and hydrodynamic equations, and the cosmic-ray heating rate per unit mass of gas  $\epsilon_{\text{CR}}$ . To relate gas pressure and internal energy density, for simplicity, we can use the ideal gas law

$$e = \frac{P}{\gamma - 1}, \quad (1.18)$$

where  $\gamma$  is the adiabatic index. The source term in the radiative transfer equation is defined as

$$S(I, \mathbf{n}) = c\rho \left[ \kappa_{\text{a,P}} \left( \frac{ca_{\text{r}}T^4}{4\pi} - J \right) + \kappa_{\text{a,R}} (J - I) \right], \quad (1.19)$$

where  $\kappa_{\text{a,P}}$  and  $\kappa_{\text{a,R}}$  are the Planck and Rosseland mean absorption opacity, respectively,  $J = \int I d\Omega/(4\pi)$  is the angular quadrature of the intensity (i.e., the mean intensity)..

Indeed, solving a similar set of equations, Masunaga & Inutsuka (2000) shows that the first core starts forming when the central density reaches  $\sim 10^{-13} \text{ g cm}^{-3}$ . At  $\sim 10^{-7} \text{ g cm}^{-3}$ , the central temperature reaches  $\sim 2000 \text{ K}$  and the second collapse begins. And finally, the second core forms  $\sim 0.1$  year after the second collapse begins. Unfortunately, due to the short time-scale of first cores and that they are deeply embedded, there is still no direct evidence for these theoretically predicted structures so far.

## CHAPTER 2

## DISK FORMATION THEORY

Being a natural consequence of the conservation of angular momentum, circumstellar disks play a critical role in the later stages of star formation. The rotation of prestellar cores is believed to be inherited from their turbulent parent molecular clouds; although there is only a negligible amount of net angular momentum in the molecular clouds, a locally non-zero net angular momentum within the clouds can contribute to the rotation of prestellar cores. By observing spectral lines, we can obtain kinematic information about these prestellar cores. Statistically, a core would have a rotational energy that is about 2% of the gravitational binding energy (i.e.  $\beta_{\text{rot}} = 2\%$ , Goodman et al. 1993). As the cores contract, due to conservation of angular momentum, their angular speed and, thus, the centrifugal support is significantly amplified. At some point, the rotational support would be large enough to halt the gravitational collapse and circumstellar disks are formed around the protostars.

To get a sense of how large a disk would be, we can consider the balance between rotational and gravitational energies. If we assume the specific angular momentum  $l \sim L/M$  is conserved, the rotational energy would be  $\sim L^2/(MR^2) \sim l^2 M/R^2 \propto R^{-2}$ . On the other hand, the gravitational energy is  $\sim GM^2/R \propto R^{-1}$ , increases slower than

the rotational energy as  $R$  decreases. When  $R$  decreases to  $\beta_{\text{rot}} = 2\%$  of the original size, the rotational energy catches up with the gravitational energy and, assuming a core size of  $\sim 10^4$  AU, the expected disk size would be  $\sim 10^2$  AU.

However, it brings a problem that, if the angular momentum of each gas parcel is perfectly conserved, none of them would be able to arrive at the centers of prestellar cores and stars would be unable to form. Therefore, there have to be ways to redistribute angular momentum. In hydrodynamic simulations, the resultant circumstellar disks are usually very massive and unstable due to Toomre's (1964) instability. Spirals can develop from the disks and angular momentum can be transported through gravitational torque. The material with angular momentum removed would be able to be accreted by the protostars. Whether the disk can accrete at a high enough rate to avoid mass accumulation and fragmentation is unclear. Other physical processes to enable disk accretion may be needed.

## 2.1 IDEAL MAGNETOHYDRODYNAMICS

In fact, the molecular cloud is partially ionized by cosmic rays and threaded by magnetic field lines. Although neutral particles cannot experience the electromagnetic (EM) forces directly, when charged particles, which are tied to magnetic fields, are accelerated by EM forces relative to the neutral particles, the EM forces would be transferred to the neutrals through collisions. These charged particles are also fairly well-coupled to the neutrals due to the fact that the magnetic diffusion timescale is usually much longer than the dynamical timescale. As the consequence, like most fluids of astrophysical interest, the gas in the molecular cloud to the zeroth order acts like a perfectly conducting plasma and can be described by ideal magnetohydrodynamics (MHD). Ideal MHD introduces the induction equation and couples it to hydrodynamics by adding the Lorentz force terms to the momentum and energy

equation. Specifically,

$$\begin{aligned}
\frac{\partial \rho}{\partial t} + \nabla \cdot (\rho \mathbf{v}) &= 0, \\
\frac{\partial \rho \mathbf{v}}{\partial t} + \nabla \cdot \left( \rho \mathbf{v} \mathbf{v} + P + \frac{B^2}{8\pi} - \frac{\mathbf{B} \mathbf{B}}{4\pi} \right) &= -\rho \nabla \Phi_g, \\
\frac{\partial E}{\partial t} + \nabla \cdot \left[ \left( E + P + \frac{B^2}{8\pi} \right) \mathbf{v} - \frac{\mathbf{B} (\mathbf{B} \cdot \mathbf{v})}{4\pi} \right] &= -\rho \mathbf{v} \cdot \nabla \Phi_g, \\
\frac{\partial \mathbf{B}}{\partial t} - \nabla \times (\mathbf{v} \times \mathbf{B}) &= 0.
\end{aligned} \tag{2.1}$$

Here, the Lorentz force, which is usually written in the form of  $(\nabla \times \mathbf{B}) \times \mathbf{B}/4\pi$ , is decomposed into two terms: the magnetic pressure term  $-\nabla B^2/8\pi$  and the magnetic tension term  $\nabla \cdot \mathbf{B} \mathbf{B}/4\pi = (\mathbf{B} \cdot \nabla) \mathbf{B}/4\pi$ . The magnetic tension term vanishes when the magnetic field has no variation along the field line, or in other words, magnetic tension is non-zero if and only if the field lines have a curvature. In absence of other forces, the magnetic field line tends to redistribute such that the force vanishes. Therefore, we can see that magnetic tension tends to straighten field lines. With a similar argument, but this time the magnetic pressure term vanishes only when the magnetic field strength is uniform, we see that magnetic pressure tends to spread out field lines such that they are uniform, as illustrated in Fig. 2.1. Therefore, materials move preferentially along the field lines, or otherwise, there will be a resistive force acted by the bent magnetic field.

Under the ideal MHD or the flux-freezing approximation, the dimensionless mass-to-flux ratio is useful when the interplay between gravity and the magnetic field is of interest. The dimensionless mass-to-flux ratio of a structure, as the name suggests, is the ratio between the mass and the magnetic flux threaded through it, normalized by the critical value:

$$\lambda = 2\pi\sqrt{G}\frac{M}{\Phi}, \tag{2.2}$$

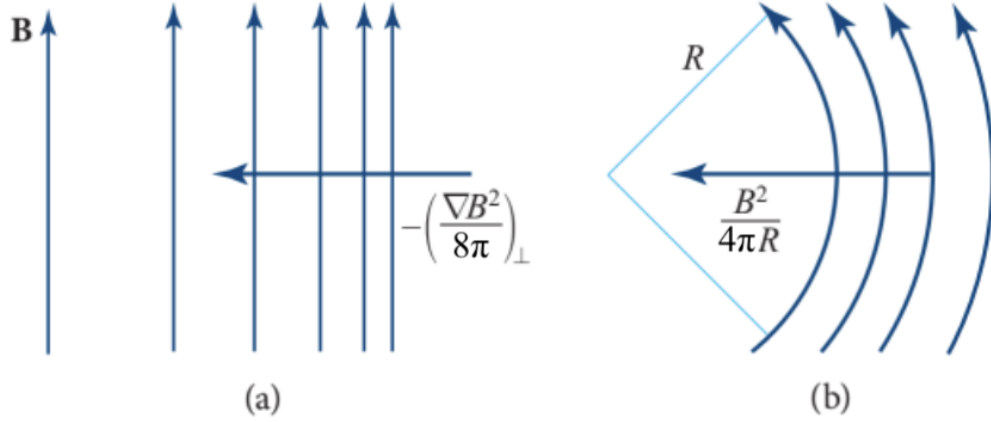


Figure 2.1: Illustration of magnetic (a) pressure force and (b) tension force. Figure adapted from (Thorne & Blandford, 2021).

where  $\Phi$  is the magnetic flux, and  $(2\pi\sqrt{G})^{-1}$  is the critical value above which gravitational instability can happen (Nakano & Nakamura 1978), i.e. a structure is stable against gravitational collapse when  $\lambda < 1$ , and vice versa. Through Zeeman observations of prestellar cores, Troland & Crutcher (2008) constrain the typical mass-to-flux ratio. After applying the correction for the projection of the underlying geometry of the cores, the authors found the mass-to-flux ratios to be close to unity ( $\lambda \approx 2.6$ ); meaning that gravity is just slightly stronger than the magnetic force.

### 2.1.1 Magnetic Braking Catastrophe

It turns out the result is catastrophic if we simulate the formation of a magnetized disk with the observed parameters in a way that is the most idealized. The simulation starts with a protostellar core of one solar mass and  $\sim 10^4$  AU with an arbitrary density profile, for example, a Bonnor–Ebert sphere. The core is initially threaded by a uniform magnetic field with a mass-to-flux ratio  $\lambda \gg 1$  and starts with a solid-body rotation such that  $\beta_{\text{rot}}$  is a few percent. In the beginning, since the magnetic field is straight and uniform, there is not any magnetic force acting on the gas, and the core

proceeds to contract isotropically. As soon as the magnetic field lines become slightly bent, the magnetic field exerts a force that resists the infall perpendicular to the field lines and causes the gas to flow preferentially along the field lines. Therefore, the core is flattened along the field lines, forming the so-called pseudo-disk (Galli & Shu 1993). As the cores are flattening, the gas along a certain field line closest to the mid-plane would feel the strongest gravitational pull. Therefore, it is pulled into the center much quicker than the others, causing the pull to be even stronger, and hence, heavily pinches the magnetic field line toward the center. As in hydrodynamic simulation, due to the conservation of angular momentum, the rotation of the gas at the mid-plane is amplified compared to the rest in the same flux tube, causing the field lines to twist slightly in the direction of the rotation. Recall that Lorentz force has two components: tension and pressure. Due to axisymmetry, the magnetic pressure would only exert a radial force and has no effect on angular momentum. The tension force, however, is exerted on the gas at the mid-plane, resisting the rotation. Note that angular momentum is always conserved; the removed angular momentum is transported to the rest of the material on the flux tube, driving an outflow that carries away angular momentum. This process is very efficient and is able to completely suppress disk formation, leading to the magnetic braking catastrophe (Galli et al. 2006).

As will be introduced in Section 6.1, the potential resolutions fall into three categories: non-ideal MHD effects, turbulence, and field-rotation misalignment. Studies including these effects will be presented in Chapter 6, and they suggest that non-ideal MHD effects are the most promising. Therefore, it is useful to provide an overview of non-ideal MHD.

## 2.2 NON-IDEAL MAGNETOHYDRODYNAMICS

Non-ideal MHD effects arise due to disks being only lightly ionized. They include Ohmic dissipation, Hall effect, and ambipolar diffusion (AD); each of them dominates a different regime. Roughly, in regions with increasing density, AD, Hall effect, and Ohmic dissipation dominate in the order given. In the circumstellar disks that this thesis studies, AD is the most effective among the three. AD relaxes the assumption that charged particles are perfectly coupled to the bulk neutral materials; instead, the charged particles (or ions) that are tied to the magnetic field can slip through the gas, causing the magnetic flux to be released from the gas.

To formulate AD, we can first start by writing down the drag force acting on the neutrals by the ions

$$\mathbf{F}_{\text{drag}} = \gamma \rho \rho_i (\mathbf{v}_i - \mathbf{v}), \quad (2.3)$$

where  $\gamma = \langle w \sigma \rangle / (m + m_i)$  is the drag coefficient,  $w$  is the relative velocity between ions and neutrals, and  $m$  and  $m_i$  are the mass of the neutrals and ions, respectively. In the frame of neutrals, the only forces experienced by the ions are the drag force and the Lorentz force. The two forces must be equal since, otherwise, the ions would be accelerated until the drag force balance the Lorentz force. So we can write

$$\begin{aligned} \gamma \rho \rho_i (\mathbf{v}_i - \mathbf{v}) &= \frac{1}{4\pi} (\nabla \times \mathbf{B}) \times \mathbf{B}, \\ \mathbf{v}_i &= \mathbf{v} + \frac{1}{4\pi \gamma \rho \rho_i} (\nabla \times \mathbf{B}) \times \mathbf{B}. \end{aligned} \quad (2.4)$$

Since the magnetic field is tied to the ions instead of the neutrals, we should write the induction equation as

$$\frac{\partial \mathbf{B}}{\partial t} - \nabla \times (\mathbf{v}_i \times \mathbf{B}) = 0. \quad (2.5)$$

Eliminating  $\mathbf{v}_i$ , we get

$$\frac{\partial \mathbf{B}}{\partial t} - \nabla \times (\mathbf{v} \times \mathbf{B}) - \nabla \times \left( \frac{1}{4\pi\gamma\rho\rho_i} (\nabla \times \mathbf{B}) \times \mathbf{B} \times \mathbf{B} \right) = 0. \quad (2.6)$$

Note that  $\mathbf{a} \times \hat{\mathbf{e}} \times \hat{\mathbf{e}}$  gives the component of an arbitrary vector  $\mathbf{a}$  that is perpendicular to the unit vector  $\hat{\mathbf{e}}$ , the induction equation becomes

$$\begin{aligned} \frac{\partial \mathbf{B}}{\partial t} - \nabla \times (\mathbf{v} \times \mathbf{B}) + \nabla \times (\eta_{\text{AD}} (\nabla \times \mathbf{B})_{\perp}) &= 0, \\ \eta_{\text{AD}} &= \frac{B^2}{4\pi\gamma\rho\rho_i}, \end{aligned} \quad (2.7)$$

where  $\mathbf{a}_{\perp}$  denote the perpendicular component of  $\mathbf{a}$  to  $\mathbf{B}$ .

## CHAPTER 3

## THE ATHENA FAMILY OF CODE

Since this thesis focuses on the application and development of the **Athena** family of code (Stone et al. 2008, 2020), this chapter provides an overview of **Athena** and its successor, **Athena++**. **Athena** is a grid-based code that solves the MHD equations. The code is designed for the studies of astrophysical flows, and is capable of solving compressible hydrodynamics and MHD with a wide range of physics in one-, two-, and three-dimension. In short, **Athena** solves the partial differential equations (PDEs) in a fixed computational domain. The domain is discretized into (cubic) cells, with each cell initialized with the initial condition. The PDEs are also discretized by the finite difference method in both time and space, and are used to evolve the fluid quantities to the next time-step.

Succeeding **Zeus**,<sup>1</sup> **Athena** inherited the strength of **Zeus** while still having quite a few improvements. Different from **Zeus**, **Athena** uses directionally-unsplit, high-order Godunov method; in each time-step, **Athena** solves individual Riemann problem at the cell interfaces and integrates the equations in the conservative form. Similar to **Zeus**, **Athena** is particularly great at maintaining the divergence-free condition ( $\nabla \cdot$

---

<sup>1</sup>In Greek mythology, Athena is the daughter of Zeus who sprang out from his head.

$\mathbf{B} = 0$ ); it evolves the magnetic field using constrained transport (CT, Evans & Hawley 1988). At each time-step, the electromagnetic force and current are calculated at the edges of each cell interface. They are used to integrate the induction equation and update the magnetic flux threading through each cell interface, analogous to evolving the fluid quantities using fluxes.

To overcome the numerical difficulties caused by the large dynamic range of astrophysical flows, static mesh refinement (SMR) has been implemented in **Athena**. SMR works by dividing the computational domain into multiple ones. Some of them where the flows are expected to be smoother would be tiled by coarser cells, while others where interesting finer structures happen would be refined and tiled by finer cells. Unfortunately, due to the difficulties in maintenance, not all pieces of physics are compatible with SMR. With the latest version of 4.2, **Athena** is deprecated in 2013. The team then started the development of the successor **Athena++**. **Athena++** is an adaptive mesh refinement (AMR) framework designed to make the development of AMR-compatible physics modules more manageable. The MHD solvers behind **Athena++** is completely based on **Athena**. **Athena++** is written in C++ and with performance in mind. The integrator is so-called task-based. It allows tasks to be performed out-of-order so that MPI (message passing interface) communication (an I/O-bound task required for distributed parallelism) can be overlapped with computationally-expensive tasks. **Athena++** is currently more capable than **Athena** in almost every way, and is quickly adopted by the community. Active development has been undergoing and some of which will be discussed in Part III.

## CHAPTER 4

# POLARIZATION

The information on the magnetic field is critical to the study of star formation. However, obtaining this information from observation has been challenging since magnetic fields are hard to be observed directly. Therefore, techniques such as Chandrasekhar–Fermi method (Chandrasekhar & Fermi 1953) and velocity gradient technique (González-Casanova & Lazarian 2017) have been developed for this purpose. It turns out that magnetic fields have effects on both linear dust continuum polarization and circular line polarization due to grain alignment and Zeeman effect, respectively. In the following, we will first introduce grain alignment and the complication due to scattering. Following that, we briefly discuss Zeeman effect, the basis of anchoring mass-to-flux ratios.

### 4.1 GRAIN ALIGNMENT

Although the main ingredient of the molecular cloud is molecular hydrogen, there are also dust grains, tiny solid particles accounting for about 1% of the total mass (Frisch et al. 1999). Composed of mainly carbon and silicates, dust grains have sizes ranging from a few angstroms up to about a micron (Draine 2011). Through collision

and sticking, dust grains can grow until they are large enough to attract each other through gravity and eventually form planets. On top of that, dust grains are also responsible for emitting, absorbing, and scattering radiation. In general, dust grains are not spherical and have rotation usually aligned to their shortest axes. Barnett (1915) discovered that dust grains would spontaneously magnetize, and in the presence of a background magnetic field, would precess around and slowly align to the background magnetic field.

This alignment affects polarization because of the dichroic absorption and emission of elongated dust grains. In particular, polarized radiation with  $E$  vectors aligned with the shortest axis is less likely to be absorbed and emitted. The resultant polarization depends on whether the radiation is contributed by the background starlight or the dust thermal emission. In the former case, starlight, resulting from black body radiation, is unpolarized at first. However, as it passes through dust grains along the line of sight, one component gets extinguished more effectively than the other, resulting in polarized radiation with  $E$  vectors aligned to the magnetic field. In the latter case, the thermal radiation is already polarized in the first place and has the opposite orientation. As illustrated in Fig. 4.1, linear polarization either parallel or perpendicular to the magnetic field is produced, allowing us to trace the magnetic field orientation and morphology, and in turn, to measure the magnetic field strength using methods like the histogram of relative orientation (Soler et al. 2013). Fig. 4.2 presents some examples of magnetic field orientation inferred from both the polarization of background starlight and dust thermal radiation. The inferred orientation is strikingly consistent.

However, grains do not always align to magnetic fields, especially in circumstellar disks as discussed in Chapter 7. Further complicating matters is the fact that grain alignment is not the only mechanism responsible for linear polarization; an-

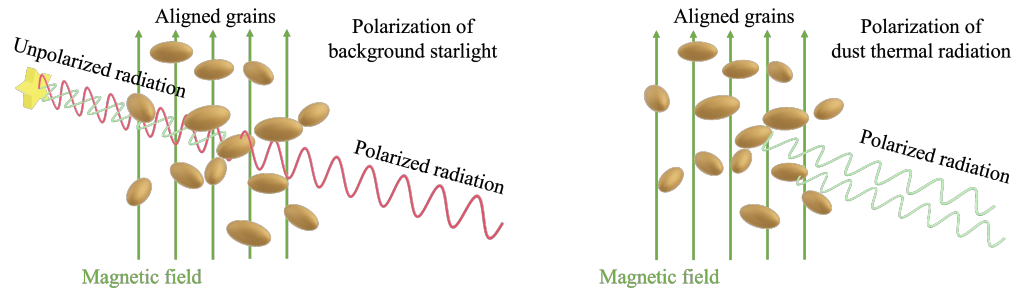


Figure 4.1: Illustration of the polarization of background starlight (left) and dust thermal radiation (right) due to grain alignment. Figure adapted from Lazarian (2007).

other mechanism is self-scattering in disks (Kataoka et al. 2015; Yang et al. 2016). The details behind the mechanism are out of the scope of this thesis. Briefly, the polarization of scattered light is a function of scattering angle. As a result of the disk inclination and emission profile, the scattered light is polarized with  $E$  vectors aligned to disk minor axes, independent of magnetic fields.

## 4.2 ZEEMAN EFFECT

As the only method of measuring the magnetic field strength directly (Crutcher 2012), Zeeman effect relies on the fact that Zeeman-sensitive transitions split under an external magnetic field. The energies of the split transitions are differed by  $\sim\mu_B B$ , where  $\mu_B$  is the Bohr magneton. The radiation would be both linearly and circularly polarized. By measuring the elliptical polarization, observers can retrieve information on both the magnetic field strength and direction. However, in most astrophysical environments, the line widths are usually much larger than the splitting, causing the information on the linear polarization inaccessible. Nonetheless, the remaining information on the circular polarization would still allow us to measure the line-of-sight component of the magnetic field.

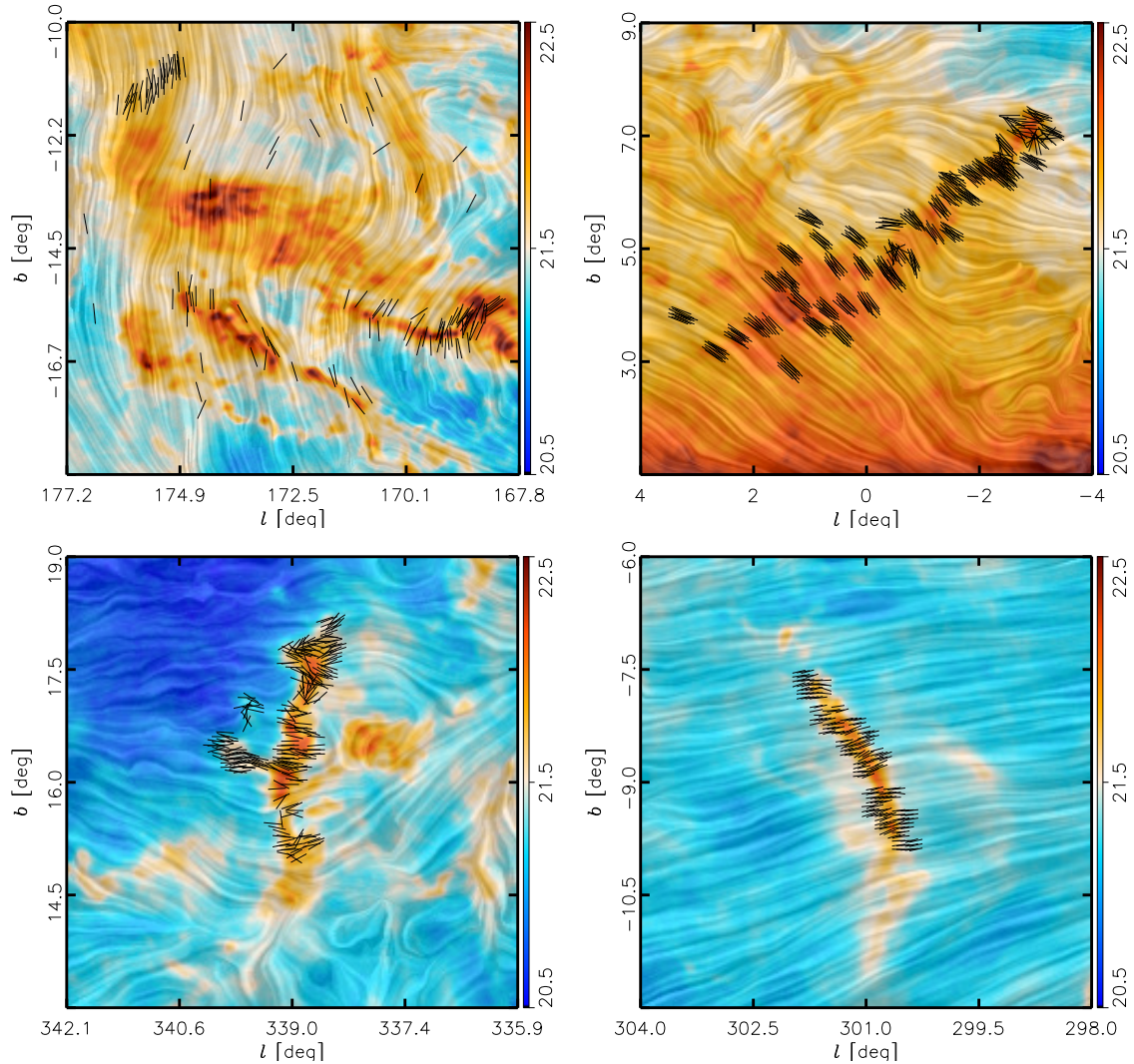


Figure 4.2: Magnetic field orientation inferred from the polarization of dust thermal emission and background starlight toward Taurus (top left), Pipe (top right), Lupus I (bottom left), and Musca (bottom right) molecular clouds. The pattern shown in grayscale is the line integral convolution of the magnetic field orientation inferred by rotating the polarization of the dust thermal emission by  $90^\circ$ . The black line segments show the magnetic field orientation inferred from the polarization of starlight. Figure taken from Soler et al. (2016).

## CHAPTER 5

## THESIS OVERVIEW

In this thesis, we first examine the process of circumstellar disk formation and tackle the magnetic braking catastrophe through numerical simulations using *Athena*. We perform the analysis on realistic disk-formation simulations including the most essential physics. With the simulations available, we consider grain alignment and gas thermal motions that reduce the alignment and synthesize the dust thermal emission and its polarization by solving the vector radiative transfer equations. The results are then compared with ALMA Band 7 observations of 10 protostars in the Perseus molecular cloud. After that, we revisit simulating disk formation and discussed the tools necessary for running a realistic high-resolution disk formation simulation. The implementations of each of them are described along with their applications to other problems.

We begin by analyzing disk formation simulation and synthetic observation in Part II. In Chapter 6, we follow the process of disk formation from prestellar cores to tens of thousands of years after the birth of the protostars using *Athena*. Through comparing designed sets of simulations including different sets of physical processes, we isolate and analyze the features induced by turbulence and AD, and discuss how

they promote disk formation, respectively. We conclude the chapter by discussing the efficacy of both resolutions to the magnetic braking catastrophe and the disk properties of the disks obtained in our simulations.

In Chapter 7, we re-examine observations of protostars in the Perseus molecular cloud and confirm the phenomenon of depolarization in the disk scale. Before attempting to reproduce the trend using synthetic observations of the simulations in the last chapter, we discuss the condition required for grains to align, and thus, lead to polarization. We are able to reproduce most parts of the observed trends using the model derived from this condition. Lastly, we discuss the cause of the depolarization with the help of an analysis of the simulation data.

Part III begins with a brief review of the challenges in simulating star and disk formation. We list the tools needed to be implemented in `Athena++`. The implementations and applications of self-gravity solver, general barotropic EOS, and sink particle treatment are described in Chapters 8, 9, and 10, respectively. The self-gravity solver enabled the 2D (axisymmetric) radiation hydrodynamic simulations of disk formation, which facilitate the computation of temperature that is needed for the astrochemical calculations carried out by Prof. Garrod’s group and for grain growth calculations. The general EOS enabled an exploration of the classic notion of “centrifugal barrier” in disk formation that was recently claimed to be observed with ALMA. The sink particle treatment is needed for both current and future disk formation 3-D simulations in Cartesian coordinates.

Finally, Part IV concludes this thesis. We present a summary of the thesis in Chapter 11. The current status of this field, the progress in resolving the magnetic braking catastrophe, and the outlook of this line of research are discussed in Chapter 12.

## Part II

# Numerical Simulations of Disk Formation

## CHAPTER 6

# DISK FORMATION IN MAGNETIZED DENSE CORES WITH TURBULENCE AND AMBIPOLAR DIFFUSION

*This chapter is adapted from Lam et al. 2019, Monthly Notices of the RAS, 489, 5326, with minimal modifications.*

## ABSTRACT

Disks are essential to the formation of both stars and planets, but how they form in magnetized molecular cloud cores remains debated. This work focuses on how the disk formation is affected by turbulence and AD, both separately and in combination, with an emphasis on the protostellar mass accretion phase of star formation. We find that a relatively strong, sonic turbulence on the core scale strongly warps but does not completely disrupt the well-known magnetically induced flattened pseudo-disk that dominates the inner protostellar accretion flow in the laminar case, in agreement with previous work. The turbulence enables the formation of a relatively large disk

at early times with or without AD, but such a disk remains strongly magnetized and does not persist to the end of our simulation unless a relatively strong AD is also present. The AD-enabled disks in laminar simulations tend to fragment gravitationally. The disk fragmentation is suppressed by initial turbulence. The AD facilitates the disk formation and survival by reducing the field strength in the circumstellar region through magnetic flux redistribution and by making the field lines there less pinched azimuthally, especially at late times. We conclude that turbulence and AD complement each other in promoting disk formation. The disks formed in our simulations inherit a rather strong magnetic field from its parental core, with a typical plasma- $\beta$  of order a few tens or smaller, which is 2–3 orders of magnitude lower than the values commonly adopted in MHD simulations of protoplanetary disks. To resolve this potential tension, longer term simulations of disk formation and evolution with increasingly more realistic physics are needed.

## 6.1 INTRODUCTION

Circumstellar disks play a central role in the formation of both Sun-like stars and planets. It is through such disks that the stars assemble most of their masses. The disk is also the birthplace for planets. Understanding the formation and evolution of disks has always been an integral part of the astronomical quest for our origins.

Despite significant progress, our knowledge of the origins of disks remains far from complete. A major impediment to a full understanding of how disks form and evolve is the magnetic field, which has been observed to thread molecular clouds in general (e.g. Planck Collaboration et al. 2015) and star-forming cloud cores in particular (for recent reviews, see Pattle & Fissel 2019 and Hull & Zhang 2019, and references therein). Since the magnetic field interacts closely with the movement of (partially) ionized gas, particularly the collapse and rotation of the magnetized

star-forming core, it is expected to strongly affect the process of disk formation out of the dense core, although fully quantifying this effect remains a work in progress.

The potential for the magnetic field to strongly affect disk formation was demonstrated by early 2D (axisymmetric) numerical simulations of the collapse of magnetized rotating cores in the ideal MHD limit (e.g. Tomisaka 2000; Allen et al. 2003), where the field removes essentially all of the angular momentum from the collapsing material through magnetic braking. Galli et al. (2006) pointed out that the efficient removal of angular momentum is directly tied to the well-known “magnetic flux problem” in star formation, namely, the stellar magnetic field would be many orders of magnitude stronger than the typically observed values if the magnetic flux threading the core was to be completely frozen into the matter and dragged all the way into the forming star, as would be the case in the strict ideal MHD limit. The concentration of magnetic flux at the center would formally lead to the formation of a split magnetic monopole in this limit, where both the rapid increase of the field strength towards the center and the long lever arm associated with the nearly radial field lines make the magnetic braking efficient and disk formation difficult. This difficulty was sometimes referred to as the “magnetic braking catastrophe” in the theoretical literature of disk formation. How the catastrophe is averted for disk formation is ultimately tied to how the magnetic flux problem is resolved in star formation.

The magnetic flux must be redistributed relative to the accreted matter in order to resolve the magnetic flux problem. The most studied means of flux redistribution is through non-ideal MHD effects, including Ohmic dissipation, AD and the Hall effect. Shu et al. (2006) was the first to suggest that Ohmic dissipation may decouple the magnetic field from the circumstellar material enough to allow for disk formation. This suggestion was confirmed and extended numerically by Krasnopolsky et al. 2010 and Machida et al. 2011, among others (see e.g. Li et al. 2014a and Tsukamoto 2016

for reviews of early work and references therein).

Non-ideal MHD effects are particularly well studied in recent years during the core collapse phase, up to (and slightly beyond) the formation of the second Larson's (stellar) core. In this early phase, there is now broad agreement that a relatively small disk (typically of several AU or smaller in size) can form in the presence of Ohmic dissipation and AD (e.g. Dapp et al. 2012; Tomida et al. 2015; Tsukamoto et al. 2015a; Vaytet et al. 2018) and disk size can be increased or decreased by the Hall effect depending on whether the magnetic field is anti-aligned or aligned with the rotation axis (e.g. Tsukamoto et al. 2015b; Wurster et al. 2018). The agreement is all the more remarkable in view of (1) the numerical challenges in covering the large range in spatial scale (from  $>10\,000$  to  $\ll 1$  AU) and in treating non-ideal MHD effects and (2) the diverse techniques used in tackling the problem: semi-analytic (e.g. Dapp et al. 2012), grid-based codes (e.g. Tomida et al. 2015; Vaytet et al. 2018), and smoothed particle hydrodynamics (SPH) codes (e.g. Tsukamoto et al. 2015a,b; Wurster et al. 2018).

How large ( $\sim 100$  AU scale), persistent disks form and evolve during the later, main protostellar mass accretion phase of star formation is far less certain, as stressed by Tsukamoto (2016) and, more recently, Gray et al. (2018). One potential difficulty in this phase is that, as more and more magnetized core material collapses on to the central protostellar system, more and more magnetic flux should be dragged by the collapsing material to the circumstellar region, making the magnetic field there increasingly stronger and magnetic braking increasingly more efficient, unless the magnetic flux can be effectively redistributed outwards relative to the infalling matter. This redistribution of flux relative to matter lies at the heart of resolving the magnetic flux problem, which is much more severe at the end of the protostellar accretion phase than at the beginning, when the stellar mass is much larger and

much more magnetic flux associated with the stellar mass needs to be redistributed outwards. How it happens exactly is unclear, and is made more difficult by a technical challenge: simulations of the main protostellar accretion phase of star formation require a sink particle treatment (or something equivalent) to avoid the problem of prohibitively small time-step shortly after the formation of the stellar seed.

Sink (or equivalent) treatment has been employed in magnetized protostellar disk formation simulations using both SPH (e.g. Wurster et al. 2016; Lewis & Bate 2018) and grid-based MHD codes. The latter include both ideal MHD simulations with turbulence (e.g. Seifried et al. 2013; González-Casanova et al. 2016; Kuffmeier et al. 2017; Gray et al. 2018; Kuruwita & Federrath 2019), and non-ideal MHD simulations with Ohmic dissipation (e.g. Machida et al. 2011, 2014; Tomida et al. 2017; Kölligan & Kuiper 2018), Ohmic dissipation and turbulence (e.g. Matsumoto et al. 2017), AD (e.g. Masson et al. 2016; Hennebelle et al. 2016; Zhao et al. 2016, 2018), and all three non-ideal MHD effects but no turbulence (e.g. Li et al. 2011). Ideally, one would want to include both turbulence and all three non-ideal MHD effects and follow the disk formation and evolution to the end of the protostellar mass accretion phase.

To achieve this goal, we have started a long-term program using the *Athena* MHD code (Stone et al. 2008). As a first step, we will focus on only one of the three non-ideal MHD effects, AD, which has yet to be studied together with turbulence during the protostellar mass accretion phase using a sink treatment. We find both turbulence and AD facilitate disk formation, but in a complementary way. The turbulence enables the formation of disks at early times and the AD allows the turbulence-enabled early disks to persist to later times. In addition, the turbulence tends to make the AD-enabled disks less prone to gravitational fragmentation.

The rest of the paper is organized as follows. In Section 6.2, we describe the set-up of the numerical simulations. This is followed by a discussion of the results of

the simulations that include only turbulence (Section 6.3) and only AD (Section 6.4), respectively. We then discuss those disk formation simulations that include both turbulence and AD in Section 6.5. Section 6.6 focuses on the gross properties of the formed disks, especially their degree of magnetization. The main results of the paper are summarized in Section 6.7.

## 6.2 PROBLEM SETUP

### 6.2.1 Governing equations

The non-ideal MHD equations including self-gravity that we solve numerically are

$$\frac{\partial \rho}{\partial t} + \nabla \cdot (\rho \mathbf{v}) = 0, \quad (6.1)$$

$$\rho \frac{\partial \mathbf{v}}{\partial t} + \rho (\mathbf{v} \cdot \nabla) \mathbf{v} = -\nabla P + \frac{1}{c} \mathbf{J} \times \mathbf{B} - \rho \nabla \Phi_g, \quad (6.2)$$

$$\frac{\partial \mathbf{B}}{\partial t} = \nabla \times (\mathbf{v} \times \mathbf{B}) - \frac{4\pi}{c} \nabla \times (\eta_A \mathbf{J}_\perp), \quad (6.3)$$

$$\nabla^2 \Phi_g = 4\pi G \rho, \quad (6.4)$$

where  $\mathbf{J} = (c/4\pi)\nabla \times \mathbf{B}$  is the current density, and  $\mathbf{J}_\perp = [(\mathbf{J} \times \mathbf{B}) \times \mathbf{B}]/B^2$  is the current density perpendicular to the magnetic field. As a first step towards a comprehensive model, we make the simplifying assumptions that the gas is isothermal (with  $P = \rho c_s^2$ ), that the ambipolar diffusivity  $\eta_A$  is given by

$$\eta_A = \frac{B^2}{4\pi\gamma\rho\rho_i}, \quad (6.5)$$

where  $\gamma = \langle \sigma v \rangle / (m + m_i)$  is the ion-neutral drag coefficient (charged grains are not accounted for explicitly), and that the ion density  $\rho_i$  is approximated using  $\rho_i = C\rho^{1/2}$ , where  $C$  is a constant (assume equilibrium between cosmic-ray ionization and recombination, e.g. Shu 1992); these approximations will be relaxed in future investigations. Therefore, the ambipolar diffusivity can be rewritten into

$$\eta_A = Q_A \frac{B^2}{4\pi\rho^{3/2}}, \quad Q_A = \frac{1}{\gamma C}. \quad (6.6)$$

The rest of the symbols have their usual meaning.

## 6.2.2 Numerical method

We carry out a set of simulations in Cartesian coordinates using **Athena**, a grid-base code that solves 3D time-dependent non-ideal MHD equations including self-gravity (Stone et al. 2008; Bai & Stone 2011). Roe solver is used for solving the MHD equations and self-gravity is solved using FFT with zero-padded boundary, which better isolates the core from its images, as if the computational domain is twice as big. Standard outflow boundary conditions are imposed in all three directions except for the velocity in the ghost zone, which is set to zero if it is pointing into the computational domain, to prevent material from entering the simulation box. In order to speed up the simulations and follow the formation and evolution of disks for as long as possible, two treatments are employed.

- (i) *Sink particle* — As mentioned in the introduction (Section 6.1), we are interested in studying disk formation and evolution during the main protostellar accretion phase, where a sink particle treatment is necessary to avoid prohibitively small time-steps. Our implementation of sink particles is based on that by Gong & Ostriker (2013). We modified the original treatment slightly to better conserve

mass and momentum. Specifically, the sink particle always lives in the center cell of a sink region of  $3 \times 3 \times 3$  cells. Density and momentum thresholds are calculated for each cell in the sink region by averaging the closest neighboring cells in the active zone. Any excess mass and momentum over the thresholds in the sink region are removed from the grid and put into the sink particle; the magnetic field in the sink region is left untouched. This implementation is intended to mimic the eventual decoupling of the material that is accreted on to the central protostar and the magnetic flux associated with it that must occur in order to resolve the well-known magnetic flux problem for the central star. While the treatment is a very rough approximation of the physics involved in the actual decoupling process, it does capture an essential aspect of the process, namely, the magnetic flux associated with the stellar material is not destroyed artificially;<sup>1</sup> rather, it is preserved to machine accuracy since the magnetic field in the sink region is evolved in exactly the same manner as that in the active region using CT in the `Athena` code.

- (ii) *AD time-step floor* — While running the non-ideal MHD simulations, we find the AD time-step often drops to very small values, causing the simulations to stall. From the definition

$$\Delta t_{\text{AD}} = \frac{\Delta x^2}{6\eta_{\text{A}}} = \frac{4\pi\rho^{3/2}\Delta x^2}{6Q_{\text{A}}B^2}, \quad (6.7)$$

it is immediately clear that the AD time-step problem is most severe in cells with very low densities and moderately strong magnetic fields (Mac Low et al. 1995). We found that this is indeed the case. To speed up the simulations, we

---

<sup>1</sup>The magnetic flux in the densest disk-forming region is not destroyed by Ohmic dissipation or other non-ideal MHD effects (as discussed in, e.g. the notes-added-in-proof of Shu et al. 2006). It is redistributed to lower density regions where the non-ideal MHD effects tend to be weaker.

reduce the diffusivity in such cells locally by enforcing a lower limit (or floor) on the AD time-step. We monitor the affected cells to make sure that only a tiny amount of mass is affected by the treatment.

### 6.2.3 Model set-up and parameters

We start our simulations with a  $0.5 M_{\odot}$  centrally condensed spherical core with a radius of 2000 AU placed in a simulation box of 5000 AU on each side. The density follows the pseudo-Bonner–Ebert sphere profile, which is described by

$$\rho(r) = \frac{\rho_0}{1 + (r/r_c)^2}, \quad (6.8)$$

where  $\rho_0$  is the central density and  $r_c$  is the characteristic radius, which is chosen to be 1/3 of the radius of the core so that the central density is  $10\times$  higher than the edge density. The background density is set to 1 percent of the edge density. The isothermal sound speed  $c_s$  is set to  $0.2 \text{ km s}^{-1}$ . The core is assumed to have a solid-body rotation with an angular speed  $\omega \approx 6 \times 10^{-13} \text{ s}^{-1}$  (corresponds to a rotational to gravitational energy ratio  $\beta_{\text{rot}} \approx 0.03$ ) with the rotational axis aligned with the z-axis. This combination of parameters yields a large disk of  $\sim 400$  AU in the absence of a magnetic field that is easily resolvable in our simulations. The magnetic field strength is characterized by the dimensionless mass-to-flux ratio  $\lambda = 2\pi\sqrt{G}(M_{\text{core}}/\Phi)$ , where  $M_{\text{core}}$  is the total mass of the core,  $\Phi$  is the magnetic flux threading through the whole core, and  $(2\pi\sqrt{G})^{-1}$  is the critical value for the mass-to-flux ratio. A uniform magnetic field along the rotation axis with strength corresponding to  $\lambda \approx 2.6$  for the dense core as a whole is adopted in all of our simulations. We note that in our setup the mass-to-flux ratios along different (initially vertical) flux tubes are different, decreasing radially outwards from a maximum value of  $\sim 8.4$  on the axis. We also note

that the above choice of dimensional numbers is not unique, since isothermal MHD simulations with self-gravity are scale-free. For example, one can choose a different length scale ( $L$ ), which would lead to a corresponding change in the mass, density and magnetic field strength (in proportional to  $L$ ,  $L^{-2}$ , and  $L^{-1}$ , respectively). The scale-free nature of the simulations is preserved in the presence of AD with the adopted power-law dependence of the ion density on the neutral density ( $\rho_i = C\rho^{1/2}$ ).

In the models with turbulence, an initial turbulent velocity field is generated with an  $k^{-2}$  power spectrum (Gong & Ostriker 2011). In order to ensure fair comparison between different models, any additional total angular momentum is removed from the turbulent velocity field before it is added on top of the solid-body rotation. The turbulence is allowed to decay freely after the initial injection. Since the dense core in our simulation collapses rather quickly, the majority of the turbulent motion is retained during the core collapse and disk formation. The level of initial turbulence is characterized by the rms Mach number  $\mathcal{M}$  such that an additional turbulent kinetic energy  $E_{\text{turb}} = M_{\text{core}}\mathcal{M}^2c_s^2/2$  is added. Three levels of turbulence are considered in this work, corresponding to  $\mathcal{M} = 0.0, 0.5, \text{ and } 1.0$ , respectively. We do not consider supersonic turbulence because they are uncommon in low-mass star-forming cores (e.g. Bergin & Tafalla 2007).

For AD, we follow Shu (1992) and adopt  $\gamma = 3.5 \times 10^{13} \text{ cm}^3 \text{ g}^{-1} \text{ s}^{-1}$  and  $C = 3 \times 10^{-16} \text{ cm}^{-3/2} \text{ g}^{1/2}$  (corresponding to the standard cosmic ray ionization rate of  $10^{-17} \text{ s}^{-1}$ ), which are taken from Draine et al. (1983). This combination yields a value of the coefficient for the ambipolar diffusivity  $Q_A$  defined in equation (6.6) of  $95.2 \text{ g}^{1/2} \text{ cm}^{-3/2} \text{ s}$ , which will be termed “the standard value” of the AD coefficient and denoted by  $Q_{A,0}$  hereafter. We will consider a range of  $Q_A$ , including  $0\times, 0.1\times, 0.3\times, 1\times, 3\times, \text{ and } 10\times$  the standard value. The model parameters are summarized in Table 1.

Table 6.1: Model parameters and outcome.

Model Name	$\mathcal{M}$	$Q_A/Q_{A,0}$	Comments
M0.0AD0.0	0.0	0.0	DEMS <sup>a</sup>
M0.5AD0.0	0.5	0.0	Transient Disk & DEMS
M1.0AD0.0	1.0	0.0	Transient Disk & DEMS
M0.0AD0.1	0.0	0.1	DEMS
M0.0AD0.3	0.0	0.3	DEMS
M0.0AD1.0	0.0	1.0	DEMS & Persistent Disk
M0.0AD3.0	0.0	3.0	Persistent Disk
M0.0AD10.0	0.0	10.0	Persistent Disk
M0.1AD0.1	0.1	0.1	DEMS
M0.1AD0.3	0.1	0.3	DEMS
M1.0AD0.1	1.0	0.1	Transient Disk & DEMS
M1.0AD0.3	1.0	0.3	Transient Disk & DEMS
M1.0AD1.0	1.0	1.0	Transient Disk & DEMS
M1.0AD3.0	1.0	3.0	Persistent Disk
M1.0AD10.0	1.0	10.0	Persistent Disk
M0.0AD1.0US <sup>b</sup>	0.0	1.0	DEMS
M1.0AD1.0US <sup>b</sup>	1.0	1.0	DEMS

<sup>a</sup> DEMS refers to the so-called “decoupling-enabled magnetic structure”, a magnetically-dominated, low-density structure that is completely different from the dense rotationally supported disk (see Zhao et al. 2011, and Fig. 6.1 below)

<sup>b</sup> Simulation is initialized as a uniform sphere.

### 6.2.4 Numerical code and zoom-in simulations

The *Athena* family of codes has been used for MHD simulations in a wide range of astrophysical systems, from clusters of galaxies (e.g. Martizzi et al. 2019) to the atmospheres of planets (e.g. Li & Chen 2019). In star formation, it has been used to study the dynamics of magnetized molecular clouds and formation of dense cores and filaments (e.g. Chen & Ostriker 2014, 2018). In this paper, we start a long-term program to extend such studies to core collapse and disk formation. This code choice is motivated by several factors. First, the code uses CT to treat the magnetic field evolution, which ensures that the divergence-free condition  $\nabla \cdot \mathbf{B} = 0$  is satisfied to the machine accuracy. This is of paramount importance for the magnetized disk formation problem because it prevents the generation of magnetic monopoles (and their associated change of magnetic field topology) even close to the forming protostar where a strong variation of the magnetic field is expected. Secondly, a well-tested sink particle treatment including magnetic fields is already in place. Thirdly, a treatment of AD has already been implemented and has been applied successfully to the related problem of dense core formation (Chen & Ostriker 2014).

A well-known difficulty with the treatment of AD is that the time-step required for numerical stability is proportional to the grid size ( $\Delta x$ ) squared (see equation 6.7). To alleviate this difficulty, we have decided to adopt a strategy of zoom-in simulations with uniform grids. Specifically, we adopt a base grid of  $256^3$  for the prestellar phase of core evolution and restart each simulation right after the sink particle formation, keeping only the central  $128^3$  cells in the original grid, and recasting them into  $256^3$  cells as follows. Each of the kept original cells is split into eight octants of equal size. We keep the cell-centered hydrodynamics quantities untouched, which are later smoothed out as they evolve. Each of the three face-centered magnetic

field components is linearly interpolated along its direction to each of the new faces, which ensures that the magnetic field on the new (finer) grid remains divergence-free. For our canonical choice of length scale, the resolution of the zoom-in simulation is  $\sim 10$  AU. This relatively large cell size enables us to explore efficiently a wide range of simulation parameters, which is important for uncovering general trends, especially with respect to the strength of AD. However, as discussed in Section 6.2.3, the physical scale of these simulations can in principle be reduced by choosing a smaller length scale.

We will first examine the trends in simulations where only turbulence or only AD is included (Sections 6.4 and 6.3, respectively). This is followed by a discussion of those simulations where both effects are included (Section 6.5).

### 6.3 DISK FORMATION IN IDEAL MHD: TURBULENCE

To isolate the effects of turbulence from those of AD, we will first concentrate on ideal MHD simulations with three different levels of turbulence characterized by  $\mathcal{M} = 0.0$  (Model M0.0AD0.0; laminar), 0.5 (M0.5AD0.0; subsonic), and 1.0 (M1.0AD0.0; transonic).

Figure 6.1 shows the column density along the  $z$ -axis (the rotation axis and the direction of the initial magnetic field) of the three models at two representative epochs when the sink particle has accreted  $0.1 M_{\odot}$  (upper row) and  $0.2 M_{\odot}$  (lower) of material, respectively. We choose to compare the models at the same sink (stellar) mass rather than the same absolute time (the time elapsed since the beginning of the simulation) or the relative time (the time elapsed since the formation of the sink particle) because, as mentioned earlier, the magnetic flux released from the stellar material plays a central role in the disk formation problem, and this flux is expected to be similar for the same stellar mass.

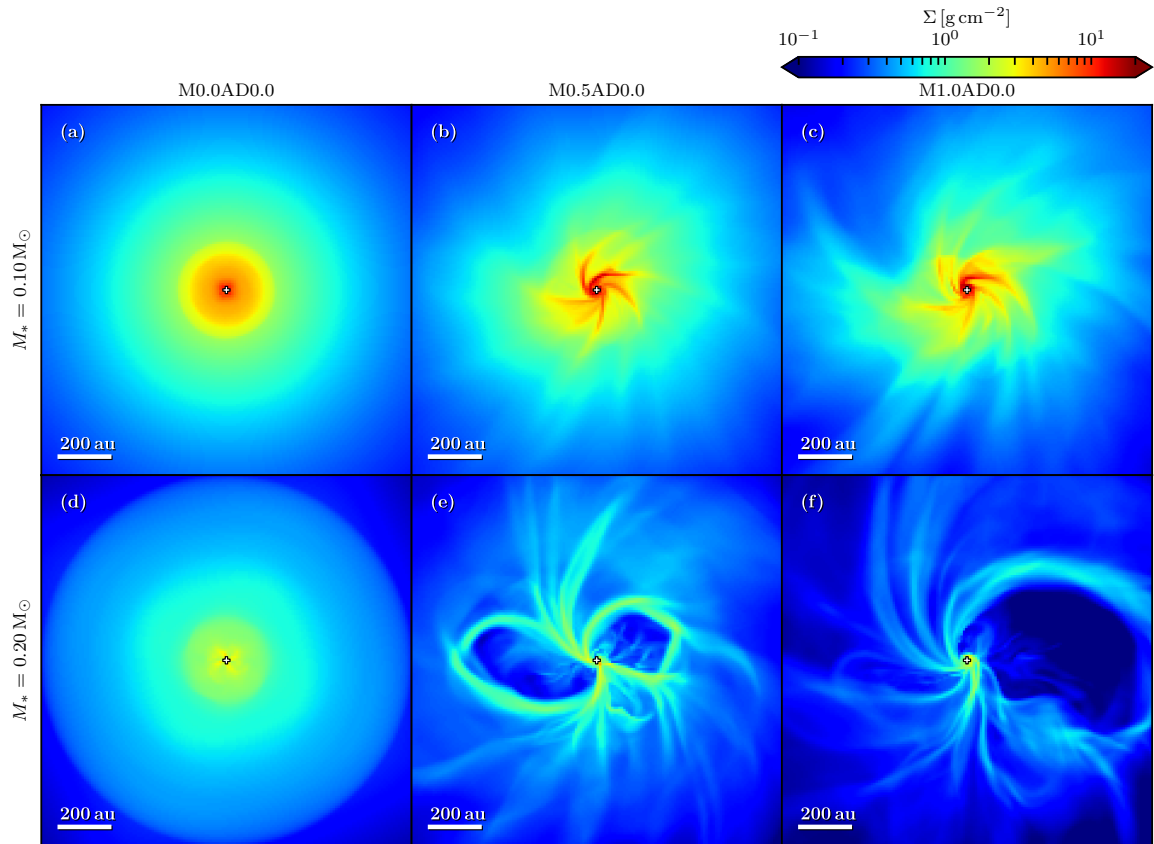


Figure 6.1: Column density along  $z$ -axis of the zoom-in simulations of the three ideal MHD models with different levels of turbulence (left to right,  $\mathcal{M} = 0.0, 0.5$  and  $1.0$ ) when the sink particle has accreted  $0.1 M_{\odot}$  (upper row) and  $0.2 M_{\odot}$  (lower). The sink particle is marked by a cross. (See the supplementary material in the online journal for an animated version of the column density distribution for each model. Models M0.0AD0.0 and M1.0AD0.0 are also included in the animated version of Figs 6.6 and 6.11, respectively.)

The simplest case of no turbulence (Model M0.0AD0.0) follows the well-known pattern that the gravitational collapse proceeds preferentially along the field lines, forming a thin, equatorial pseudo-disk through which most of the material is accreted. Rotation of the infalling pseudo-disk material winds up magnetic field lines, driving a bipolar outflow that removes angular momentum from the pseudo-disk. The magnetic flux brought in by accretion accumulates in the sink region and causes the formation of the so-called DEMS (decoupling-enabled magnetic structure; Zhao et al. 2011), which persists until the end of the simulation. The combination of efficient angular momentum removal by outflow and the obstacle presented by the magnetically dominated DEMS makes it difficult to form a rotationally supported disk, which is absent from the laminar model.

In the presence of a subsonic (Model M0.5AD0.0) or transonic (M1.0AD0.0) turbulence, the basic picture remains broadly similar. In particular, both pseudo-disk and DEMS still exist in the turbulent simulations. One difference is that the core collapse is slowed down somewhat by the additional kinetic energy associated with the turbulence. Another difference is that the pseudo-disk is significantly warped, as discussed in more detail in Section 6.3.1 below. Perhaps more importantly, the turbulence has induced the formation of prominent spiral structures close to the central protostar that are disk-like, at least at relatively early times (see panels b and c of Fig. 6.1). These disk-like structures are indicative of the beneficial effects of turbulence on disk formation. However, they largely disappear at later times as the circumstellar region becomes more dominated by DEMS (see panels e and f of Fig. 6.1). The effects of turbulence on disk formation will be discussed in more detail in Section 6.3.2 below.

We note that a large fraction, if not most, of the magnetic flux liberated from the central star is contained in the DEMS in these ideal MHD simulations, which is approximately the region where the plasma- $\beta$  is less than unity and the radial

velocity is positive (i.e. expanding). For example, we have computed the magnetic flux threading such a region on the equatorial plane for the laminar ( $\mathcal{M} = 0$ ) model when the stellar mass reaches  $M_* = 0.25 M_\odot$ , and found a dimensionless ratio of the stellar mass to the DEMS magnetic flux of  $\sim 4.8$ . It is bracketed by the expected minimum value of  $\sim 3.0$  (if the collapse is isotropic) and maximum of  $\sim 5.4$  (if the stellar mass is accumulated along the field lines). Similarly, the ratio of the stellar mass to the DEMS magnetic flux is  $\sim 4.9$  for the most turbulent model of  $\mathcal{M} = 1$  when  $M_* = 0.2 M_\odot$  (see Fig. 6.1f), again consistent with the range between  $\sim 3.1$  to  $\sim 5.9$  expected for the stellar mass of  $0.2 M_\odot$ .

### 6.3.1 Warped pseudo-disk

In this subsection, we focus on the structure of the protostellar accretion flow on the several hundred to a few thousand AU scale that is well resolved by our simulations. This region is important to study both theoretically and observationally. Theoretically, it is the bridge between the larger scale dense core and the smaller scale disk (if present). Observationally, it is starting to be probed by (sub)millimeter interferometers, especially ALMA. One may naively expect this region to be driven completely chaotic by turbulence. However, in the presence of a dynamically significant, large-scale magnetic field, the protostellar accretion flow remains spatially coherent to a large extent, as first demonstrated by Li et al. (2014b) for a non-self-gravitating accretion flow on to a star of fixed mass. Here we show that this basic result still holds when the self-gravity and a varying stellar mass are treated self-consistently.

We demonstrate the coherence of the density structure in two ways, through density distributions on cylindrical surfaces around the z-axis passing through the sink particle (Fig. 6.2) and three-dimensional visualization (Fig. 6.3). Panel (a) of

Fig. 6.2 shows that, at a representative epoch when  $M_* = 0.1 M_\odot$ , the density distribution of the non-turbulent model (M0.0AD0.0) on a representative cylinder of radius  $r_{\text{cyl}} = 250 \text{ AU}$  is concentrated near the equator. This is of course the well-known pseudo-disk. As the level of turbulence increases, the pseudo-disk becomes increasingly more warped (compare panels a–c) but remains spatially connected. This coherence persists to later times, even in the case of strongest turbulence (M1.0AD0.0; see panels d–f, where the density distributions are plotted for the epochs when  $M_* = 0.05$ ,  $0.15$  and  $0.2 M_\odot$ , respectively). The pseudo-disk warping is not limited to the particular radius of  $r_{\text{cyl}} = 250 \text{ AU}$ , as illustrated in panels (g)–(i), where we plot the density distributions for Model M1.0AD0.0 at the same time as shown in panel (c) but on cylinders of three other radii ( $r_{\text{cyl}} = 125$ ,  $500$  and  $1000 \text{ AU}$ ).

The spatial coherence of the turbulence-warped pseudo-disk can be visualized more clearly in Fig. 6.3, which shows the isosurface of the normalized density

$$\tilde{\rho} = \frac{\rho r_{\text{cyl}}}{\Sigma} = 1, \quad (6.9)$$

where  $r_{\text{cyl}}$  is the cylindrical radius and  $\Sigma$  is the column density along the direction of the initial magnetic field ( $z$ -axis). Physically,  $\tilde{\rho}$  is a dimensionless quantity that is the inverse of the characteristic thickness of the local density structure ( $\Sigma/\rho$ ) relative to the local cylindrical radius. It is a measure of the (angular) “thinness” of the density structure. We find it easier to highlight regions with high-mass concentration at different radii simultaneously (i.e. the pseudo-disk) using this dimensionless quantity than the density itself, because the latter varies much more strongly with radius.

The 3D view of the pseudo-disk drives home the important conceptual point that, in the presence of a dynamically significant large-scale magnetic field and a subsonic or transonic turbulence, the inner protostellar accretion flow has a unique texture that is

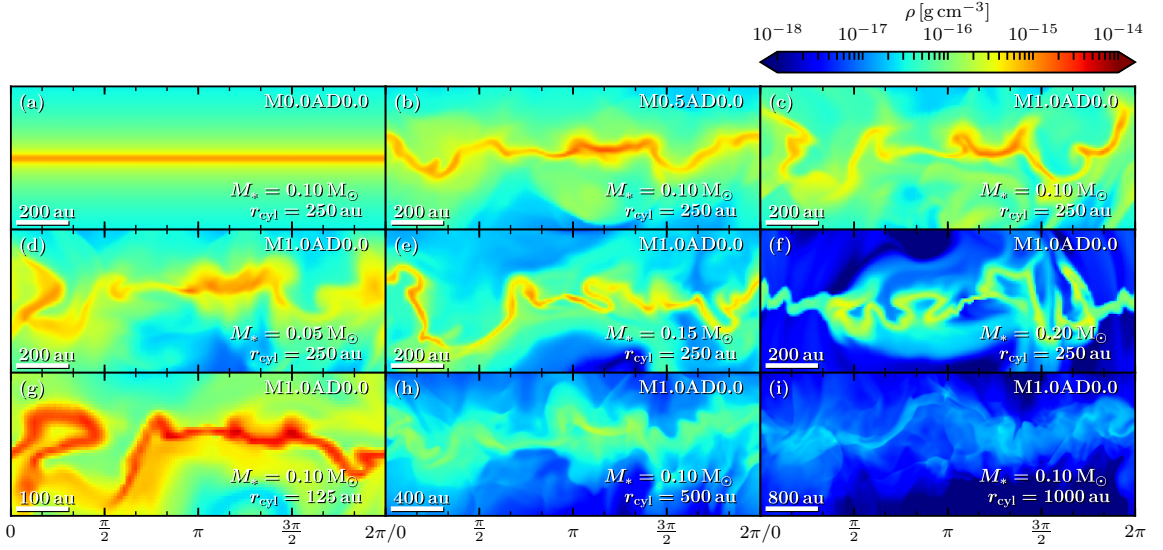


Figure 6.2: Turbulence-induced pseudo-disk warping. Plotted in the top row are the density distributions on a cylinder of radius  $r_{\text{cyl}} = 250 \text{ AU}$  at the epoch when  $M_* = 0.1 M_\odot$  for Model M0.0AD0.0 (panel a), M0.5AD0.0 (b), and M1.0AD0.0 (c) as a function of azimuthal angle  $\phi$  (from 0 to  $2\pi$ ) and height  $z$ , showing a more severe warping of the (dense) pseudo-disk by a stronger turbulence. The middle row is for Model M1.0AD0.0 at the same radius as in panel (c) but at different epochs [ $M_* = 0.05$  (d),  $0.15$  (e), and  $0.2 M_\odot$  (f)], showing the time evolution of the warped pseudo-disk. The bottom row is also for Model M1.0AD0.0 at the same epoch as in panel (c) but at different cylindrical radii [125 (g), 500 (h), and 1000 au (i)].

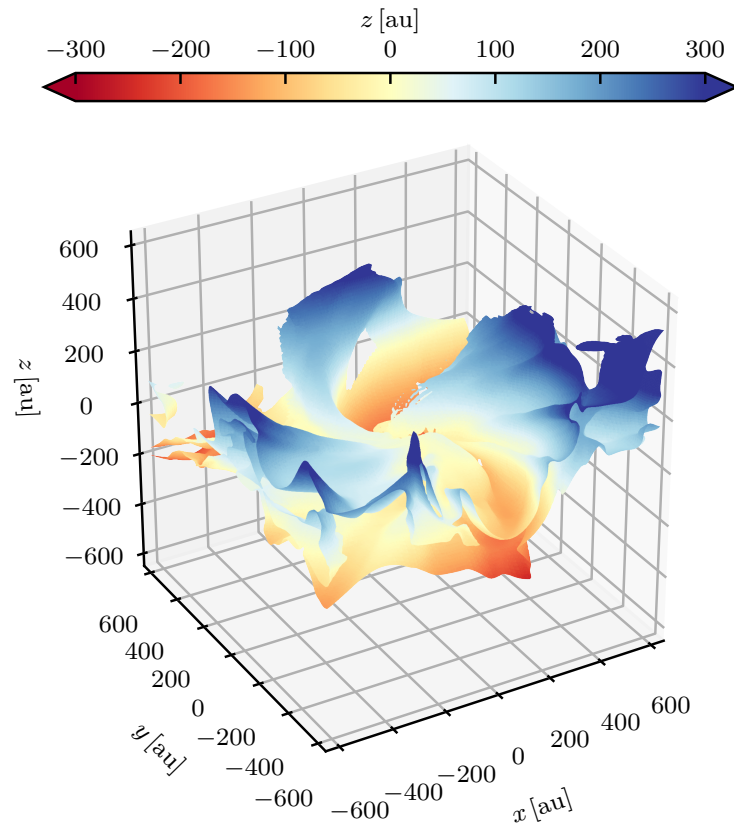


Figure 6.3: 3D view of the turbulence-warped pseudo-disk. Plotted is the isosurface of the normalized density  $\tilde{\rho} = 1$  at an epoch when the stellar mass  $M_* = 0.15 M_\odot$  for the ideal MHD sonic turbulence model M1.0AD0.0. The surface is colored by its height above or below the  $x$ - $y$  plane passing through the sink particle (i.e. its  $z$  value).

neither completely chaotic (as expected, e.g. for a region of isotropic turbulence) nor simply organized (as the equatorial pseudo-disk in the laminar Model M0.0AD0.0). Instead, it has a structure intermediate between these two extremes that is shaped by the interaction between the large-scale magnetic field and gravity, which tends to produce a flattened structure (i.e. a pseudo-disk) because of the anisotropy in the magnetic support against the gravity, on the one hand, and by the turbulent motions initially present inside the core, which tend to perturb the flattened structure by deflecting the gravity-induced collapsing motions towards the pseudo-disk and by distorting the magnetic field lines. The perturbed pseudo-disk is further modified by rotation, especially at small radii where the rotational speed is typically the highest. Indeed, the spiral structures that are prominent in the column density maps of the turbulent models in Fig. 6.1 are those more tilted parts of the warped pseudo-disk that are viewed more edge-on (i.e. with a longer path-length in the pseudo-disk along the line of sight), as already discussed in Li et al. (2014b) in the absence of self-gravity. The inclusion of self-gravity in our simulations strengthens the general picture that the warped pseudo-disk serves as a dense “backbone” for the inner protostellar accretion flow on to low-mass stars formed in turbulent, magnetized dense cores. It would be interesting to test this picture through high-resolution observations, especially using ALMA.

### 6.3.2 Enhanced rotation by turbulence

In Fig. 6.1, we have already seen hints of the beneficial effects of turbulence on disk formation from the morphology of the circumstellar material. These effects are quantified in Fig. 6.4, which plots the mass-weighted distributions of the infall and rotational speeds as a function of radius at the same two representative stellar mass  $M_* = 0.1$  and  $0.2 M_\odot$  as in Fig. 6.1. At the relatively early epoch when  $M_* = 0.1 M_\odot$ ,

the bulk of the circumstellar material on the 100-AU scale rotates well below the Keplerian speed in the laminar case (Model M0.0AD0.0), with a rotational speed significantly below the infall speed, which is indicative of a rapidly collapsing inner protostellar envelope rather than a rotationally supported structure. This is in contrast with the turbulent cases where the rotational speed is significantly closer to the Keplerian value and the infall speed closer to zero. This is especially true for the sonic turbulence model (M1.0AD0.0) where the rotational speed approaches the Keplerian speed outside the sink region ( $r_{\text{cyl}} \gtrsim 15 \text{ AU}$ ), and the infall speed is  $\sim 2\text{--}3$  times lower than that (and well below the free-fall value). Whether this slowly collapsing (compared to free fall), rotationally dominated, flattened circumstellar structure is called a “disk” or not depends on how disks are defined (e.g. Vaytet et al. 2018). A quantitative definition of disks will be described below in Section 6.6.1.

The sonic turbulence model (M1.0AD0.0) is strongly affected by the magnetically dominated, low-density DEMS at later times. For example, a well-developed DEMS is clearly visible in the surface density plot of Fig. 6.1 when  $M_* = 0.2 M_\odot$  (see panel f). Nevertheless, the infall speed remains well below the free-fall value even at this late epoch, and the (mass-weighted) rotational speed still approaches the Keplerian value right outside the sink region, as illustrated by the red curves in panel (b) of Fig. 6.4. At this epoch, the appearance of the circumstellar region of the weaker turbulence case (M0.5AD0.0) is also dominated by DEMS, although its rotational speed is somewhat lower on average and its infall motion somewhat faster compared to Model M1.0AD0.0 (compare green and red curves in panel b). This trend continues to the laminar case (violet curves), especially for the rotational speed, which is close to zero on the 100-AU scale. This comparison re-enforces the notion that turbulence facilitates disk formation, making it possible for the circumstellar material to rotate closer to the Keplerian speed.

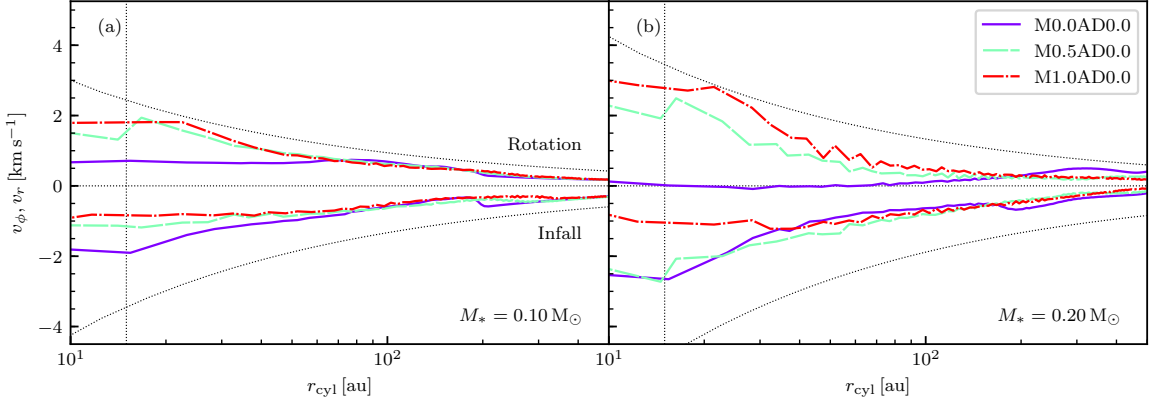


Figure 6.4: Distributions of the mass-weighted rotational (upper curves) and infall speeds (lower) in a wedge within  $45^\circ$  of the equatorial plane compared to the Keplerian (upper black dotted line) and free-fall (lower) profile at two representative epochs with stellar mass of  $M_* = 0.1$  (panel a) and  $0.2 M_\odot$  (b) for three ideal MHD models with turbulent Mach number of  $\mathcal{M} = 0.0$  (violet solid line),  $0.5$  (green dashed), and  $1.0$  (red dash-dotted). The vertical dotted line in each panel denotes roughly the radius of the sink region.

There are several reasons suggested for why turbulence tends to promote disk formation. They include turbulence-induced magnetic diffusion (e.g. Santos-Lima et al. 2012), tangling of magnetic field lines (e.g. Seifried et al. 2013), field-rotation misalignment (e.g. Joos et al. 2013; Gray et al. 2018), and pseudo-disk warping (e.g. Li et al. 2014b). To these we add two more possibilities: earlier formation of DEMS and self-sorting of infalling protostellar envelope materials of different specific angular momenta.

Strongly magnetized, low-density, expanding DEMS are formed in all three ideal MHD cases (see e.g. Fig. 6.1) especially at the later epoch when  $M_* = 0.2 M_\odot$ . It turns out that such DEMS form at a smaller stellar mass for the turbulent case compared to the laminar case, as can be seen most clearly from the animation of the column density map in the supplementary material of the online version of the article. The reason for the earlier (in terms of stellar mass) formation is that DEMS are produced by a competition between the ram pressure of the infalling material

and the magnetic forces exerted by the magnetic flux decoupled from the accreted mass. As the star accretes mass, the magnetic flux associated with the accreted mass is left in its surroundings, causing an accumulation of magnetic flux. Although the ram pressure increases initially due to the increasing central mass and infall speed, it drops with the density at later times. When the ram pressure becomes dominated by the magnetic forces, DEMS form. This process is facilitated by turbulence, which produces inhomogeneity in the density distribution in the circumstellar gas, including low-density channels between dense spirals where the trapped magnetic flux can leak out more easily and, therefore, at an earlier epoch. The flux leakage lowers the magnetic flux near the accreting protostar, as illustrated in the panel (a) of Fig. 6.5, which shows a much lower magnetic flux passing through an equatorial circle of 125 AU in radius centered on the protostar for each of the two turbulence models compared to the laminar model. The lower magnetic flux in turn promotes disk formation.

There is the possibility that the decrease of magnetic flux in the central region with increasing turbulence is due to enhanced magnetic diffusion from turbulence-induced reconnection (as reviewed by Lazarian et al. 2015). Indeed, in their ideal MHD simulations of strongly magnetized, turbulent, cluster-forming clouds, Li et al. (2015) found that the mass-to-flux ratios of the most massive dense clumps are often larger than that of the cloud as a whole, indicating a breakdown of the flux-freezing condition, possibly due to turbulent reconnection. In panel (b) of Fig. 6.5, we plot the dimensionless ratio  $\lambda_{125}$  of the mass  $M_{125}$  enclosed within a sphere of 125 AU in radius (including the stellar mass) to the magnetic flux passing through an equatorial circle of 125 AU (shown in panel a) as a function of the enclosed mass, and compare it to the initial mass-to-flux ratio of the core as a whole ( $\lambda_{\text{core}}$ , the dotted line in the panel), as well as the mass-to-flux ratios expected under flux freezing in two limits: (1) the stellar mass is accumulated along the (initially vertical) magnetic field lines ( $\lambda_{\text{cyl}}$ ,

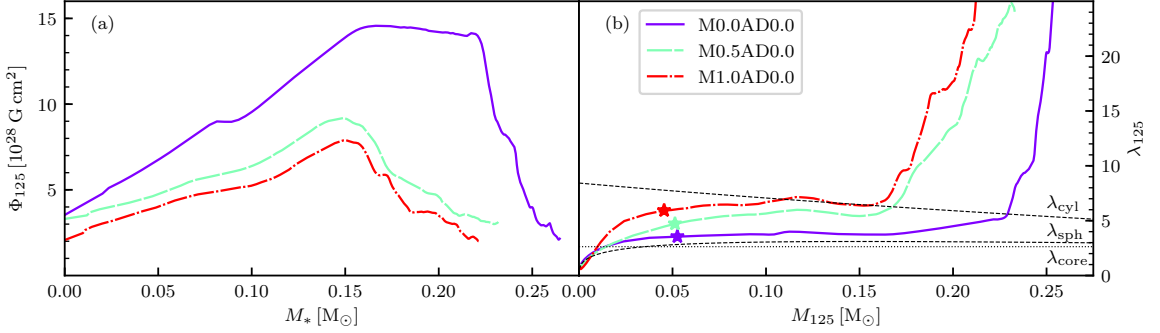


Figure 6.5: Reduction of the magnetic flux close to the accreting protostar by turbulence. Plotted are (a) the magnetic flux passing through a circle of 125 AU in radius on the equatorial plane as a function of stellar mass and (b) the dimensionless ratio of the mass enclosed by a sphere of 125 AU in radius (including the stellar mass) and the magnetic flux as a function of the enclosed mass for ideal MHD models of turbulence Mach number  $\mathcal{M} = 0.0$  (violet solid line), 0.5 (green dashed), and 1.0 (red dash-dotted). The dotted line in panel (b) denotes the initial value for the core as a whole  $\lambda_{\text{core}}$  and the upper and lower dashed lines denote, respectively, the mass-to-flux ratio expected under flux freezing in the limit that the stellar mass is accumulated along the (initially vertical) magnetic field lines ( $\lambda_{\text{cyl}}$ ) and that the core collapse into the star is strictly spherical or isotropic ( $\lambda_{\text{sph}}$ ). The star symbol denotes the time of sink particle formation for each model.

upper dashed line), and (2) the core collapse into the star is strictly spherical or isotropic ( $\lambda_{\text{sph}}$ , lower dashed line). It is clear that although  $\lambda_{125}$  is significantly larger than  $\lambda_{\text{core}}$  and  $\lambda_{\text{sph}}$  over most of the time for the turbulent models, it remains near or below  $\lambda_{\text{cyl}}$ , except towards the end of the simulation, when  $\lambda_{125}$  increases rapidly above  $\lambda_{\text{cyl}}$ . Therefore, the relatively high values of  $\lambda_{125}$  before its rapid rise could in principle come from mass accumulation along field lines rather than turbulent reconnection, although some contribution from the latter cannot be excluded. The rapid increase in  $\lambda_{125}$  towards the end is due to rapid expansion of DEMS, which happens even for the laminar case without any turbulence.

Another way that turbulence can help with disk formation is that, unlike the laminar case with a flat equatorial pseudo-disk, the bulk of rotating, protostellar material can fall close to the central protostar on different planes (see Fig. 6.3). In

the presence of a strong magnetic field, material on the same magnetic field line would tend to flow along the field line and form the dense (warped) pseudo-disk, as illustrated in Fig. 6.2 and discussed in Section 6.3.1. The turbulence-induced variation of angular momentum of the material initially located on the same field line would be largely erased once the bulk of this material has collapsed along the field line on to the pseudo-disk. Nevertheless, there can still be variation of angular momentum between the materials collected on to the pseudo-disk along different field lines. Because of strong warping, different parts of the pseudo-disk with different specific angular momenta can fall towards the central protostar on different planes, which reduces their chance of collision. This makes it easier for the high specific angular momentum material to retain its angular momentum and form a disk, without being impeded by the low specific angular momentum material, which can fall into the sink region without colliding with the high specific angular material.

## 6.4 DISK FORMATION IN NON-IDEAL MHD: AMBIPOLAR DIFFUSION

In this section, we seek to isolate the effects of AD by setting the turbulence to zero and considering a wide range of ambipolar diffusivity, with the coefficient  $Q_A = 0 \times$  (Model M0.0AD0.0),  $0.1 \times$  (M0.0AD0.1),  $0.3 \times$  (M0.0AD0.3),  $1 \times$  (M0.0AD1.0),  $3 \times$  (M0.0AD3.0), and  $10 \times$  (M0.0AD10.0) the standard value. The choice of the largest AD coefficient is motivated by Zhao et al. (2016, 2018), who showed that the level of AD can be enhanced by 1–2 orders of magnitude when small grains are depleted. We will first survey the broad trends (Section 6.4.1) before diving into detailed discussions of how AD affects the protostellar accretion flow relative to the ideal MHD case (Section 6.4.2) and the reasons behind the trends identified (Section 6.4.3).

### 6.4.1 Overview of results

To get a first impression on how AD affects the dynamics of core collapse and disk formation, we plot in Figs 6.6 and 6.7, respectively, the column density maps and the mass-weighted infall and rotational speeds as a function of radius for the material on the equatorial plane for all non-turbulent AD models (rather than within a wedge of  $45^\circ$  of the equatorial plane as in Fig. 6.4 since the pseudo-disk here is not warped by turbulence) at five epochs when the stellar mass  $M_* = 0.1, 0.15, 0.2, 0.25,$  and  $0.3 M_\odot$ . From the left-most column of the column density maps, it is clear that the least magnetic diffusive model, M0.0AD0.1, does not show any evidence of a well-formed disk, especially at later epochs, when the appearance of the circumstellar region is dominated by low-density, expanding regions (i.e. DEMS). The lack of a rotationally supported structure is corroborated by the velocity profiles displayed as violet solid curves in the Fig. 6.7, which show that the rotation is significantly sub-Keplerian on the 100-AU scale at the earliest epoch (when  $M_* = 0.1 M_\odot$ ) and becomes worse at later times, and that the rotational speed is increasingly dominated by the infall speed over time.

As the AD coefficient  $Q_A$  increases from 0.1 to 0.3 times the standard value, the (mass-weighted) rotational speed stays closer to the Keplerian value (compare blue dashed and violet solid curves in Fig. 6.7) until the last epoch (when  $M_* = 0.3 M_\odot$ ), when the rotational speed drops to close to zero and becomes much smaller than the infall speed. At the early epochs, the rotation remains significant, with a speed comparable to the infall speed. However, there is no clear evidence for a rotationally supported structure either from the column density map or velocity profiles for this moderately weak AD case. The appearance of the circumstellar region at the last epoch is dominated by low-density, expanding DEMS, as in the least diffusive model

of M0.0AD0.1.

The appearance of the circumstellar region changes drastically as the AD coefficient  $Q_A$  increases further to the standard value (i.e. Model M0.0AD1.0). As is seen from the middle column of Fig. 6.6, a small dense circumstellar structure is (barely) visible at the earliest epoch ( $M_* = 0.1 M_\odot$ ). It rotates close to the Keplerian value, and appears to be the seed for the larger, more prominent, rotationally supported structure that develops later. The formation of a rotationally dominated (perhaps even supported) structure of  $\sim 30$  AU in radius is evident at the epoch of  $M_* = 0.15 M_\odot$  from the velocity profiles, which show a nearly Keplerian rotation for the structure that clearly dominates the slow (sub-free-fall) infall. This structure is visible in the column density map (see panel h of Fig. 6.6) as the small red region (of high column density) near the sink particle (marked by the white cross). A well-defined dense spiral structure is apparent at the epoch when  $M_* = 0.2 M_\odot$ . The structure becomes more ring-like at even later epochs ( $M_* = 0.25$  and  $0.3 M_\odot$ ), although arm-like features are still visible. There is little doubt that these dense spiral/ring-like structures are rotationally supported, because they rotate at (or slightly above) the Keplerian value and their infall speed is close to zero (well below the infall value; see the green dash-dotted curves in panels c–e of 6.7). Despite the formation of a rotationally supported structure that is absent from the less magnetically diffusive models, Model M0.0AD1.0 retains an important feature of the less diffusive models: the low-density, expanding, DEMS. The co-existence of a rotationally supported disk and DEMS is an interesting new feature that has not been reported in the literature before.

The low-density DEMS all but disappear as the AD coefficient increases further, to 3 and 10 times the standard value (Models M0.0AD3.0 and M0.0AD10.0, respectively). For these more magnetically diffusive cases, the circumstellar region remains

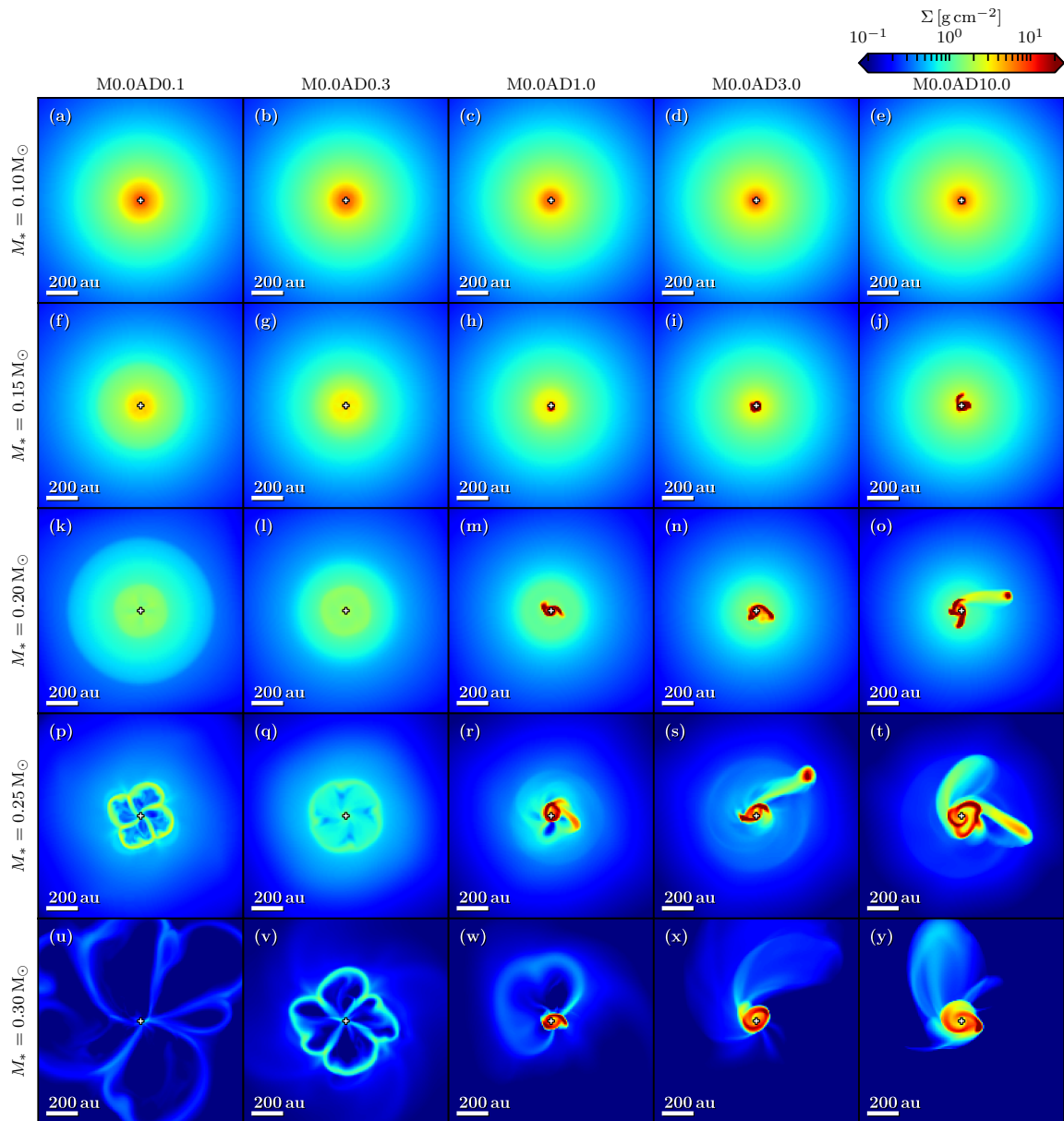


Figure 6.6: Column density along  $z$ -axis of the zoom-in simulations of all non-turbulent AD models with  $Q_A = 0.1\times, 0.3\times, 1\times, 3\times$  and  $10\times$  (left to right) the standard value when the sink particle has accreted  $0.1, 0.15, 0.2, 0.25$  and  $0.3 M_\odot$  (top to bottom). The sink particle is marked by a cross. (See the supplementary material in the online journal for an animated version of the column density distribution for each model.)

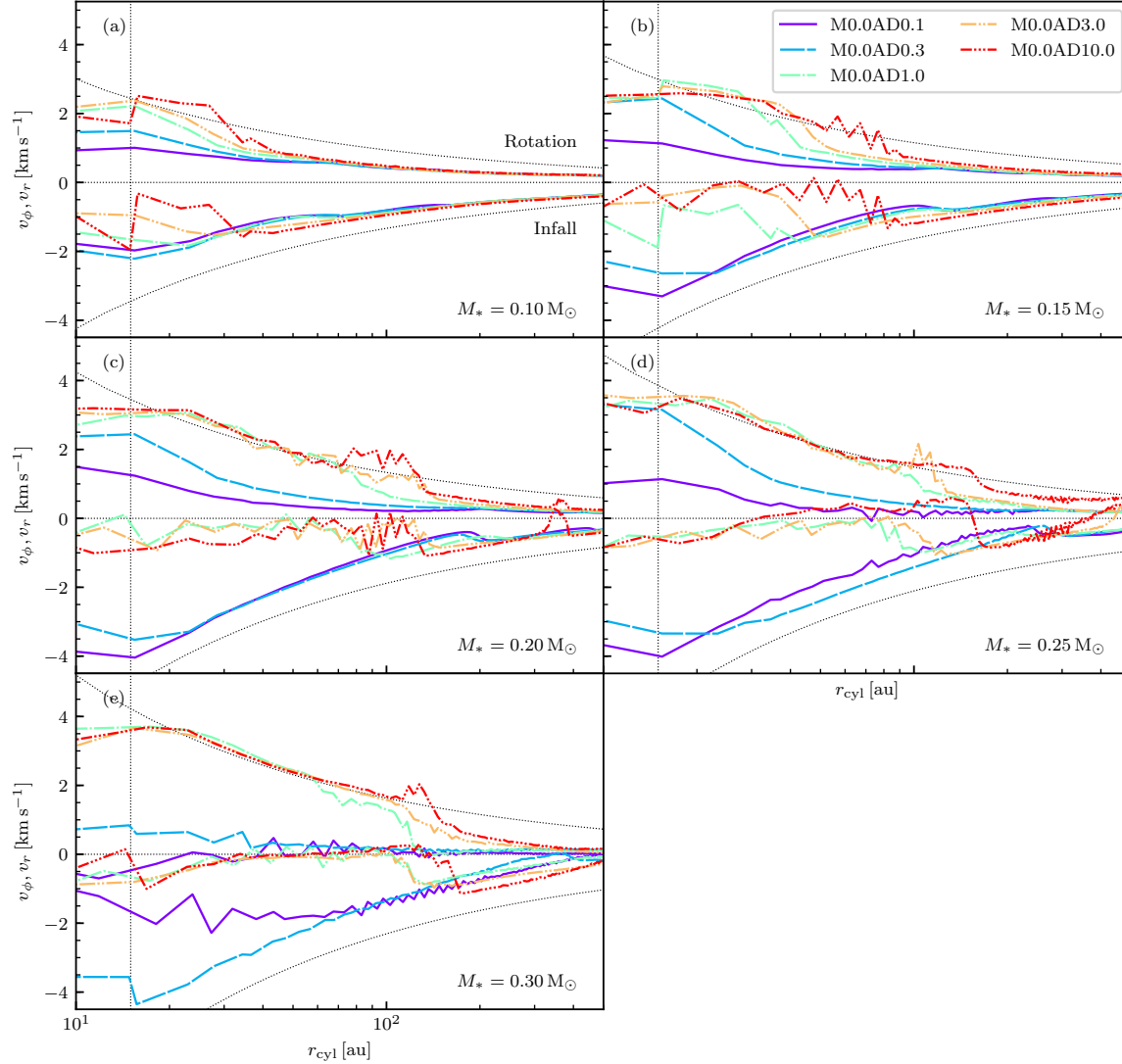


Figure 6.7: Distributions of the mass-weighted rotational (upper curves) and infall speeds (lower) on the equatorial plane compared to the Keplerian (upper black dotted) and free-fall (lower) profile at five representative epochs with stellar mass of  $M_* = 0.1$  (panel a),  $0.15$  (b),  $0.2$  (c),  $0.25$  (d) and  $0.3 M_\odot$  (e) for all non-turbulent AD models with  $Q_A = 0.1 \times$  (violet solid line),  $0.3 \times$  (blue dashed),  $1 \times$  (green dash-dotted),  $3 \times$  (yellow dash-double-dotted), and  $10 \times$  (red dash-triple-dotted) the standard value. The vertical dotted line in each panel denotes roughly the radius of the sink region.

dominated by a rotationally supported structure even at late epochs (see the last two columns of Fig. 6.6). Compared to Model M0.0AD1.0 with the standard AD coefficient, the rotationally supported structures emerge earlier, are larger at the same epoch (with the same  $M_*$ ), and appear to be more gravitationally unstable, as evidenced by the presence of secondary fragments (see e.g. panels o and s). Although more refined treatments, such as radiation hydrodynamics, are required to investigate the process of gravitational fragmentation properly, the broad trend is unmistakable: as the level of AD increases, more angular momentum is retained by the circumstellar material, making the formation of a rotationally supported structure easier. In what follows, we seek to understand the physical reasons behind this trend, starting with a discussion of an AD-induced structure that is absent in the ideal MHD limit.

### 6.4.2 AD-induced diffusion-DEMS

The presence of AD in principle allows the magnetic flux dragged to the vicinity of the protostar to diffuse outwards relative to the protostellar accretion flow, which is a mode of flux redistribution not available in the ideal MHD limit. Li & McKee (1996) showed analytically that the magnetic flux left behind by the accreted stellar material tends to create a circumstellar region of strong magnetic field that is confined by the ram pressure of the accretion flow. The transition between the accretion flow and the circumstellar region dominated by the (AD) redistributed flux is often mediated by a shock of continuous type (C-shock; see Draine & McKee 1993 for a review) although not always. This transition is a key difference between protostellar accretion with AD and in the ideal MHD limit. It has been confirmed in non-ideal MHD simulations in 1D (adopting the so-called “thin-disk” approximation, e.g. Krasnopolsky & Königl 2002; Tassis & Mouschovias 2005), 2D (assuming axisymmetry, e.g. Mellon & Li 2009; Kunz & Mouschovias 2010; Li et al. 2011), but not yet in 3D. Krasnopol-

sky et al. (2012) showed that the AD-induced circumstellar structure found in their 2D (axisymmetric) simulations quickly became unstable when the assumption of axisymmetry is removed. This leaves open the question whether such a structure can ever be produced in 3D in the first place. The answer turns out to be “yes”, as we show next.

The case for the AD-induced structure can be made most clearly in the least diffusive model M0.0AD0.1 at early epochs. There are three lines of evidence supporting this case. First, the model has a clear plateau in the distribution of the vertical magnetic field strength ( $B_z$ ) on the equatorial plane near the centre that is distinct from the surrounding (weaker field) region, as seen pictorially in Fig. 6.8, which plots the maps of  $B_z$  at the same five epochs as in Fig. 6.6. This is further quantified for the representative early epoch  $M_* = 0.15 M_\odot$  in panel (a) of Fig. 6.9, where the azimuthally averaged  $B_z$  is plotted as a function of radius. The magnetic flux threading through this plateau region ( $r \lesssim 125$  AU, the red region in panel b of Fig. 6.8) is about  $1.30 \times 10^{29}$  G cm<sup>2</sup>, which yields a dimensionless mass-to-flux ratio of 3.7 (using  $M_* = 0.15 M_\odot$  as the mass). This ratio is comparable to the mass-to-flux ratio of the central  $0.15 M_\odot$  of the initial core, which is  $\sim 3.1$  if the core collapse is isotropic and  $\sim 6.5$  if the collapse is along the field lines. This agreement lends credence to the notion that the plateau is created mostly by the magnetic flux that is decoupled from, and left behind by, the mass already accreted on to the star. The same holds true for the other two early epochs shown in Fig. 6.8, which correspond to  $M_* = 0.1$  and  $0.2 M_\odot$ , when the dimensionless ratio of the stellar mass to the magnetic flux in the plateau region is 4.8 and 3.6, respectively.

Secondly, in the transition zone between the plateau and its surrounding region (at a radius  $\sim 100$  AU), the infall of the bulk neutral material slows down temporarily, before reaccelerating towards the central protostar (see panel b of Fig. 6.9). The ions,

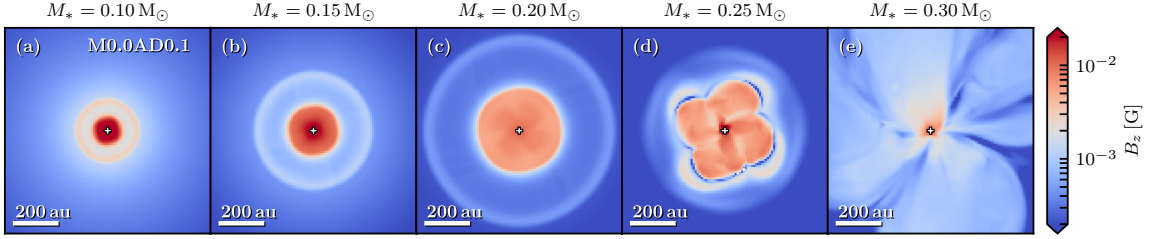


Figure 6.8: Distribution of the vertical magnetic field on the equatorial plane for the least diffusive model M0.0AD0.1 at the epochs when  $M_* = 0.10, 0.15, 0.2, 0.25, 0.3 M_\odot$ , showing a distinct strong-field plateau at early epochs, which is disrupted at later epochs. (See the supplementary material in the online journal for an animated version of the vertical magnetic field strength and column density distribution.)

which are tied to the magnetic field lines, collapse much more slowly than the neutrals inside the plateau, however, which is another characteristic of the AD-induced structure proposed originally by Li & McKee (1996) and found numerically in previous 1D and 2D simulations. Since this strongly magnetized structure is created by flux redistribution by (microscopic) magnetic diffusion, we will refer to it as “diffusion-DEMS”, to distinguish it from the structure created by interchange instability, where magnetic flux is advected outwards by bulk fluid motions of strongly magnetized, low-density regions, which we will sometimes refer to as “advection-DEMS” or just DEMS (since it is the more common of the two types in the current simulations).

Thirdly, at early times when the central stellar mass  $M_*$  is of the order of  $0.1 M_\odot$  or smaller, the magnetic field strength in the diffusion-DEMS agrees to within a factor of 2 with the analytic estimate from Li & McKee (1996) (their equation 7) for the AD-shock based on a balance of the ram pressure of the pre-shock infalling material and the post-shock magnetic pressure. The agreement worsens at later times, when the pre-shock material is confined vertically to a thin layer by the tension force of a highly pinched magnetic field, which is not accounted for in the analytic theory. In such a case, it is more appropriate to exam the balance of forces than pressures.

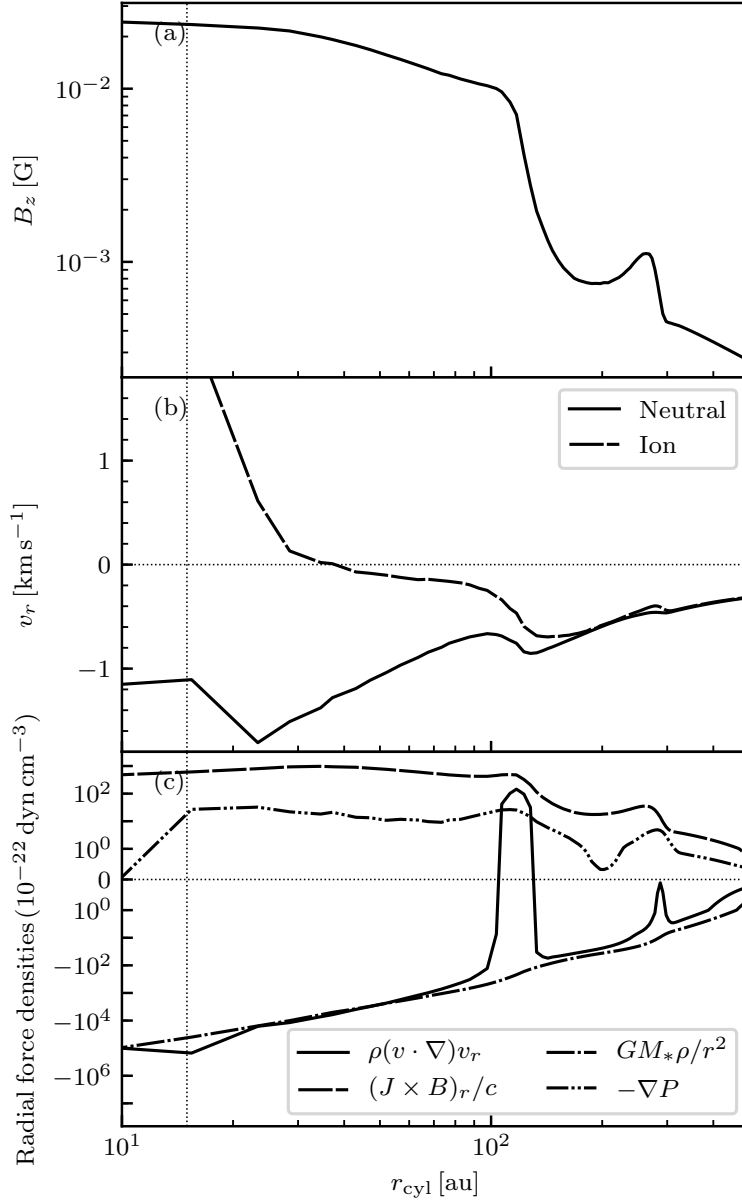


Figure 6.9: AD-induced magnetically dominated circumstellar structure in Model M0.0AD0.1 at a representative epoch when  $M_* = 0.15 M_\odot$ . Plotted are the distributions as a function of radius of (a) the azimuthally averaged vertical magnetic field strength ( $B_z$ ) on the equatorial plane, (b) ion and neutral infall speeds weighted by mass, and (c) the radial component of each of the force terms in the momentum equation (equation 6.2), including the flow acceleration (the solid line), magnetic force (dashed), gravity of the central object (dash-dotted), and the gas pressure gradient (dash-double-dotted). Note that a symmetrical log scale is used for the vertical axis of panel (c), where the range  $[-1, 1]$  is in linear scale to highlight the change of flow acceleration to positive values in the transition region around  $r \sim 100$  AU.

The mechanics of the accretion flow in the equatorial region is illustrated more clearly in panel (c) of Fig. 6.9, which plots the radial components of all force terms in the momentum equation (equation 6.2). It is clear that most of the flow acceleration in the radial direction,  $\rho(\mathbf{v} \cdot \nabla)v_r$  (solid line in the panel), comes from the gravity of the central object (dash-dotted) over most radii. The main exception is near the plateau-surrounding transition region ( $r \sim 100$  AU), where the magnetic force  $(\mathbf{J} \times \mathbf{B})_r/c$  (dashed) and, to a lesser extent, the gas pressure gradient (dash-double-dotted) dominate the gravity and lead to a net outward acceleration, which slows down the accretion flow in the transition region. In other words, the natural tendency for the strong magnetic field in the plateau region to expand is contained by the rapidly collapsing accretion flow.

A strong-field plateau was also found in the AD simulations of Tomida et al. (2015), Masson et al. (2016), and Hennebelle et al. (2016). Hennebelle et al. (2016) found an interesting way to interpret the plateau semi-analytically using a one-dimensional model where the inward advection of the magnetic flux is balanced by the outward diffusion of the flux (see their equation 1). The balance is also one of the basic ingredients of our interpretation, based on the semi-analytic work of Li & McKee (1996), where the neutral material accretes across the magnetic field lines in the diffusion-DEMS (but not necessarily outside this structure), as evidenced by the much slower infall speed of ions (and thus the field lines tied to them) compared to that of neutrals (see panel b of Fig. 6.9). Our interpretation goes one step further and envisions the diffusion-DEMS (or the plateau region) as a region distinct from its surroundings, with a sharp drop in field strength between the two, especially at relatively early epochs (see the first three panels of Fig. 6.8). The drop introduces an outward magnetic force which, in our picture, is reflected in the deceleration of the surrounding accretion flow. This confinement of a lighter fluid (the magnetic field)

by a heavier fluid in the presence of the gravity of the central star has long been suspected to be unstable to interchange instabilities (e.g. Li & McKee 1996; Stehle & Spruit 2001). It is indeed the case, as we show next.

The development of the interchange instability can be seen most clearly in the animations of the distributions of the mid-plane vertical magnetic field strength ( $B_z$ ) and the surface density  $\Sigma$  side-by-side (see online complementary materials or compare the first column of Fig. 6.6 to that of Fig. 6.8). The animations show that noticeable azimuthal variations start to develop inside the diffusion-DEMS for both  $B_z$  and  $\Sigma$  around the epoch when  $M_* = 0.2M_\odot$ , with the two variations anti-correlated. The variations become more prominent at later epochs, with denser, less magnetized “fingers” infalling towards the central protostar along some azimuthal directions, and less dense but more strongly magnetized pockets expanding away from the central object (see e.g. panel p of Fig. 6.6 and panel d Fig. 6.8), as expected for interchange instability, which is a form of the Rayleigh–Taylor instability. The infalling heavier Rayleigh–Taylor “fingers” deliver both matter and magnetic flux to the central sink region, where the mass is accreted on to the sink particle while the magnetic flux is left behind. Magnetic pressure builds up in the sink region, which is released along the directions of least resistance, driving the expansion of the low-density pockets between the dense infalling “fingers”. Fueled by the magnetic flux released by the accreted mass and the decline of the density of the confining medium, the strongly magnetized, low-density pockets expand quickly at later times, as illustrated in the panel (u) of Fig. 6.6 and panel (e) of Fig. 6.8 (when  $M_* = 0.3M_\odot$ ). Again, the variations of the surface density and  $B_z$  are strongly anti-correlated. At such times, the circumstellar region is essentially a mixture of the diffusion-DEMS (driven by the AD-enabled flux redistribution at earlier times) and the advection-DEMS (fueled by

the flux released in the sink region at later times).<sup>2</sup>

### 6.4.3 Ambipolar diffusion and disk formation

In this subsection, we will explore how the AD affects the angular momentum evolution of the protostellar accretion flow compared to the ideal MHD case and how the formation of large disks is enabled by a relatively high ambipolar diffusivity.

We have already seen in Section 6.3 that the laminar ideal MHD model M0.0AD0.0 does not form a large rotationally supported structure because of efficient magnetic braking of the protostellar accretion flow. Part of the reason for the efficient braking comes from a rapid increase of the (vertical) magnetic field strength on the equatorial plane ( $B_z$ ) towards the protostar, as illustrated in panel (a) of Fig. 6.10 (black-solid curve). This, coupled with a significant pinching of the field lines in the azimuthal direction (or a strong radial current density  $J_r$ ), gives rise to a large magnetic braking torque ( $\propto B_z J_r$ ) that removes angular momentum from the infalling protostellar envelope efficiently (through a braking-driven outflow).

In the presence of even a weak ambipolar diffusivity, the magnetic field distribution in the circumstellar region is modified significantly, as discussed in the last subsection. Specifically, an ambipolar diffusivity that is 10 times less than the standard value (Model M0.0AD0.1) is enough to limit the increase of  $B_z$  towards the protostar, and produce a plateau region of more or less constant  $B_z$  – the diffusion-DEMS. As a result, the protostellar accretion flow is less braked in Model M0.0AD0.1 compared to the ideal MHD model M0.0AD0.0 (compare the black solid and violet dashed curves in panel c of Fig. 6.10). The weaker braking allows the accretion flow to retain more angular momentum, as can be seen by comparing the violet solid curves

---

<sup>2</sup>We note that the flux decoupling inside the sink region is ultimately achieved through magnetic diffusion as well, so the advection-DEMS is also driven by magnetic diffusion on scales smaller than the DEMS themselves.

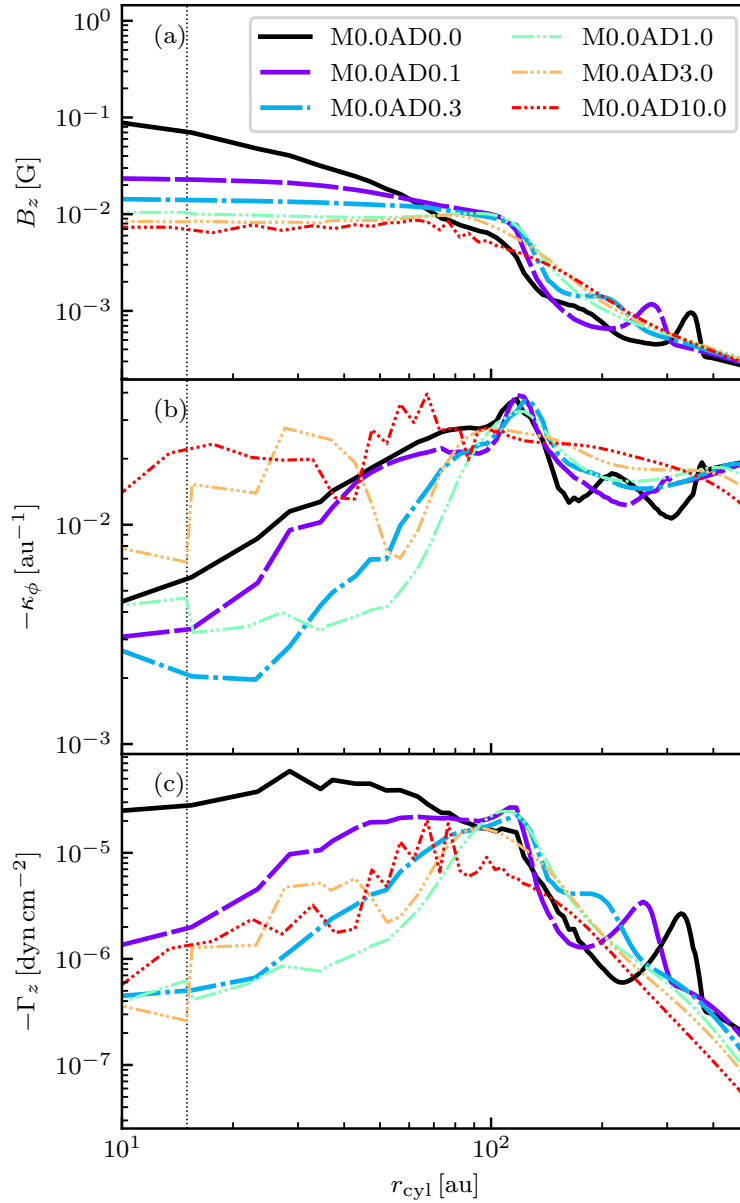


Figure 6.10: Effects of AD on the magnetic field strength and structure, and the magnetic braking efficiency. Plotted are the distributions of (a) the azimuthally averaged vertical magnetic field strength  $B_z$ , (b) the degree of pinching of the magnetic field lines (see equation 6.10 for a definition) in negative  $\phi$ -direction, and (c) the magnetic braking torque  $-\Gamma_z = (1/c)[(\mathbf{J} \times \mathbf{B}) \times \mathbf{r}]_z$ , on the equatorial plane at a representative epoch when  $M_* = 0.15 M_\odot$ . The curves in each panel correspond to the models with  $Q_A = 0.0$  (black solid line), 0.1 (violet dashed), 0.3 (blue dash-dotted), 1.0 (green dash-double-dotted), 3.0 (yellow dash-triple-dotted) and 10.0 (red dash-quadruple-dotted), respectively.

in panels a and c of Fig. 6.7 to those in panels a and b of Fig. 6.4, respectively.

Despite the reduction in magnetic braking efficiency, this least diffusive model (M0.0AD0.1) does not retain enough angular momentum to form a large rotationally supported structure. As the ambipolar diffusivity increases by a factor of 3–0.3 times the standard value (Model M0.0AD0.3), the situation remains qualitatively similar, with the circumstellar region dominated by a well-defined diffusion-DEMS at early epochs and by the development of interchange instabilities at later times (see the second column of Fig. 6.6). Quantitatively, the increase in AD coefficient causes a further reduction in the vertical field strength  $B_z$  in the circumstellar diffusion-DEMS (compare the blue dash-dotted and violet dashed curves in panel a of Fig. 6.10). Just as importantly, the circumstellar field lines are significantly less pinched, especially in the azimuthal direction.

To measure the pinching of the field lines quantitatively, we consider the magnetic field curvature:

$$\kappa = \frac{\mathbf{B}}{B} \cdot \nabla \frac{\mathbf{B}}{B}. \quad (6.10)$$

In particular, the  $\phi$ -component of the curvature,  $\kappa_\phi$ , measures the degree of field line pinching in the azimuthal direction, which is directly tied to magnetic braking. It is significantly smaller for Model M0.0AD0.3 than for Model M0.0AD0.1 within the diffusion-DEMS, as shown in panel (b) of Fig. 6.10 (compare the blue dash-dotted and violet dashed curves). The combination of a weaker and less azimuthally pinched magnetic field reduces the efficiency of magnetic braking in Model M0.0AD0.3 further compared to Model M0.0AD0.1 (compare the blue dash-dotted and violet dashed curves in panel c). However, the reduction is still not enough to enable the formation of a large rotationally supported structure in this relatively weak AD case.

As the AD coefficient increases further from 0.3 to 1.0 times the standard value,

a rotationally supported structure is formed, as a result of further weakening of the magnetic braking by a somewhat weaker and substantially less azimuthally pinched circumstellar magnetic field (compare the green dash–double-dotted and blue dash–dotted curves in Fig. 6.10). The situation with the more magnetically diffusive cases of M0.0AD3.0 and M0.0AD10.0 is qualitatively similar, with the magnetic braking weakened enough to allow for large disk formation. Quantitatively, the rotationally supported structures form at earlier epochs. Note that the magnetic field lines near the protostars are actually more pinched in these two highly diffusive models compared to the standard AD one because of the increased rotational speed (compare, for example, the yellow dash–triple-dotted and green dash–double-dotted curves in panel b of Fig. 6.10). Nevertheless, the magnetic braking remains weak enough for the large rotationally supported structure to persist until the end of the simulation.

## 6.5 DISK FORMATION WITH TURBULENCE AND AMBIPOLAR DIFFUSION

In the last two sections, we have explored separately the effects of turbulence and AD on disk formation. Here we study the combined effects of these two physical ingredients, focusing on the cases with a sonic turbulence (with Mach number  $\mathcal{M} = 1$ ) and a range of ambipolar diffusivity, from 0.1 to 10 times the standard value. The results are shown in Figs 6.11 and 6.12, which plot, respectively, the surface density and the radial profiles of the mass-weighted infall and rotational speeds at four representative epochs when  $M_* = 0.1, 0.15, 0.2$  and  $0.25 M_\odot$ . It is immediately apparent that well-formed disks are present at the earliest epoch shown ( $M_* = 0.1 M_\odot$ ) for all five models independent of the values of AD coefficients, both in morphology (the first row of Fig. 6.11) and in kinematics (with rotational speed close to the Keplerian

value, and much larger than the infall speed; see panel a of Fig. 6.12). This is very different from the laminar ( $\mathcal{M} = 0$ ) cases where, at the same epoch, a rotationally supported structure either does not exist (see panels a and b of Fig. 6.6 and the curves plotted in violet solid and blue dashed line in panel a of Fig. 6.7) or is barely visible (see the right three panels of the same row of Fig. 6.6 and the rest of the curves in Fig. 6.7). This is clear evidence that turbulence is beneficial to disk formation, at least at early epochs, independent of the strength of AD. It is consistent with the results discussed in Section 6.3 for the ideal MHD cases.

Whether the rotationally supported structure formed at early epochs can persist to later times or not depends on the value of the AD coefficient. In Section 6.3, we have already seen that the rotationally supported structure formed early in the ideal MHD sonic turbulence model M1.0AD0.0 disappears at later times, with the circumstellar region becoming increasingly dominated by strongly magnetized, low-density (advection-)DEMS. This behavior is preserved qualitatively for the two weakest AD cases (Model M1.0AD0.1 and M1.0AD0.3), where the well-defined rotationally supported disk at the epoch  $M_* = 0.1 M_\odot$  becomes severely disrupted by the epoch  $M_* = 0.15 M_\odot$  and almost completely disappears by the epoch  $M_* = 0.2 M_\odot$  (see the left two columns of Fig. 6.11 and the purple and blue lines in panels c and d of Fig. 6.12). This late-time behavior is broadly similar to that of the corresponding laminar AD cases (Model M0.0AD0.1 and M0.0AD0.3), although it is easier to observe the development of magnetic interchange instability in the laminar cases, and their circumstellar regions are dominated by the DEMS to a larger extent at late epochs. For these two weakest AD cases, the sonic turbulence produces only initial transient disks, as in the ideal MHD case.

To produce a large, persistent, rotationally supported structure, a relatively strong AD is needed, with or without turbulence. The formation of such a structure in the

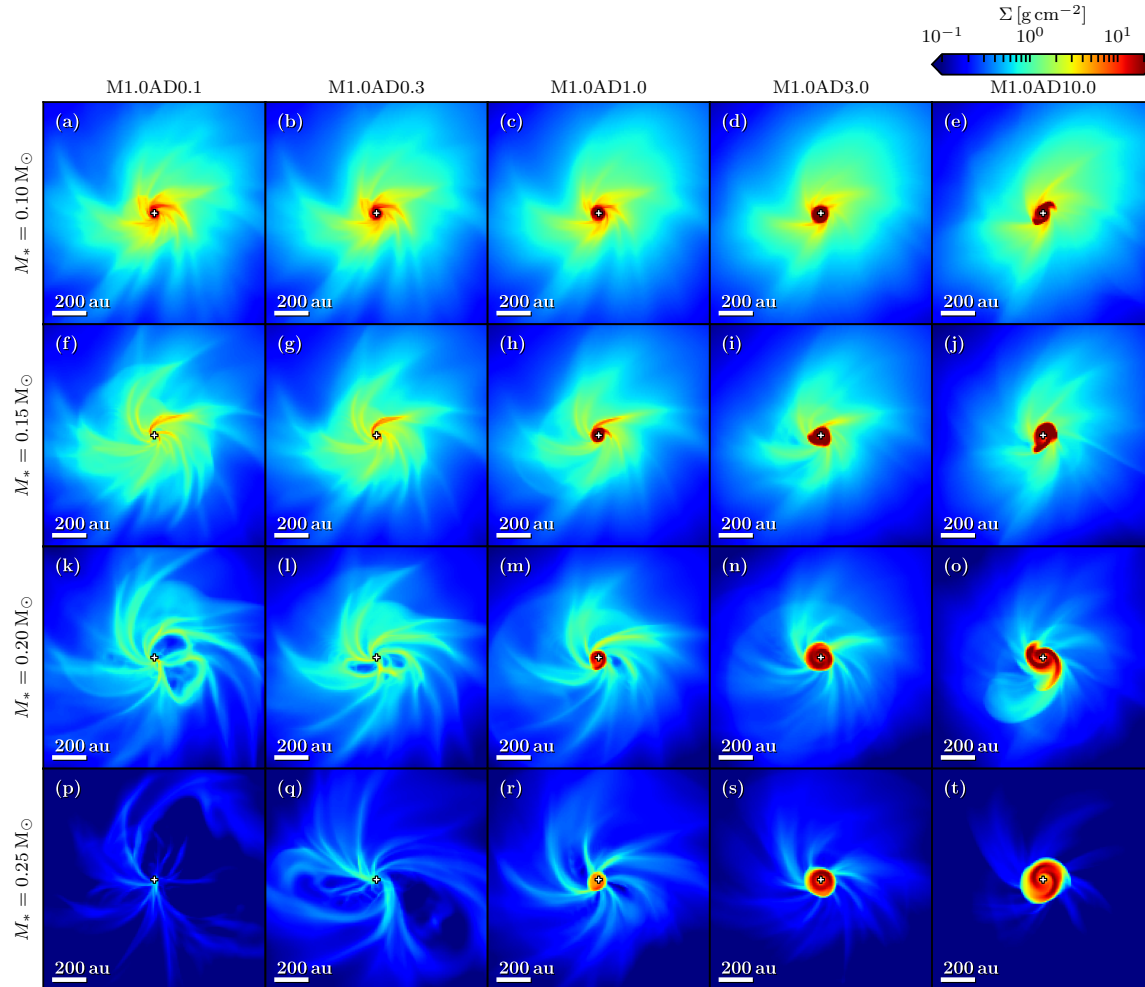


Figure 6.11: Column density along  $z$ -axis of the zoom-in simulations of five sonic-turbulent AD models with  $Q_A = 0.1\times, 0.3\times, 1\times, 3\times$  and  $10\times$  (left to right) the standard value when the sink particle has accreted 0.1, 0.15, 0.2 and 0.25  $M_\odot$  (top to bottom). The sink particle is marked by a cross. (See the supplementary material in the online journal for an animated version of the column density distribution of each model.)

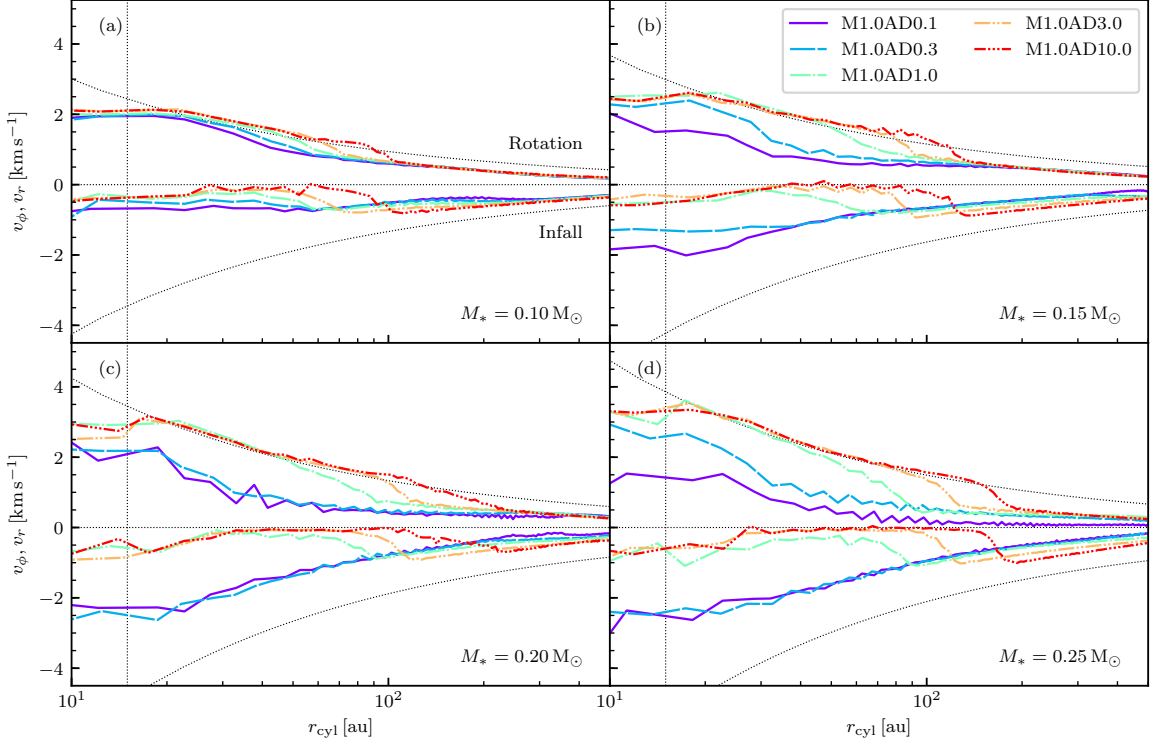


Figure 6.12: Distributions of the mass-weighted rotational (upper curves) and infall speeds (lower) in a wedge within  $45^\circ$  of the equatorial plane compared to the Keplerian (upper black dotted) and free-fall (lower) profile at five representative epochs with stellar mass of  $M_* = 0.1$  (panel a),  $0.15$  (b),  $0.2$  (c) and  $0.25 M_\odot$  (d) for all sonic turbulence AD models with  $Q_A = 0.1\times$  (violet solid line),  $0.3\times$  (blue dashed),  $1\times$  (green dash-dotted),  $3\times$  (yellow dash-double-dotted) and  $10\times$  (red dash-triple-dotted) the standard value. The vertical dotted line in each panel denotes roughly the radius of the sink region.

laminar cases with AD coefficient of 1.0, 3.0, and 10.0 times the standard value has already been discussed in the last section (see the last three columns of Fig. 6.6). For these cases of relatively strong AD, the sonic turbulence makes the small rotationally supported structure at early epochs (e.g.  $M_* = 0.1$  and  $0.15 M_\odot$ ) much more prominent and better defined compared to the laminar cases (contrast the first two panels of the last three columns of Figs 6.6 and 6.11). In addition, the turbulence appears to have made the rotationally supported structure more stable against gravitational fragmentation, judging from the absence of prominent fragments that are prevalent in the corresponding laminar cases at later epochs. Part of the reason is likely that the disk produced in the presence of turbulence is already highly structured (and more strongly magnetized; see Section 6.6 below) to begin with, which facilitates the redistribution of angular momentum inside the disk and lessens the need for strong spirals to develop gravitationally to transport angular momentum. In any case, we have shown that AD and turbulence work together constructively to form large, persistent, stable disks throughout the protostellar accretion phase, with the turbulence making the disk formation easier at early epochs and AD making it easier for the disks to survive to later epochs.

As in the ideal MHD case, the promotion of disk formation at early times by turbulence in the AD cases is facilitated by the warping of pseudo-disks. The warp is illustrated in Fig. 6.13, which plots the density distribution on a cylinder of a representative radius  $r_{\text{cyl}} = 250 \text{ AU}$  at the epoch  $M_* = 0.1 M_\odot$  for the cases with AD coefficient of 0.1, 1.0 and 10.0 times the standard value. These are to be compared with panel (c) of Fig. 6.2 for the ideal MHD case. As the AD coefficient increases, the warped pseudo-disk appears somewhat thicker, which is understandable since the field lines are expected to be less pinched across the pseudo-disk, leaving it less magnetically compressed. Nevertheless, the AD of the levels considered in this paper

does not fundamentally change the basic picture of a flattened pseudo-disk as the backbone of the protostellar accretion flow and its warping (but not complete disruption) by turbulence. The beneficial effects of pseudo-disk warping in disk formation as discussed for the ideal MHD case in Section 6.3, including self-sorting of materials of different specific angular momenta and easier escape of trapped magnetic flux, are therefore preserved.

The early formation of a large, rotationally supported disk enabled by turbulence is expected to affect the diffusion-DEMS formed in the laminar AD simulations discussed in Section 6.4.2. This interesting structure was particularly well defined in the weakest AD model of M0.0AD0.1 at early epochs (see Fig. 6.8). In the presence of a relatively weak turbulence of  $\mathcal{M} = 0.1$  (Model M0.1AD0.1), the strong-field plateau region (the diffusion-DEMS) at the earliest two epochs is significantly perturbed but not destroyed, as illustrated in the upper row of Fig. 6.14, which plots the distributions of the vertical component of the magnetic field on the equatorial plane ( $B_z$ ) at four representative epochs when  $M_* = 0.1, 0.15, 0.2,$  and  $0.25 M_\odot$ . In addition, the ring-like structure outside the diffusion-DEMS at intermediate epochs for the laminar case (see panels b–d of Fig. 6.8) where the vertical field strength is locally enhanced is largely preserved (although significantly perturbed, see panels b–d of Fig. 6.14), again indicating that the weak turbulence does not change the flow structure fundamentally. Nevertheless, it does produce an azimuthal variation that appears to have accelerated the development of the interchange instability which, as in the laminar case, dominates the circumstellar region at late epochs, as shown more clearly in the surface density maps plotted in the lower row of Fig. 6.14. In this case, the combination of a weak turbulence and a weak AD was not able to enable the formation of a large, well-defined disk. The situation is broadly similar for the somewhat stronger turbulence model of M0.3AD0.1 (with  $\mathcal{M} = 0.3$ ), where the diffusion-DEMS is harder

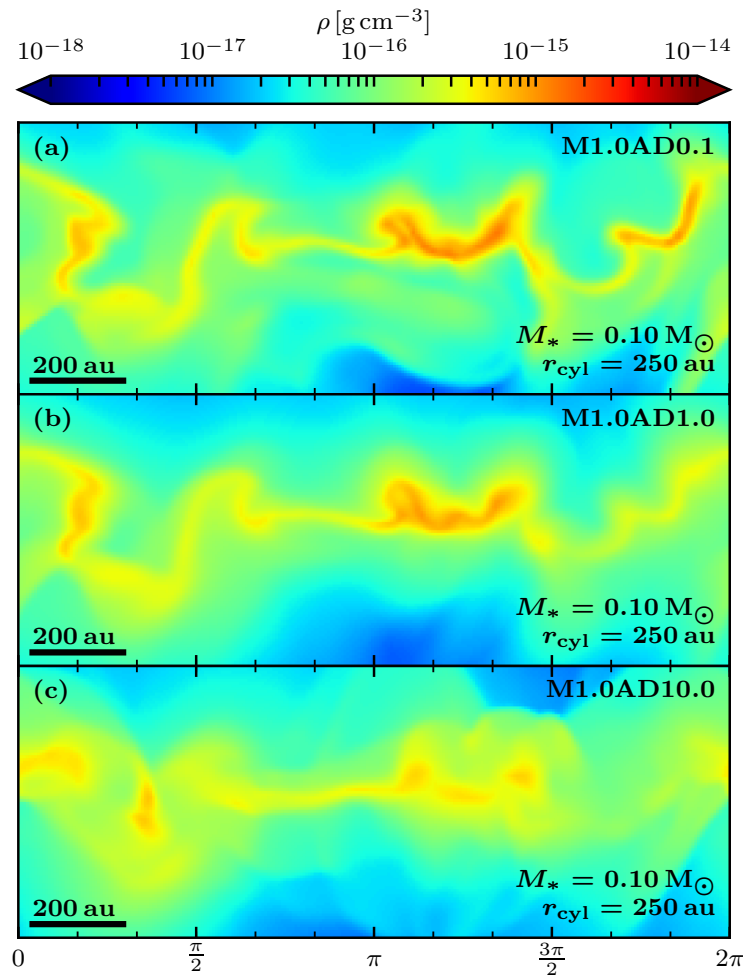


Figure 6.13: Turbulence-induced pseudo-disk warping with AD. Plotted are the density distributions on a cylinder of radius  $r_{\text{cyl}} = 250 \text{ AU}$  at the epoch when  $M_* = 0.1 M_\odot$  for Model M1.0AD0.1 (panel a), M1.0AD1.0 (b), and M1.0AD10.0 (c) as a function of azimuthal angle  $\phi$  and height  $z$ , showing a thicker pseudo-disk as the AD coefficient increases.

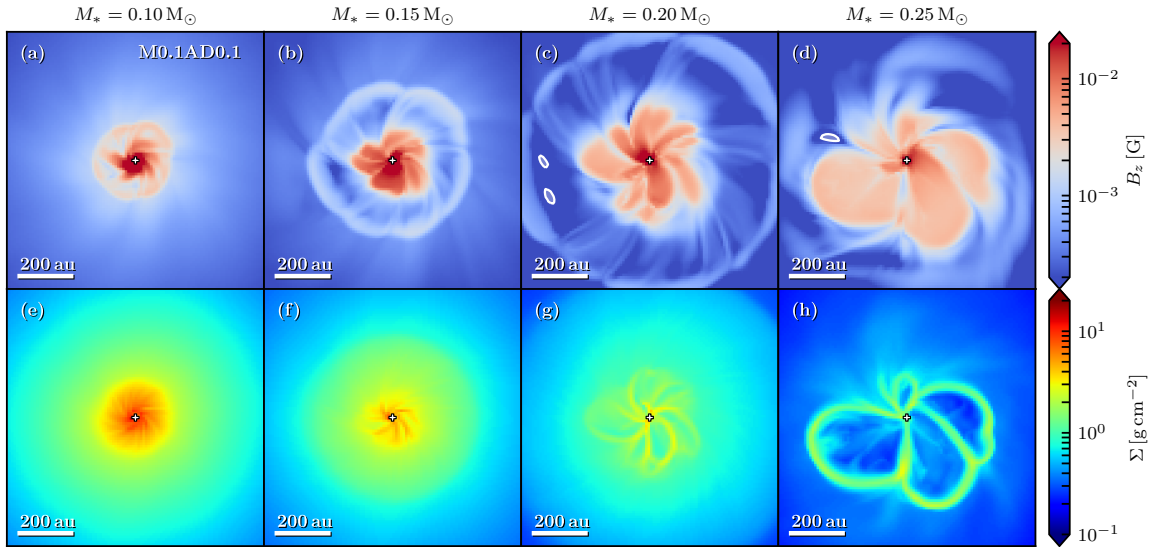


Figure 6.14: Distribution of the vertical magnetic field on the equatorial plane (top panels) and the column density (bottom panels) for the weak turbulence and weak AD model (M0.1AD0.1) at the epochs when  $M_* = 0.05, 0.1, 0.15, 0.2, 0.25 M_\odot$ , showing a distinct strong-field plateau at early epochs, which is disrupted at later epochs. (See the supplementary material in the online journal for an animated version of the vertical magnetic field strength and column density distribution.)

to identify (not shown) and a rotationally supported structure remains absent. As the turbulence level increases to the sonic value ( $\mathcal{M} = 1$ ), the diffusion-DEMS is no longer clearly visible; the circumstellar region at the earliest epoch is dominated by a transient rotationally supported structure instead (see the left column of Fig. 6.11).

## 6.6 DISCUSSION

### 6.6.1 How strongly magnetized are protostellar disks?

It is widely believed that a main driver of disk evolution is the magnetic field, through either the magneto-rotational instability (Balbus & Hawley 1991) or a magnetic disk-wind (Blandford & Payne 1982). How fast the disk evolves depends on the degree of disk magnetization, especially the strength of the poloidal magnetic field threading the disk. For example, in the 2D (axisymmetric) non-ideal MHD simu-

lations of Bai (2017), a mid-plane plasma- $\beta$  of  $10^5$  for the initial poloidal magnetic field is enough to drive an accretion rate of order  $10^{-8} M_{\odot} \text{yr}^{-1}$ , typical of classical T Tauri stars. The rate is increased to  $\sim 10^{-7} M_{\odot} \text{yr}^{-1}$  when the initial poloidal field strength is increased by a factor of  $\sqrt{10}$ , corresponding to a plasma- $\beta$  of  $10^4$ . The degree of disk magnetization is currently a critical free parameter in modeling the dynamics of protoplanetary disks that is unfortunately difficult to measure observationally. Theoretically, it is expected to be determined by the amount of magnetic flux carried into the disk during its formation out of the dense molecular cloud cores, which are known to be significantly magnetized, and the subsequent magnetic flux transport within the disk (e.g. Okuzumi et al. 2014). Determining the initial degree of magnetization of protostellar disks is therefore a central task of magnetized disk formation calculations. In this subsection, we will take a first step in this direction.

To quantify the disk properties, particularly its degree of magnetization, we need to determine which simulation cells belong to the disk. We will adopt the criteria used in Masson et al. (2016), which are

1. the material in the cell is close to the hydrostatic equilibrium in the  $z$ -direction so that the rotational speed is significantly greater than the vertical speed ( $v_{\phi} > f|v_z|$ );
2. it is rotationally supported against infall so that the rotational speed is significantly greater than the radial speed ( $v_{\phi} > f|v_r|$ );
3. it is significantly dominated by rotational support instead of thermal support ( $\rho v_{\phi}^2/2 > fP$ );
4. it has high density ( $\rho > 3.8 \times 10^{-15} \text{g cm}^{-3}$ ).

Following Masson et al.(2016, see also Gray et al. 2018), we will choose a value of

2 for the factor  $f$ , which ensures that the quantities to be compared are significantly different. The results are shown in Figs 6.15 and 6.16.

In Fig. 6.15, we plot the column density along the  $z$ -axis for the “disk cells” selected based on the above criteria for all non-turbulent ( $\mathcal{M} = 0$ ) models that have a wide range of values for the AD coefficient, from  $Q_A = 0$  (ideal MHD, the leftmost column) to 10 (rightmost column), at five different epochs (the last epoch was not reached in the ideal MHD case where the mass in the simulation box is significantly depleted by a magnetic braking driven outflow). Also shown for each model and each epoch are the number of disk cells and the total mass in these cells. Obviously as the number of disk cells increases, the disk becomes better defined, although the boundary between a disk and not a disk is somewhat arbitrary. For definiteness, we will refer to a structure with less than 50, between 50 and 100, and more than 100 disk cells as “no disk”, “underdeveloped disk”, and “well-developed disk” (or “disk” for short), respectively. Based on this definition, we find no discernible disk at any epoch for the laminar ideal MHD (Model M0.0AD0.0) and laminar, relatively weak AD (M0.0AD0.1 and M0.0AD0.3) models (see the first three columns in Fig. 6.15).

A well-developed disk does appear in the standard AD coefficient case (M0.0AD1.0), at the epoch when  $M_* = 0.2 M_\odot$  (panel p) and later. For such well-developed disks, we characterize their degree of magnetization through two dimensionless numbers: the normalized ratio of the disk mass to the magnetic flux threading the disk,  $\lambda_d$ , and the plasma- $\beta$  (the ratio of thermal to magnetic pressure), both noted in Fig. 6.15. The former is to be compared to the mass-to-flux ratio of the initial cloud core, which is  $\lambda_{\text{core}} = 2.6$  globally. For the standard AD case under discussion, we find  $\lambda_d = 18$  at the epoch when  $M_* = 0.2 M_\odot$ . It is much higher than  $\lambda_{\text{core}}$ , indicating that the newly formed disk is much less magnetized relative to its mass compared to its parental core, presumably because of the action of AD, which is expected to redistribute the mag-

netic flux outwards, away from the high-density circumstellar region. Nevertheless, this disk is still significantly magnetized, as reflected in the value of the plasma- $\beta$ , which is 14 at this epoch. This value, while much larger than that for the initial core as a whole ( $\beta_{\text{core}} = 1.9$ ), is much smaller than what is typically adopted in MHD simulations of protoplanetary disks, as mentioned earlier. Interestingly, the magnetic energy is dominated by the poloidal component of the magnetic field rather than the toroidal component, as shown by the values of  $\beta_t$  and  $\beta_p$  in Fig. 6.15 for each disk, which are the ratios of the thermal to magnetic energy due to the toroidal and poloidal field component, respectively. The disk remains significantly magnetized at later epochs. The values of  $\lambda_d$  and  $\beta$  are formally 9.2 and 2.5, respectively, at the epoch when  $M_* = 0.25 M_\odot$ , smaller than their counterparts at the earlier epoch of  $M_* = 0.2 M_\odot$ , but they are affected by a relatively low density region that satisfies the disk criteria but is detached from the main body of the disk (see panel v of Fig. 6.15). By the last epoch shown (panel aa,  $M_* = 0.3 M_\odot$ ), the disk has  $\lambda_d = 23$  and  $\beta = 7.7$ , with the magnetic energy strongly dominated by the poloidal field component.

As the AD coefficient increases, the disk starts to form earlier. For example, by the epoch when  $M_* = 0.15 M_\odot$ , a disk is already well-developed in the most magnetically diffusive model (M0.0AD10.0, panel l), clearly visible although underdeveloped in the second most diffusive model (M0.0AD3.0, panel k), but barely discernible in the standard AD case (panel j). Another trend is that, as the AD coefficient increases, the disk is somewhat bigger (compare the disks in the last three columns of Fig. 6.15) and more massive, with the disk mass increasing from  $\sim 0.02 M_\odot$  for Model M0.0AD1.0 to  $\sim 0.03 M_\odot$  for M0.0AD3.0 to  $\sim 0.04 M_\odot$  for M0.0AD10.0. The disk remains significantly magnetized, with  $\lambda_d \sim 10 - 20$  and  $\beta \sim 10 - 20$  typically, and the magnetic energy dominated by the poloidal field component in most cases. The main exception is the last epoch of the most diffusive model (M0.0AD10.0,  $M_* = 0.3 M_\odot$ ), when the

disk is significantly less magnetized, with  $\lambda_d = 32$ ,  $\beta = 59$ , and the magnetic energy dominated by the toroidal field component instead.

Turbulence changes the formation and properties of disks substantially, as illustrated by Fig. 6.16, which is the same as Fig. 6.15 but for all models with sonic turbulence ( $\mathcal{M} = 1$ ) and different levels of AD. The change is the most pronounced at the earliest epoch ( $M_* = 0.1 M_\odot$ ), when the disk is well developed in all AD models and is clearly visible (although underdeveloped) even for the ideal MHD case (panel a). The ideal MHD disk is strongly magnetized, with  $\lambda_d = 3.8$  that is comparable to that of its parental core (especially the central part that is less magnetized compared to the core as a whole) and a plasma- $\beta$  that is much less than unity ( $\beta_d = 0.1$ ). The strong magnetization, we believe, is the reason that the disk enabled by turbulence early in the ideal MHD case is transient; the magnetic braking is simply too efficient to allow the disk to persist for a long time. The same is broadly true for the early disks formed in the two weakest AD cases (Model M1.0AD0.1 and M1.0AD0.3), even though their masses ( $0.003$  and  $0.008 M_\odot$ ) are significantly larger than that of the ideal MHD disk ( $0.001 M_\odot$ ); both disks disappear at later epochs.

The early disk enabled by turbulence does survive to the last epoch shown in Fig. 6.16 ( $M_* = 0.3 M_\odot$ ) in the standard AD model of M1.0AD1.0. However, even in this case where a disk is formed without turbulence, the properties of the disk, especially its magnetization, are strongly affected by the turbulence. Similar to the ideal MHD and the two weakest AD cases, the early disk is strongly magnetized, with  $\beta = 0.81$  and  $0.94$  at the epochs  $M_* = 0.1$  and  $0.15 M_\odot$  respectively (see panels d and j). The order-of-unity disk plasma- $\beta$  persists to the later epoch of  $M_* = 0.2 M_\odot$ , when  $\beta = 1.6$ . This value is much smaller than that for the corresponding non-turbulent model at the same epoch, where  $\beta = 14$ . The stronger magnetization induced by turbulence is expected to make it more difficult for the

disk to survive. This is indeed true for the standard AD case, where the disk mass is reduced by more than a factor of 2 (from  $0.014$  to  $0.006 M_{\odot}$ ) between the last two epochs ( $M_* = 0.2$  and  $0.25 M_{\odot}$ ). Indeed, the disk disappears completely at even later epochs (not shown). In this particular case, the turbulence not only enabled the earlier formation of the disk, but also made the disk more strongly magnetized and thus harder to survive. This negative effect of turbulence on the long-term survivability of AD-enabled disks is a new phenomenon that has not been seen before.

The reduction of disk plasma- $\beta$  by turbulence is also evident in the stronger AD models of M1.0AD3.0 and M1.0AD10.0. For example, at the epoch when  $M_* = 0.2 M_{\odot}$ , the well-developed disks in the laminar Model M0.0AD3.0 and M0.0AD10.0 have  $\beta = 9.4$  and  $21$ , respectively. When a sonic turbulence is present, these values are reduced by roughly a factor of 2, to  $4.2$  for Model M1.0AD3.0 and  $14$  for Model M1.0AD10.0, respectively. Nevertheless, these significantly magnetized disks are able to survive to the end of the simulation, unlike the standard AD case.

Another interesting effect is that, for the more magnetically diffusive cases where disk formation can be enabled by AD alone, the turbulence makes the disk more stable to violent gravitational instability (which often produces fragments distinct from the main body of the disk in the laminar cases, see e.g. panels s and o of Fig. 6.6). As speculated earlier, part of the reason may be that the turbulence strongly warps the pseudo-disk that feeds the disk, leading to a strong initial inhomogeneity in the disk (including spirals) that facilitates the redistribution of angular momentum which, in turn, lessens the need for violent gravitational instability to do so. Another reason is that the disks formed in the presence of turbulence tend to be more strongly magnetized and thus less prone to gravitational instability. In any case, the combination of a relatively strong turbulence and relatively strong AD appears capable of producing a large, persistent, stable, but significantly magnetized disk.

The significant level of magnetization that we found in the disk formed in the presence of AD and especially turbulence may be a potential problem for the disk evolution in late phases of star formation, particularly the classical T Tauri phase that is generally thought to be crucial to planet formation. While it is reassuring that the disk can inherit a magnetic field from its parental core, our simulations show that the inherited field may be too strong for the protoplanetary disks, with a typical plasma- $\beta \sim 10 - 20$  without turbulence and  $\sim 1 - 10$  with turbulence, and a poloidal field component comparable to, and often larger than, the toroidal field component. These values are orders of magnitude lower than the typical initial values used in global protoplanetary disk simulations ( $\sim 10^4 - 10^5$ ), as mentioned earlier. One empirical constraint on the disk plasma- $\beta$  comes from the measurement of the magnetic field strength of  $\sim 0.54$  G in the Semarkona meteorite (Fu et al. 2014). If we adopt the estimates of the temperature and density distributions for the solar nebula from Desch (2007) and assume that the parent body of the meteorite comes from the main asteroid belt at a radius of  $\sim 2.5$  AU, we obtain a plasma- $\beta$  of  $\sim 700$  in the gas surrounding the meteorite if the field strength in the gas is the same as that in the meteorite. It is, however, possible that the former may be weaker than the latter, by a factor between 1 and 10, if the chondrules are formed in nebular shocks (Desch & Connolly 2002). In this case, the gas plasma- $\beta$  would be in the range of  $\sim 10^3 - 10^5$ , close to the values often adopted in simulations of relatively evolved, protoplanetary disks. This is reassuring since the Semarkona chondrules are thought to form in a rather late stage of the solar nebula evolution, with an inferred age of 2–3 Myr after the formation of the first calcium aluminum-rich inclusions (Mostefaoui et al. 2002). This is much older than the disks studied in this paper, which typically have an age of only a few times  $10^4$  years.

The above result needs to be tested with high resolution simulations that resolve

the disks better. If confirmed, the discrepancy would indicate that, although AD and turbulence can enable disks to form, they may not be able to demagnetize the formed disk enough to satisfy the constraints imposed by the (low) accretion rate and measurements of meteoritic magnetic field strength in late phases. Additional magnetic diffusivities, such as Ohmic dissipation and Hall effect, a detailed treatment of the disk thermodynamics, and longer-term simulations of the disk from its initial formation to the T Tauri phase may be required to resolve the discrepancy.

### 6.6.2 Connection with previous work and future refinement

As discussed in the introduction, the most detailed non-ideal MHD studies of magnetized disk formation to date tend to focus on the early phase up to, and slightly beyond, the formation of Larson’s second core (stellar seed; see recent reviews by Tsukamoto 2016 and Wurster & Li 2018). The focus of this work is on the less well explored protostellar accretion phase, with emphasis on turbulence and AD, which have previously been investigated separately but not in combination thus far.

Our self-gravitating ideal MHD simulations with turbulence (but not AD) can be viewed as an extension of the work by Li et al. (2014b), who studied the simplified problem of the accretion of non-self-gravitating turbulent rotating protostellar envelope on to a star of fixed mass. Our more self-consistent treatment strengthened their general conclusions that the structure of the magnetized protostellar accretion flow is dominated by a turbulence-warped but spatially coherent pseudo-disk, and that the turbulence is beneficial to disk formation. However, there is an important difference: whereas the disk induced by a sonic turbulence in Li et al. (2014b) lasted until the end of their simulation (see also González-Casanova et al. 2016), that in the corresponding model here (Model M1.0AD0.0) is more transient and becomes disrupted by DEMS at late epochs (see the right column of Fig. 6.1). The exact reason for this

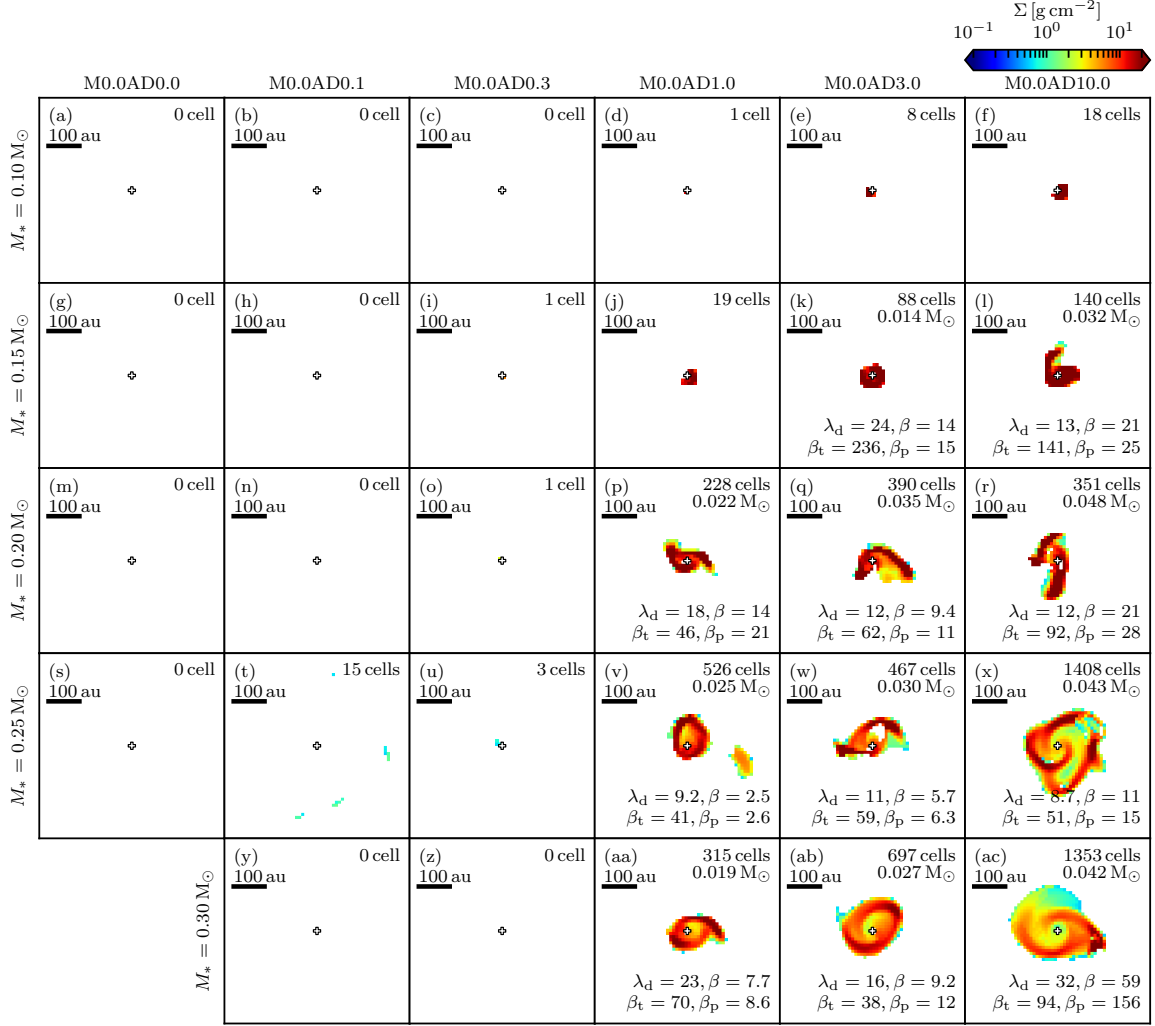


Figure 6.15: Column density of cells identified as a part of the disk along  $z$ -axis of all non-turbulent AD models with  $Q_A = 0.0\times, 0.1\times, 0.3\times, 1\times, 3\times,$  and  $10\times$  (left to right) the standard value when the sink particle has accreted  $0.1, 0.15, 0.2, 0.25,$  and  $0.3 M_\odot$  (top to bottom). The sink particle is marked by a cross. The number of cells is written on the upper right corner. For those snapshots where either underdeveloped or well-developed disks (with more than 50 disk cells) are identified, the disk mass is shown below the disk cell number in the upper right corner, and the mass-to-flux ratio  $\lambda_d$ , total plasma- $\beta$ , and toroidal component  $\beta_t$  and poloidal component  $\beta_p$  of the plasma- $\beta$  are shown on the lower part of each panel.

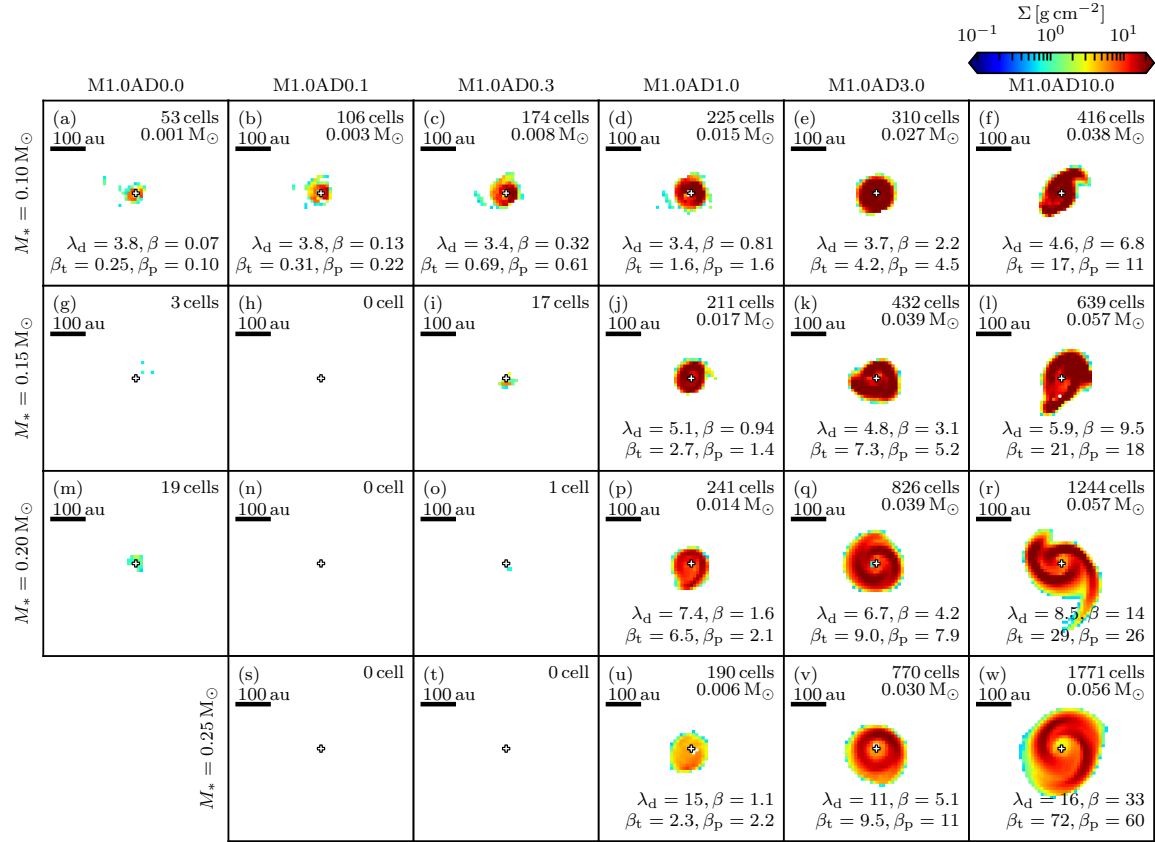


Figure 6.16: Column density of cells identified as a part of the disk along  $z$ -axis of all sonic-turbulent AD models with  $Q_A = 0.0\times, 0.1\times, 0.3\times, 1\times, 3\times, \text{ and } 10\times$  (left to right) the standard value when the sink particle has accreted 0.1, 0.15, 0.2, and 0.25  $M_\odot$  (top to bottom). The sink particle is marked by a cross. The number of cells is written on the upper right corner. For those snapshots where either underdeveloped disks or well-developed disks are identified, the disk mass is written on the upper right corner, and the mass-to-flux ratio  $\lambda_d$ , total plasma- $\beta$ , and toroidal component  $\beta_t$  and poloidal component  $\beta_p$  of  $\beta$  are written on the lower right corner of each panel.

difference is unclear. We also note that the lack of a persistent rotationally supported disk is broadly consistent with the work of Gray et al. (2018), who found that such a disk does not form unless there is a large misalignment between the turbulence-induced angular momentum (which is set to zero for our simulation as a whole) and the magnetic field. We note that Kuffmeier et al. (2017) found multiple spirals in the circumstellar regions in some of their ideal MHD disk formation simulations (see the left column of their Fig. 10) similar to our ideal MHD turbulent models (M0.5AD0.0 and M1.0AD0.0). It would be interesting to see whether their spirals are part of a warped but spatially coherent pseudo-disk (as true for our cases, e.g. Fig. 6.3) or not.

Our 3D laminar (non-turbulent) simulations with AD is a natural extension of the 2D (axisymmetric) work of Li et al. (2011). In particular, we have shown for the first time that the strongly magnetized circumstellar structure driven by AD-induced magnetic flux redistribution that is predicted analytically and found in the 2D simulations can be produced in 3D as well. We have shown further that such a structure is unstable to the magnetic interchange instability, which is broadly consistent with the 3D work of Krasnopolsky et al. (2012). However, an apparent difference is that there are AD-enabled, persistent rotationally supported circumstellar structures in our simulations (see Fig. 6.6) but not in theirs. This is probably because Krasnopolsky et al. adopted an initially uniform density distribution, which is known to be less conducive to disk formation compared to the centrally condensed distribution adopted in most of our simulations (see e.g. Machida et al. 2014). Indeed, we have performed two simulations with an initially uniform density distribution (keeping the global mass-to-flux ratio the same as before, i.e.  $\lambda_{\text{core}} \approx 2.6$ ) for the standard AD case with and without a sonic turbulence (Models M1.0AD1.0US and M0.0AD1.0US respectively). Neither model produced a large, persistent rotationally supported circumstellar structure. This is consistent with Zhao et al. (2016), who found that enhanced AD, possibly

by removal of small grains, is needed to enable the disk formation in such cases. It is also broadly consistent with Masson et al. (2016, see also Hennebelle et al. 2016), who found that, for an initially uniform core with aligned magnetic field and rotation axis, the formation of a large, well-resolved disk is enabled by AD in the relatively weak field case of  $\lambda \approx 4$  (after correcting for a somewhat different definition of the dimensionless mass-to-flux ratio) but barely in the stronger field case of  $\lambda \approx 1.6$ . They showed further that disk formation in the latter case is helped by a relatively large misalignment (of  $40^\circ$ ) between the magnetic field and rotation axis. We note that our 3D results are also qualitatively consistent with those from 2D (axisymmetric) simulations of Mellon & Li (2009) in that relatively large disks can form if the AD is strong enough. It is, however, difficult to quantitatively compare these early 2D simulations with the current 3D simulations because they have very different initial conditions (self-similar magnetized toroids with non-uniform magnetic fields versus centrally condensed cores threaded by an uniform magnetic field).

The most unique aspect of our work is the combination of turbulence and AD. We have shown that the two work together to form disks that are much better defined than those induced by turbulence or AD separately. The turbulence tends to promote disk formation at early epochs while AD helps the early disks to survive to later times. However, even with both turbulence and AD, there is no guarantee that a large, persistent disk would form automatically. It depends on many factors, including the degree of magnetization (i.e.  $\lambda_{\text{core}}$ ), the level of turbulence (i.e. Mach number  $\mathcal{M}$ ), the structure of the core (e.g. the initial density distribution), the rate of core rotation, and the degree of coupling between the magnetic field and the bulk neutral cloud material. For example, we do not find a large, persistent disk for the uniform core model M1.0AD1.0US with a sonic turbulence and the standard AD coefficient, as mentioned above.

We caution the reader that small, numerically unresolved disks may still form in those simulations that do not produce large, persistent rotationally supported disks. This is a general concern for disk formation simulations that focus on the protostellar mass accretion phase where a sink particle treatment is needed, particularly for the relatively low-resolution simulations presented in this manuscript, because the angular momentum of the material accreted onto the central star (sink particle) from the sink region is lost as far as the disk formation is concerned (e.g. Machida et al. 2014; Gray et al. 2018). We have carried out a crude resolution study, by running the uniform-grid simulations well into the protostellar accretion phase without zoom-in (256 cells in 5000 AU). Compared with the zoom-in simulations presented in this paper, it is somewhat more difficult to form disks in these lower resolution simulations, although the general trend is the same, namely, disks are formed more easily in the presence of a larger AD and a stronger turbulence. We plan to perform higher resolution simulations in the near future using a version of the **Athena++** code (currently under development) that will include not only non-ideal MHD effects and sink particles but also a self-gravity solver that works with AMR.

## 6.7 CONCLUSION

We have carried out a set of numerical simulations of disk formation in rotating, magnetized molecular cloud cores including turbulence and AD, both separately and in combination, with a focus on the protostellar mass accretion phase of star formation that is made possible by a sink particle treatment. The main results are as follows.

1. In the ideal MHD limit, a relatively strong, sonic turbulence on the core scale strongly warps but does not completely disrupt the well-known magnetically induced flattened pseudo-disk that dominates the inner protostellar accretion flow in the laminar case, in agreement with previous results obtained in the absence

of self-gravity. The turbulence facilitates the disk formation at early times, possibly by creating strong inhomogeneities (including low-density regions) in the warped pseudo-disk that allow the magnetic flux trapped near the forming star to escape more easily. The warping of the pseudo-disk may also promote disk formation by making it easier for materials with high specific angular momenta to retain their angular momenta. However, the turbulence-enabled initial disk is too strongly magnetized to persist to the end of the simulation, when the majority of the core material has been accreted onto the star or ejected in outflows. It is replaced at later times by strongly magnetized, low-density expanding regions where the magnetic flux associated with the accreted stellar material is advected outwards (i.e. the so-called “advection-DEMS” or simply DEMS).

2. We find from our 3D laminar (non-turbulent) non-ideal MHD simulations that AD can redistribute the magnetic flux associated with the accreted stellar material to a circumstellar region where it is trapped by the surrounding protostellar accretion flow, forming the so-called “diffusion-DEMS”, in agreement with previous analytic work and 2D (axisymmetric) simulations. For a relatively weak AD, the strongly magnetized diffusion-DEMS dominates the circumstellar region at early times, making disk formation difficult. It is subsequently disrupted by the magnetic interchange instabilities, although the circumstellar region remains strongly magnetized, with no evidence for a large rotationally supported disk. As the level of AD increases, the magnetic field in the circumstellar region becomes weaker and less pinched in the azimuthal direction, both of which reduce the magnetic braking torque, making it easier to form a large persistent disk.
3. We find from our non-ideal MHD simulations with sonic turbulence that the

turbulence and AD promote disk formation in a complementary manner, with the former ensuring the formation of a relatively large disk early in the protostellar accretion phase and the latter facilitating the survival of the disk to later times. In addition, the turbulence tends to make the disks formed in the presence of a relatively strong AD more stable to gravitational fragmentation.

4. The turbulence-enabled early disks tend to be strongly magnetized, which makes them difficult to persist unless a relatively strong AD is also present. Even with a strong AD, the disks formed in our simulations remain rather strongly magnetized, with a typical plasma- $\beta$  of order a few tens or smaller, which is 2–3 orders of magnitude lower than the values commonly adopted in MHD simulations of the relatively evolved, slowly accreting, protoplanetary disks. This potential tension highlights the strong need to quantify the evolution of the disk magnetic field from its parental core to the end of its evolution with increasingly realistic physics and to confront the model predictions with future ALMA Zeeman observations of the field strength in disks of different evolutionary stages.

CHAPTER 7

THE TRANSITION OF POLARIZED  
DUST THERMAL EMISSION FROM THE  
PROSTELLAR ENVELOPE TO THE  
DISK SCALE

*This chapter is adapted from Lam et al. 2021, Monthly Notices of the RAS, 507, 608, with minimal modifications, except for an extra Appendix 7.B.*

**ABSTRACT**

Polarized dust continuum emission has been observed with Atacama Large Millimeter/submillimeter Array in an increasing number of deeply embedded protostellar systems. It generally shows a sharp transition going from the protostellar envelope to the disk scale, with the polarization fraction typically dropping from  $\sim 5$  percent to  $\sim 1$  percent and the inferred magnetic field orientations becoming more aligned with the major axis of the system. We quantitatively investigate these observational trends us-

ing a sample of protostars in the Perseus molecular cloud and compare these features with a non-ideal magnetohydrodynamic disk formation simulation. We find that the gas density increases faster than the magnetic field strength in the transition from the envelope to the disk scale, which makes it more difficult to magnetically align the grains on the disk scale. Specifically, to produce the observed  $\sim 1$  percent polarization at  $\sim 100$  AU scale via grains aligned with the B-field, even relatively small grains of  $1 \mu\text{m}$  in size need to have their magnetic susceptibilities significantly enhanced (by a factor of  $\sim 20$ ) over the standard value, potentially through superparamagnetic inclusions. This requirement is more stringent for larger grains, with the enhancement factor increasing linearly with the grain size, reaching  $\sim 2 \times 10^4$  for millimeter-sized grains. Even if the required enhancement can be achieved, the resulting inferred magnetic field orientation in the simulation does not show a preference for the major axis, which is inconsistent with the observed pattern. We thus conclude that the observed trends are best described by the model where the polarization on the envelope scale is dominated by magnetically aligned grains and that on the disk scale by scattering.

## 7.1 INTRODUCTION

Magnetic fields have long been viewed as a key ingredient in molecular clouds and star formation (McKee & Ostriker 2007). This view has been greatly strengthened by polarimetric observations of dust continuum emission in recent years, especially through the *Planck* all-sky survey (e.g. Planck Collaboration et al. 2015) and Atacama Large Millimeter/submillimeter Array (ALMA; e.g. Hull & Zhang 2019). On the relatively large cloud scales probed by *Planck*, there is little doubt that the polarized dust emission traces the magnetic field because the (relatively small, sub-micron-sized) dust grains are known to be preferentially aligned with their short axis along the magnetic field (e.g. Andersson et al. 2015). On the much smaller scales

probed by ALMA, the situation is less clear, which is the focus of our investigation.

In particular, ALMA has detected dust polarization in an increasing number of protostellar systems that are still deeply embedded in their massive envelopes (e.g. Hull et al. 2017, 2020; Cox et al. 2018; Maury et al. 2018; Sadavoy et al. 2018a,b, 2019; Kwon et al. 2019; Le Gouellec et al. 2019; Takahashi et al. 2019; Ko et al. 2020; Yen et al. 2020). Le Gouellec et al. (2020) analyzed the polarization data from Class 0 sources statistically, and found an interesting anticorrelation between the dispersion of the polarization orientations and the polarization fraction. Another interesting trend, first discussed in Cox et al. (2018) and quantified further in this paper (see Section 7.2 below), is that the typical dust polarization fraction on the  $10^3$  AU scale of the inner protostellar envelope ( $\gtrsim 5$  percent) is much higher than that on the  $10^2$  AU disk scale ( $\lesssim 1$  percent). While the relatively high polarization fraction on the envelope scale is likely still due to magnetically aligned grains (as on the larger cloud scale), the origin of the much lower polarization fraction on the disk scale is less certain.

One possible explanation of the lower polarization fraction on the disk scale compared to that on the envelope scale is that the grains in the disk are much larger than those in the envelope and thus harder to align magnetically because of their longer Larmor precession timescale around the magnetic field (e.g. Lazarian 2007; Yang 2021). The higher density in the disk also makes it harder for grain alignment, regardless of the alignment mechanism because of more frequent randomizing collisions of the grains with their ambient gas. These lead to a larger ratio of the Larmor precession timescale to the gas damping timescale in the disk compared to that in the envelope, and hence a lower magnetic grain alignment efficiency in the disk (see equation 7.7 below), which may explain its lower polarization fraction.

A potential scenario is that the reduction factor of magnetic alignment on the disk scale is so large as to render the polarized emission from magnetically aligned grains

undetected. In this case, another mechanism is needed to explain the lower but still well-measured polarization at the  $\sim 1$  percent level. The most likely alternative to magnetically aligned grains is dust self-scattering, which has been shown to be capable of producing percent-level polarization at (sub)millimeter wavelengths (Kataoka et al. 2015), especially in inclined disks (Yang et al. 2016).

The goal of our investigation is therefore to quantify the change in the dust polarization fraction and pattern in the transition from the protostellar envelope scale to the disk scale and to determine whether the observed trends in the transition can be explained by magnetically aligned grains alone or whether scattering is also needed. In particular, we examine how the condition for magnetic grain alignment at a given location in the protostellar system depends on its local environment, including the gas density, magnetic field strength, and the grain properties such as size and magnetic susceptibility. We also take into consideration the possible enhancement of dust magnetic susceptibility by superparamagnetic inclusions (SPIs) based on the theory recently developed by Yang (2021). Our analytic model is then tested in synthetic polarization of a simulated protostellar disk-envelope system from Lam et al. (2019) to provide a qualitative comparison to the ALMA observations discussed in Cox et al. (2018).

The rest of the paper is organized as follows. We first revisit the ALMA polarization data of eight protostellar systems in the Perseus molecular clouds presented in Cox et al. (2018) to quantify the sharp drop in polarization fraction and change in polarization orientation from the protostellar envelope scale to the disk scale (Section 7.2). In Section 7.3, we provide an overview of the condition for magnetic alignment of dust grains based on Yang (2021). The non-ideal MHD disk formation simulations of Lam et al. (2019) are described in Section 7.4, where we also present the synthetic polarization observations and their comparison with the ALMA data. Our

results are discussed in Section 7.5. Section 7.6 summarizes our conclusions.

## 7.2 OBSERVATIONAL MOTIVATION: SHARP ENVELOPE–DISK TRANSITION IN DUST POLARIZATION

The combination of sensitivity and resolution afforded by ALMA makes it possible to detect polarized dust emission from the inner protostellar envelope down to the disk scale. The behavior of the polarization in the envelope-to-disk transition region is well illustrated in Cox et al. (2018), which presented ALMA Band 7 polarization data on 10 Class 0/I protostars in the Perseus molecular clouds (distance  $\sim 300$  pc; Zucker et al. 2019). They found that on the 100-AU disk scale the polarization tends to be well ordered, with a typical fraction of  $\lesssim 1$  percent. In contrast, on the larger envelope scale, the polarization becomes more disordered, with a relatively large fraction of typically  $\gtrsim 5$  percent. These differences were clearly visible in their polarization maps (see their Figs. 1–3) and quantified through cumulative probability distributions of the polarization fraction (see their Fig. 4).

To characterize the polarization in the envelope–disk transition further and facilitate a quantitative comparison of the observational data with synthetic observations based on numerical simulation, we re-examine the polarization data from Cox et al. (2018) from a different angle by taking into account the spatial information more directly. In particular, we want to know how the polarization fraction and direction change with the distance from the center. Since the resolution of the ALMA data presented in Cox et al. (2018) is  $\approx 0.4''$ , we regridded the data to have pixel size  $\approx 0.2''$  so that there are  $\sim 2 - 4$  pixels per beam. To correct for projection effects, we need to know the system orientation in the plane of the sky and inclination rel-

ative to the sky plane. For the orientation, we use the outflow directions inferred in Tobin et al. (2015) and Stephens et al. (2017, 2018). Since protostellar outflows are generally aligned perpendicular to the equatorial plane of the system, we adopt the orientation  $90^\circ$  to the outflow direction as the position angle of the disk of the system. For the inclination angle of the system, we use the disk orientation inferred from the VLA Ka-band continuum observations by Segura-Cox et al. (2018), as part of the VLA Nascent Disk and Multiplicity Survey of Perseus Protostars (VANDAM) survey (Tobin et al. 2016), whenever such measurement is available. For the other five systems that do not have a well-measured inclination, we assume  $45^\circ$  for the inclination angle.<sup>1</sup> Considering the targets are different in size, we further normalized the derived radius by a characteristic “disk” radius, defined as the radius of a circle that encloses the same area as the ellipse at 10 percent maximum intensity from 2D Gaussian fitting of the ALMA Band 7 Stokes I image; i.e. we fit the emission with 2D Gaussian distribution, measure the parameters of the ellipse at the 10 percent peak level of the fitted distribution, and calculate  $R_{10 \text{ percent}} \equiv \sqrt{a \cdot b}$  where  $a$ ,  $b$  are the half lengths of the major and minor axes of the resulting ellipse from the fitted Gaussian, respectively. The fitted Gaussian peak is adopted as the center of the system. The same masking criteria as in Cox et al. (2018) are used, i.e.  $I > 5\sigma_I$  and  $P > 3\sigma_P$ . More details on the de-projection process, as well as the parameters adopted for individual sources, are described in Appendix 7.A.

In Fig. 7.1, we plot, as scatter plots color-coded by polarization fraction, the combined distributions of the polarization fraction (left-hand panel) and the inferred orientation of the polarization B-vector (rotated from the E-vector by  $90^\circ$ ; right-hand panel), as a function of the normalized (deprojected) distance from the center for

---

<sup>1</sup>We have tested that the inclination angle does not have a huge effect (unless the system is nearly edge-on, which is less likely) on the features we show in Fig. 7.1, since these features are visible even before de-projection (see Appendix 7.A). We therefore adopt a representative value of  $45^\circ$ .

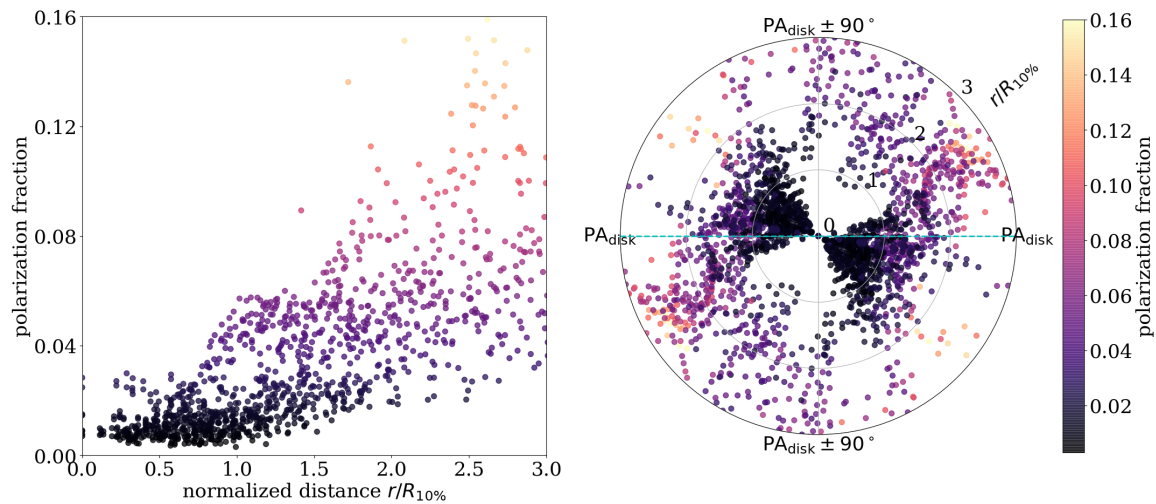


Figure 7.1: Trends of observed polarization from envelope to disk scales. Plotted as functions of the deprojected distance from the center (normalized by  $R_{10\text{ percent}}$ ; see text for definition) are the combined distributions of the polarization fraction (*left*) and the orientation of the polarization B-vector (rotated from the E-vector by  $90^\circ$ ; *right*), for 8 of the 10 protostellar systems presented in Cox et al. (2018). The orientation of the polar plot is rotated so that the disk major axes align with the horizontal line. Also, the polar plot is mirror-imaged to reflect the degeneracy of polarization angles over  $180^\circ$ . The polarization fraction is color coded in both panels to highlight its increase from the disk to envelope scale.

8 of the 10 sources discussed in Cox et al. (2018). We note that, among the 10 sources presented in Cox et al. (2018), Per 41 has too few polarization detections for meaningful analysis. The other source, Per 21, is located within the highly perturbed protostellar envelope NGC 1333 IRAS 7 that harbors at least two other protostars (see e.g. Tobin et al. 2016; Chen et al. 2019) with complex outflow morphologies (Stephens et al. 2017). The complexity makes it difficult to assign an outflow direction for Per 21 with confidence. We thus exclude it in this study as well.

The left-hand panel of Fig. 7.1 shows that there is a clear trend for the polarization fraction to stay roughly constant at typically a percent level (although it is higher in a couple of cases; see discussion in Section 4) within about one normalized radius (i.e.  $r/R_{10 \text{ percent}} \lesssim 1$ ) and then rapidly increases outwards, reaching values as high as 10 – 15 percent or more. As shown in Appendix 7.A, the trend is clear in both the cases where a large number of polarization vectors are detected on the envelope scale (such as Per 2, Per 5, Per 11, and Per 29) and those with fewer envelope-scale detections (such as Per 14, Per 18, and Per 50). It is a robust feature that needs to be explained by all models of envelope/disk polarization, including our own (see Section 7.4 below).

The right-hand panel of Fig. 7.1 shows that the orientations of the polarization B-vectors are clearly non-isotropic (e.g. two cavities devoid of data points) within about one normalized radius ( $R_{10 \text{ percent}}$ ), with a strong preference towards the disk orientation. This is in strong contrast with the orientations on the larger (envelope) scale, which are much more isotropic. The difference can also be seen in individual sources (e.g. the right-hand panels of Fig. 7.A.2), which tend to have much more uniform polarization orientations (i.e. narrow distributions) on the disk scale than on the envelope scale. Nevertheless, we note that there are noticeable offsets between the disk-scale polarization orientation and the outflow-based system major axis in some

of our targets (Per 5, Per 11, Per 18, and Per 26; see Fig. 7.A.2). It is unclear what is the physical reason introducing such offset, and we discuss this further in Sec. 7.5. In any case, the difference in the polarization orientations between the envelope and disk scales is significant, and is another feature that needs to be explained.

### 7.3 CONDITION FOR MAGNETIC GRAIN ALIGNMENT

The simplest explanation of the observed drop in polarization fraction from the envelope scale to the disk scale is that the grains are less well aligned at higher densities, especially inside the disks. Here, to explore this possibility quantitatively, we discuss the necessary conditions for magnetic grain alignment based on the recent work by Yang (2021).

The investigation of magnetic alignment of spinning dust grains has a long and distinguished history (see Andersson et al. 2015 for a review). Although there are different proposed mechanisms to spin up the dust grains, the current favorite is radiative alignment torque, which appears capable of spinning up grains in protoplanetary disks (e.g. Tazaki et al. 2017; Lazarian 2007). However, for the spinning grains to align with the magnetic field, they have to gyrate quickly around the magnetic field, with a Larmor precession timescale  $t_L$  shorter than the gas damping timescale on dust grains  $t_d$ .

#### 7.3.1 Larmor precession timescale

It is well-known that a spinning grain would be magnetized through the Barnett (1915) effect. This spinning-induced magnetization can be quantified as  $\mathbf{M} = \chi\mathbf{\Omega}/\gamma$  (Purcell 1979; Roberge et al. 1993), where  $\chi$  is the magnetic susceptibility,  $\mathbf{\Omega}$  is the angular velocity,  $\gamma = g\mu_B/\hbar$  is the gyromagnetic ratio with  $\mu_B = 9.27 \times 10^{-21}$  erg·G<sup>-1</sup> (the Bohr magneton) and  $g \approx 2$  (the  $g$ -factor) for electrons (Draine 1996). For a dust

grain with a magnetic moment  $|\mathbf{M}|V$ , where  $V$  is the volume of the dust grain (i.e.  $V \equiv 4\pi a^3/3$  for spherical grains with radius  $a$ ), the magnetic torque exerted on the dust grain by the external magnetic field  $B$  is roughly  $|\mathbf{M}|VB$ . We can therefore define a Larmor precession timescale as (see e.g. Lazarian 2007; Yang 2021):

$$\begin{aligned} t_L &= \frac{2\pi I|\boldsymbol{\Omega}|}{|\mathbf{M}|VB} = \frac{4\pi(\rho_s V)a^2/5 \cdot \gamma}{\chi VB} = \left(\frac{4\pi\gamma}{5}\right) \frac{\rho_s a^2}{\chi B} \\ &= 2.6 \times 10^{11} \text{ s} \times \hat{\chi}^{-1} \left(\frac{\rho_s}{3 \text{ g cm}^{-3}}\right) \left(\frac{T_s}{15 \text{ K}}\right) \left(\frac{B}{5 \text{ mG}}\right)^{-1} \left(\frac{a}{1 \text{ mm}}\right)^2, \end{aligned} \quad (7.1)$$

where  $\rho_s$  is the mass density of the dust grain, and

$$\hat{\chi} \equiv \chi \cdot 10^3 \left(\frac{T_s}{15 \text{ K}}\right) \quad (7.2)$$

is a dimensionless parameter of the magnetic susceptibility determined by the composition of dust grains, and  $T_s$  is the dust temperature.

For regular paramagnetic material, the magnetic susceptibility is given as (e.g. Morrish 2001; Draine 1996)

$$\chi_p = \frac{n_p \mu^2}{3kT}, \quad (7.3)$$

where  $n_p = f_p n_{\text{tot}}$  is the number density of paramagnetic atoms with  $f_p$  the fraction of the atoms that are paramagnetic and  $n_{\text{tot}}$  the total atomic density, and  $\mu = p\mu_B$  is the averaged Bohr magneton per iron atom. Draine (1996) noted that  $p \approx 5.5$  for paramagnetic materials, and gave a realistic estimate of paramagnetic susceptibility:

$$\chi_p = 4.2 \times 10^{-2} f_p \left(\frac{n_{\text{tot}}}{10^{23} \text{ cm}^{-3}}\right) \left(\frac{T_s}{15 \text{ K}}\right)^{-1} \left(\frac{p}{5.5}\right)^2. \quad (7.4)$$

For typical interstellar dust grains composed of {C, H, Mg, Si, Fe},  $\rho_s \sim 3 \text{ g cm}^{-3}$  and  $n_{\text{tot}} \sim 10^{23} \text{ cm}^{-3}$  (see e.g. Draine 1996). With  $f_p \approx 0.1$  (Draine 1996), this suggests

that the dimensionless parameter  $\hat{\chi} \sim 1$  in equation (7.1), which we will refer to as the “standard” value for paramagnetic grains.

### 7.3.2 Gas damping timescale

Collisions between dust grains and surrounding gas particles have the potential to randomize the angular momenta of grains and thus limit the degree of magnetic alignment. In general, the damping timescale can be estimated as the time needed to accumulate the same amount of mass from the gas material as the mass of the dust grain (e.g. Purcell & Spitzer 1971). Assuming every colliding gas particle sticks long enough on the grain surface for its kinetic energy to become thermalized at the grain temperature, Roberge et al. (1993) derived a gas damping timescale

$$\begin{aligned} t_d &= \frac{2\sqrt{\pi}}{5} \frac{\rho_s a}{n_g m_g v_{g,\text{th}}} \\ &= 3.37 \times 10^8 \text{ s} \times \left( \frac{\rho_s}{3 \text{ g cm}^{-3}} \right) \left( \frac{a}{1 \text{ mm}} \right) \left( \frac{n_g}{5 \times 10^9 \text{ cm}^{-3}} \right)^{-1} \left( \frac{T_g}{15 \text{ K}} \right)^{-1/2} \end{aligned} \quad (7.5)$$

for the simplest case of spherical grains<sup>2</sup>, where  $\rho_s$  and  $a$  are the mass density and size of the grain,  $n_g$  the number density of the gas,  $m_g$  the mass per gas particle, and  $v_{g,\text{th}}$  and  $T_g$  the gas thermal velocity and temperature, respectively.

### 7.3.3 Condition for magnetic alignment with superparamagnetic Inclusions

Combining equations (7.1) and (7.5) and assuming that the dust grains and gas particles are in thermal equilibrium ( $T_s = T_g \equiv T$ ), we have

$$\frac{t_L}{t_d} = 771 \times \left( \frac{a_{\text{mm}}}{\hat{\chi}} \right) \left( \frac{B}{5 \text{ mG}} \right)^{-1} \left( \frac{n_g}{5 \times 10^9 \text{ cm}^{-3}} \right) \left( \frac{T}{15 \text{ K}} \right)^{3/2} \quad (7.6)$$

---

<sup>2</sup>Note that for polarization produced by B-field aligned grains, non-spherical grains are required. Nonetheless, the timescale would be at the same order of magnitude.

where  $a_{\text{mm}} \equiv (a/1 \text{ mm})$  is the grain size in units of millimeter. Note that, as discussed in Yang (2021), the magnetic susceptibility parameter  $\hat{\chi}$  and the grain size  $a$  are degenerate in the ratio between Larmor precession and gas damping. Equation (7.6) suggests that, for paramagnetic materials with the standard value of magnetic susceptibility  $\hat{\chi} \sim 1$ , only small, sub-micron-sized grains have  $t_L < t_d$  (and thus can align with the magnetic field) for the adopted fiducial disk parameters of  $B \sim 5 \text{ mG}$ ,  $n_g \sim 5 \times 10^9 \text{ cm}^{-3}$ , and  $T \sim 15 \text{ K}$ . However,  $\hat{\chi}$  can be enhanced by a large factor when superparamagnetic inclusions (SPIs hereafter) are present in the grains (Jones & Spitzer 1967).

Superparamagnetism appears in nanoparticles made of ferromagnetic or ferrimagnetic materials. Unlike paramagnetic materials that have only un-correlated electron spins, within one superparamagnetic particle, all the atoms are spontaneously magnetized and behave like a single large magnetic moment (“macro-spin”; Bean & Livingston 1959), which could greatly increase the magnetic susceptibility. Yang (2021) considered three types of candidate materials for the superparamagnetic inclusions, and estimated a maximum enhancement factor of  $\hat{\chi}_{\text{max}} \sim 1.1 \times 10^3$  for  $\text{Fe}_3\text{O}_4$  (magnetite),  $\sim 3.7 \times 10^3$  for  $\gamma\text{-Fe}_2\text{O}_3$  (maghemite), and  $\sim 7.0 \times 10^4$  for the extreme case of pure metallic iron (see their Table 1). Since magnetite and maghemite are more likely representative of superparamagnetic materials than metallic iron, the magnetic susceptibility is likely enhanced by a maximum factor up to a few thousands at most, rather than tens of thousands. Yang (2021) also noted that this maximum enhancement is a hard limit determined by the crystalline structure of the SPI material and the energy needed to overcome the crystalline structure and align the initially randomly oriented magnetic moments inside the SPIs to the direction of the external magnetic field. The required energy is proportional to the volume of the SPI. It therefore takes longer to align larger SPIs because of a larger energy required. Indeed, the

alignment timescale is exponentially sensitive to the SPI size (see equation 9 of Yang (2021)), which severely limits the contributions of SPIs larger than the critical size to the magnetic susceptibility of the dust grain. Indeed, the maximum enhancement is reached only when all SPIs inside a grain have the (same) critical size, which is unlikely.

As briefly discussed in Yang (2021), while no magnetic alignment is expected when the Larmor precession timescale is longer than the gas damping time scale ( $t_L > t_d$ ),  $t_L < t_d$  does not guarantee magnetic alignment. The grain needs to gyrate around the magnetic field multiple times within a single gas damping time in order to ensure magnetic alignment, which leads to a more stringent alignment condition:  $t_L < t_d/\eta$ , where  $\eta (> 1)$  is the number of gyrations per gas damping time needed for grain alignment. The exact value of  $\eta$  is uncertain; in the discussion below, we will follow Yang (2021) and adopt a fiducial value of 10. Making use of equation (7.6), the alignment condition becomes:

$$\lambda \equiv 771 \times \left( \frac{B}{5 \text{ mG}} \right)^{-1} \left( \frac{n_g}{5 \times 10^9 \text{ cm}^{-3}} \right) \left( \frac{T}{15 \text{ K}} \right)^{3/2} < \xi \equiv \frac{\hat{\chi}/\eta}{a_{\text{mm}}}, \quad (7.7)$$

where the dimensionless parameter  $\lambda$  and  $\xi$  encapsulate, respectively, the combination of the gas and magnetic field quantities and of the grain properties that enter the alignment condition. They will be referred to as gas and grain alignment parameter respectively hereafter. In regions where the gas alignment parameter  $\lambda$  is larger, the grains are harder to magnetically align because of a higher gas density  $n_g$ , a higher temperature  $T$ , or a lower magnetic field strength  $B$ . Conversely, grains with a larger grain alignment parameter  $\xi$  are easier to align magnetically because of a larger magnetic susceptibility enhancement  $\hat{\chi}$  by SPIs, a smaller grain size  $a$ , or a less stringent requirement on the number of times  $\eta$  that the spinning grains need

to gyrate around the field line before being knocked off by gas collisions in order to be magnetically aligned. In particular, in the protostellar envelope where the gas density  $n_g$  is lower and the grain size  $a$  is expected to be smaller, the condition for magnetic alignment should be satisfied more easily. In the next section, we will quantify how the condition affects the polarization in the transition region from the protostellar envelope scale to the disk scale, using the physical quantities obtained from a non-ideal MHD disk formation simulation.

## 7.4 MODELING DUST POLARIZATION

### 7.4.1 Model setup and synthetic observations

The simulation to be used for our polarization modeling comes from Lam et al. (2019), which contains a series of non-ideal MHD simulations of turbulent core collapse and disk formation with a range of values for the turbulent level and ambipolar diffusion (see their Table 1). The simulations are isothermal with a temperature of 10 K. They start with a centrally condensed core of  $0.5 M_\odot$  in mass and 2000 AU in radius and an initial solid-body rotation of  $\Omega = 6 \times 10^{-13} \text{ s}^{-1}$ . For the purpose of illustrating the difference in dust polarization between the protostellar envelope and disk, we pick a high-resolution version of their model M1.0AD10.0, which has an initial turbulence Mach number of 1.0, a relatively large ambipolar diffusion coefficient that is ten times the fiducial value based on the standard cosmic ray ionization rate of  $10^{-17} \text{ s}^{-1}$  (see e.g. Shu 1992), and a  $\sim 100$  AU disk. The simulation was performed using the **Athena** code (Stone et al. 2008) on a uniform base grid of  $512^3$ . It was zoomed in once with half box length while keeping the number of cells fixed at  $512^3$ , which yields a minimum resolution of 5 AU. The high-resolution simulation data at the time when the disk is well formed around the central protostar of  $0.22 M_\odot$  is used

for our polarization analysis. The disk can be clearly see in the top panel of Fig. 7.2, which shows a 3D view of the density distribution, together with several representative magnetic field lines. The bottom panel shows the polarization vectors obtained through the procedure discussed next.

In the simplest case of optically thin dust with a spatially homogeneous grain alignment efficiency, the Stokes parameters  $I$ ,  $Q$ , and  $U$  of dust thermal emission along a given line of sight are given by (see e.g. Fiege & Pudritz 2000):

$$I = \int \rho \left( 1 - \alpha \left( \frac{\cos^2 \gamma}{2} - \frac{1}{3} \right) \right) ds, \quad (7.8a)$$

$$Q = \alpha \int \rho \cos 2\psi \cos^2 \gamma ds, \quad (7.8b)$$

$$U = \alpha \int \rho \sin 2\psi \cos^2 \gamma ds, \quad (7.8c)$$

where  $\rho$  and  $s$  are, respectively, the mass density at a given location and the distance into the cloud of that location along the line of sight. The polarizability parameter  $\alpha$  is determined by the grain cross sections and alignment properties and assumed to be spatially constant. The quantity  $\gamma$  is the inclination angle of the field line with respect to the plane of the sky, and  $\psi$  is the angle of the magnetic field from the direction of positive  $Q$  in the sky plane. The maximum degree of polarization  $p_0$  is related to the parameter  $\alpha$  through  $p_0 = \alpha/(1 - \alpha/6)$ . For simplicity, we set  $\alpha = 10$  percent, which yields  $p_0 = 10.17$  percent<sup>3</sup>. The polarization fraction and direction

---

<sup>3</sup>The maximum polarization parameter  $p_0$  should in principle be determined from grain alignment theory, as done in, e.g. Valdivia et al. (2019); Kuffmeier et al. (2020), using the POLARIS code (Reissl et al. 2016). However, the uncertainties in the grain properties, especially their shapes, make it difficult to firmly predict this parameter. Our choice is guided by the typical values observed in the inner protostellar envelopes of the Perseus protostars. It is the same as the constant value adopted by Valdivia et al. (2019) but somewhat smaller than the value of 15 percent adopted by Padovani et al. (2012) and Lee et al. (2017).

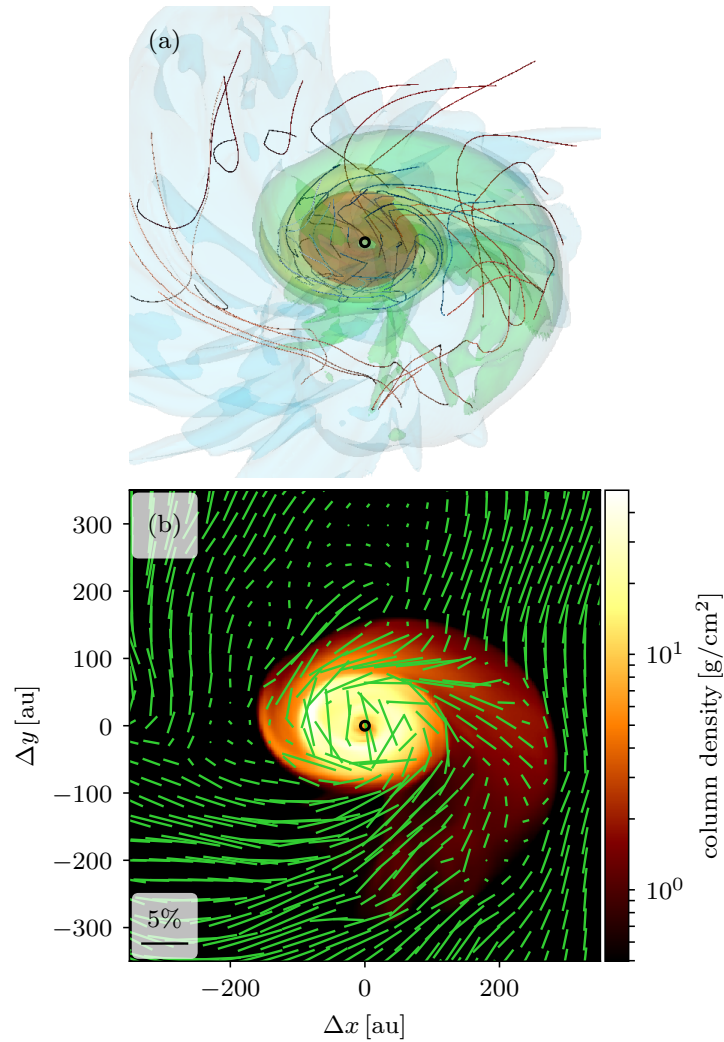


Figure 7.2: (a) A 3D view of the density distribution and magnetic field lines of the simulated protostellar envelope–disk system that is used for the dust polarization modeling. Plotted are the iso-density surfaces at  $n_g = 10^7, 10^8, 10^9, 10^{10} \text{ cm}^{-3}$  (semi-transparent surfaces) and a sample of magnetic field lines, viewed at an angle of  $45^\circ$  to the rotation axis (as in the synthetic polarization maps in the bottom panel and in Fig. 7.3 below). (b) Polarization (B-)vectors (with length proportional to the polarization fraction) superposed on the color map of (mass) column density.

are obtained from the Stokes parameters through

$$p = \frac{\sqrt{Q^2 + U^2}}{I}, \quad \phi = \frac{1}{2} \arctan 2(U, Q). \quad (7.9)$$

There are a few complications. First, the densest part of the protostellar disk formed in our simulation is moderately optically thick, which could lower its polarization fraction somewhat (Yang et al. 2017; Lin et al. 2020). The optical depth (and associated extinction) is accounted for by solving the vector radiation transfer equation, as described in Appendix 7.C. Secondly, the magnetic alignment efficiency is not expected to be spatially homogeneous, with grains in denser regions less likely magnetically aligned, as discussed in Section 7.3. We capture this effect using a magnetic alignment probability  $A$ , defined in each voxel of the simulation based on the alignment condition, equation (7.7):

$$A = \begin{cases} 1, & \text{if the voxel satisfies equation (7.7)} \\ 0, & \text{if the voxel does not satisfy equation (7.7)}. \end{cases} \quad (7.10)$$

Finally, it is well known that dust scattering can provide significant polarization in inclined disks along the disk minor axis (Kataoka et al. 2015; Yang et al. 2016). To account for this possibility, in one of the models, we added a scattering-induced polarization of fraction  $p_{\text{sca}}$  (see Section 7.4.2 below for discussions on the value of  $p_{\text{sca}}$ ) along the disk minor axis (which is the negative  $Q$  direction in our setup) only in those voxels that do not satisfy the magnetic alignment condition (i.e.  $A = 0$ ).

The synthetic observations are conducted at a resolution of 5 AU. To provide better comparison to the ALMA observations of Cox et al. (2018), we smoothed the synthetic  $I$ ,  $Q$ , and  $U$  maps with a 2D Gaussian beam with FWHM = 10 pixels

Table 7.1: Model parameters and outcome.

Model Name	$\xi$	$p_{sca}$	Consistency <sup>a</sup>
Xi-inf-NoSca	$\infty$	0.0	no
Xi-100-NoSca	100	0.0	no
Xi-2000-NoSca	2000	0.0	partially
Xi-100-Sca	100	1 percent	yes

<sup>a</sup> Whether or not the model is broadly consistent with the observed polarization trends from the envelope to disk scale discussed in Section 7.2.

(corresponding to  $\sim 50$  AU), which is large enough to illustrate the beam convolution effect but small enough that the envelope and disk scales remain distinct (see Fig. 7.3 below). To be consistent with our analysis on the observational data, we downsampled the smoothed synthetic observations to have  $\approx 4$  pixels per beam. We did not include any noise in the synthetic observations but applied the same masking criteria ( $I > 5\sigma_I$ ,  $P > 3\sigma_P$ , where  $P = \sqrt{Q^2 + U^2}$  is the polarized intensity and  $\sigma_I$ ,  $\sigma_P$  are mean values measured from a relatively quiescent  $10 \times 10$  pixel<sup>2</sup> region on our synthetic maps) as adopted in Cox et al. (2018) for consistency and better comparison with data.

### 7.4.2 Model results

We consider four models that cover a range of parameters, with the simulated system viewed along a representative line of sight that is  $45^\circ$  to the disk plane (i.e. an inclination angle  $i = 45^\circ$ ). The model names and parameters are listed in Table 7.1. We follow the same deprojection process as described in Section 7.2 and Appendix 7.A with the known projected disk orientation (horizontal) and inclination angle ( $45^\circ$ ). Similar to Fig. 7.1, we plot the polarization fraction and angle as functions of the normalized, inclination-corrected radius for each synthetic observation in Fig. 7.3.

We start the discussion with the simplest case of spatially homogeneous magnetic

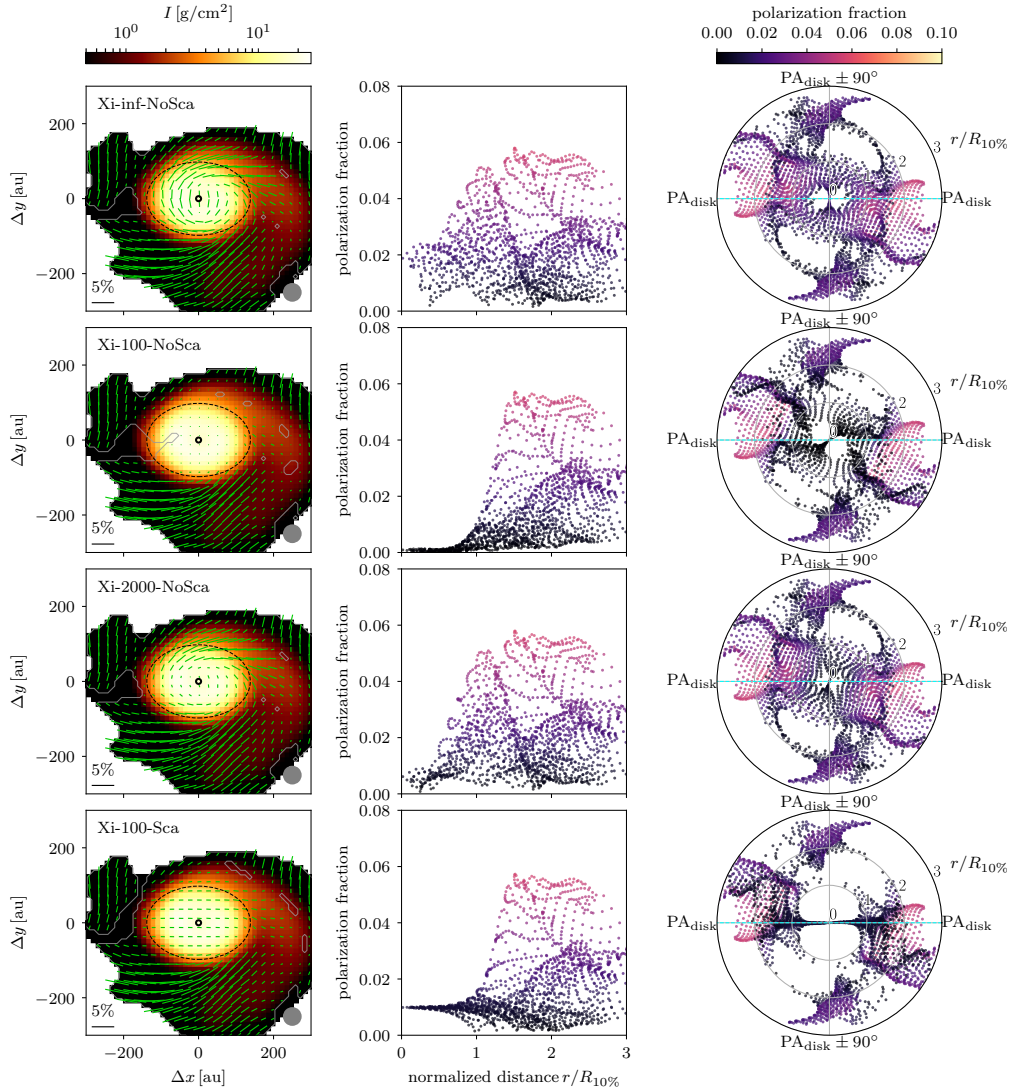


Figure 7.3: Comparing the four models of synthetic polarization considered in this study. Top to bottom: Model Xi-inf-NoSca, Xi-100-NoSca, Xi-2000-NoSca, and Xi-100-Sca (see Table 7.1 for model parameters). *Left-hand panels*: Maps of total intensity (with mask  $I > 5\sigma_I$ ), overplotted with polarization (B-)vectors (*green segments*), with length proportional to the polarization fraction. Gray contours show the masking boundaries  $P = 3\sigma_P$  adopted when calculating the scatter plots (*middle and right-hand panels*). Black open circles mark the locations of the protostar, and black dashed ellipses represent the disk defined by horizontal position angle and  $45^\circ$  inclination, with size comparable to the contour of 10 percent peak intensity). *Middle and right-hand panels*: scatter plots of polarization fraction (*middle*) and angle (*right*) in the corresponding envelope–disk system, as in Fig. 7.1. The polarization fraction is color coded in both panels.

grain alignment without scattering (Model Xi-inf-NoSca, the first row of Fig. 7.3). In this case, the alignment condition is satisfied everywhere, including in the densest part of the disk. To facilitate comparison with observations, we masked out regions with polarized intensity  $P < 3\sigma_P$ , which creates several spatially coherent patches of high polarization separated by stripes of lower polarization. Since the dust is aligned with the magnetic field everywhere, the relatively-low polarization stripes are caused by a combination of field orientation along the line of sight and, more importantly, the variation of the field component in the sky plane, which leads to a cancellation of the polarized emission (e.g. Kataoka et al. 2012). A clear example of the lower polarization stripes is located to the upper-left of the disk (see the upper-left panel of Fig. 7.3 and, more clearly, Fig. 7.2(b), where the polarization map is not beam-convolved). The low polarization in this region comes from its magnetic field lines being pinching by the radial infall and twisted by rotation at the same time, which results in roughly orthogonal magnetic fields at different locations along the same line of sight (see Fig. 7.2a for a visual impression).

It is obvious that the simplest model fails to reproduce the observed trends in two ways. First, although the polarization fraction on the envelope scale is broadly consistent with the observed values, that on the disk scale is higher than typically observed. This is not too surprising since the magnetic field in the densest part of the disk that dominates the dust emission is rather well ordered (and not along the line of sight; see the representative field lines threading the disk in Fig. 7.2a for an illustration), which leads to relatively little cancellation of polarized emission. Indeed, the polarization fraction would be even higher without the beam-convolution, as can be seen from Fig. 7.2(a), which shows that the intrinsic polarization fraction (before beam convolution) on the disk scale is comparable to that on the envelope scale. Clearly, magnetic field geometry alone cannot explain the large reduction of

the polarization fraction on the disk scale compared to the envelope scale. Secondly, there is substantial variation of the polarization orientations on the disk scale except in the very central region ( $r \lesssim 0.4R_{10 \text{ percent}}$ ), where the polarization is aligned perpendicular to the disk major axis. The reason for this polarization orientation is that the magnetic field threading the disk has a significant poloidal component (as opposed to being wound up by disk rotation into a completely toroidal configuration, presumably because of the relatively large magnetic diffusivity that enabled the disk to form and survive in the simulation in the first place). We should note that the beam convolution makes the orientations of the polarization vectors in the inner part of the disk more ordered but this effect is relatively moderate (compare Fig. 7.2(b) and the top-left panel of Fig. 7.3). In particular, it does not make the polarization (B-)vectors preferentially align with the system major axis, which is one of the observed trends for the disk-scale polarization (see the right-hand panel of Fig. 7.1).

We next consider Model Xi-100-NoSca with the grain alignment parameter  $\xi$  on the right side of the equation (7.7) set to 100 instead of  $\infty$ . The results are shown in the second row of Fig. 7.3. Note that the combination of physical parameters to reach  $\xi \equiv \hat{\chi}/(\eta a_{\text{mm}}) = 100$  is not unique. For the fiducial choice of  $\eta = 10$ , the value corresponds to micron-sized ( $a_{\text{mm}} = 0.001$ ), regular paramagnetic grains without any superparamagnetic inclusions ( $\hat{\chi} = 1$ ). Another combination is to have much larger, mm-sized grains ( $a_{\text{mm}} = 1$ ) with the magnetic susceptibility enhanced by a factor of 1000 ( $\hat{\chi} = 10^3$ ) by SPI. Compared with the simplest model with a spatially homogeneous grain alignment (Model Xi-inf-NoSca, first row), the polarization on the envelope scale appears little affected, indicating that the grains there remain efficiently aligned with the magnetic field. In contrast, the polarization on the disk scale is drastically reduced, to a level well below 1 percent.

The reason for the reduction can be understood from Fig. 7.4, where we show a

face-on view (along the  $z$ -axis) of the spatial distributions (in the  $x - y$  plane) of the gas number density  $n_g$ , the magnetic field strength  $B$ , and the corresponding dimensionless gas alignment parameter  $\lambda$  defined in equation (7.7). Along each  $z$ -sight line, these quantities are plotted at the location where the density is the highest, which is chosen to highlight the disk. It is clear that, while both the magnetic field strength and the density increase from the envelope to the disk, the density increases by a much larger factor, making it easier for the collisions with gas particles to damp out the Larmor precession of the spinning grains around the magnetic field in the disk than in the envelope. This drastic difference between how the density and field strength vary from the envelope to the disk scale is quantified in panel (d), where we plot the average and range of these two quantities at each radius. The difference is reflected in the distribution of the gas alignment parameter  $\lambda \propto n_g/B$ , which is plotted in panel (e). Clearly,  $\lambda$  increases rapidly as the radius decreases, crossing the value of 100 adopted for the grain alignment parameter  $\xi$  for Model Xi-100-NoSca (the lower dashed line in the panel) around a radius of order 200 AU. In the envelope outside this radius, the grain alignment condition  $\lambda < \xi$  (equation 7.7) is satisfied, which leads to a high polarization fraction. Interior to this radius, the alignment condition is violated for most of the mass, which leads to a polarization fraction well below the observed value. An implication of this deficiency is that the observed disk-scale polarization is unlikely produced by large, mm-sized, magnetically aligned grains since it would require an unrealistically large enhancement of the magnetic susceptibility (by a factor more than  $10^3$ ).

To increase the polarization level on the disk scale, we consider a larger grain alignment parameter,  $\xi = 2000$  (Model Xi-2000-NoSca, third row of Fig. 7.3). For the fiducial value of  $\eta = 10$ , this choice corresponds to  $\hat{\chi} = 20000 a_{\text{mm}}$ , which means that, for large mm-sized grains, the magnetic susceptibility must be enhanced by a

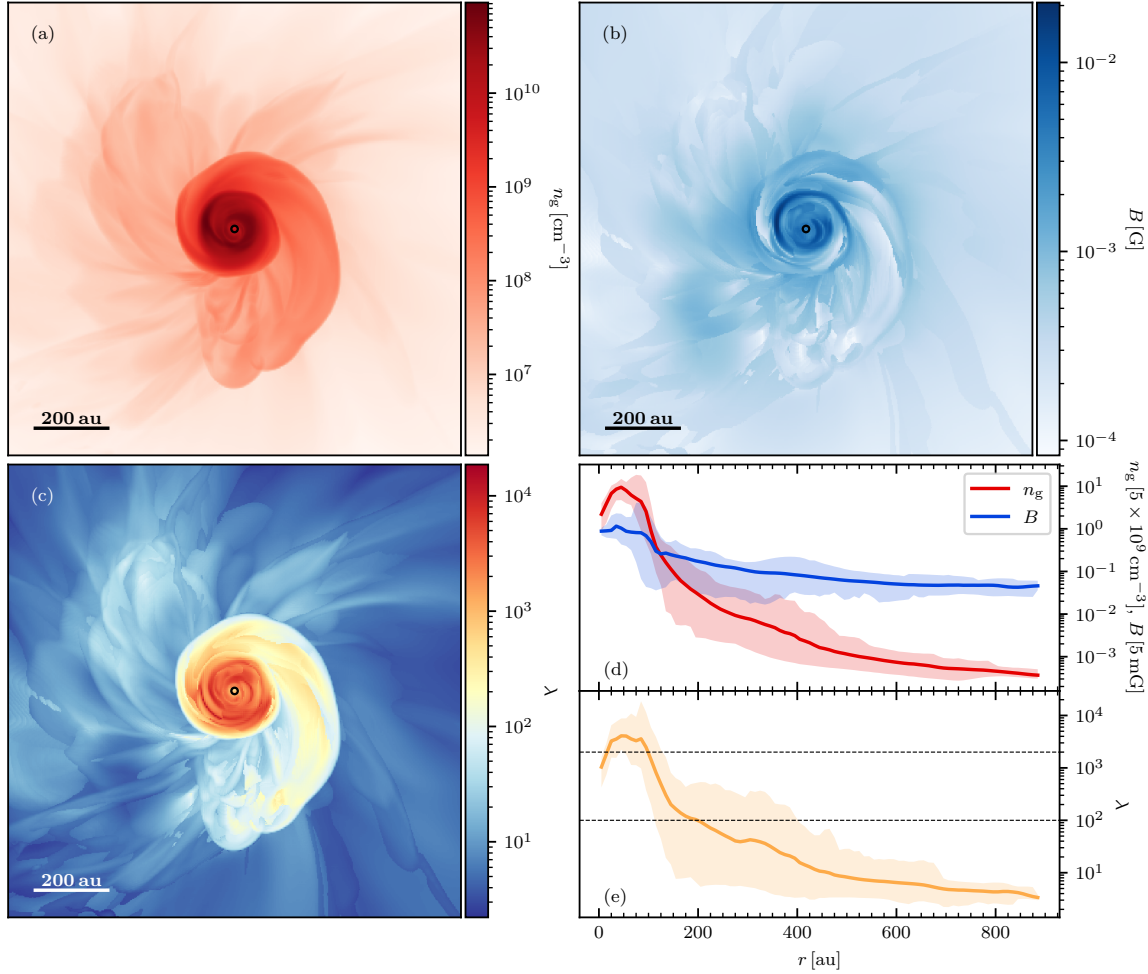


Figure 7.4: Face-on view of the spatial distributions (in the  $x - y$  plane) of (a) volume density, (b) the magnetic field strength, and (c) the dimensionless gas alignment parameter  $\lambda$  (see equation 7.7), at the location along each  $z$ -sight line where the density is the highest. The small black circle highlights the location of the sink (stellar) particle in the simulation. Also plotted are the azimuthal average and range of the density and field strength (panel d) and gas alignment parameter  $\lambda$  (panel e) as a function of radius. Note that  $\lambda$  is larger in the disk than in the envelope, indicating that the condition for magnetic alignment is harder to satisfy in the former than in the latter. The grain alignment parameter adopted in Models Xi-100-NoSca and Xi-100-Sca ( $\xi = 100$ ) is shown as the lower dashed horizontal line in panel (e), and that in Model Xi-2000-NoSca ( $\xi = 2000$ ) as the upper dashed line.

factor close the maximum possible value for the extreme case of pure metallic iron as the material for superparamagnetic inclusions (Yang 2021); the requirement would be even more extreme when the higher temperature on the disk scale is taken into account. For smaller grains, the requirement is less extreme. For example, for  $1 \mu\text{m}$ -sized grains, the enhancement factor is 20. In any case, with the grain alignment parameter  $\xi$  increased from 100 to 2000, we are able to increase the polarization fraction on the disk scale from  $\ll 1$  percent to  $\sim 1$  percent, more in line with the typically observed values. At the same time, this polarization fraction is smaller than that of Model Xi-inf-NoSca, where the magnetically aligned grains in the disk produce a polarization fraction significantly above the typically observed values.

Even though Model Xi-2000-NoSca has enough magnetic alignment of the grains to produce a polarization fraction in line with the typically observed values on the disk scale, its polarization orientations differ substantially from the observed trend. In particular, there is a significant variation in polarization orientation on the disk scale, with a preference along the disk minor axis, which is the opposite of the observed trend. This discrepancy motivates us to consider a model that includes another polarization mechanism – dust scattering.

The degree of continuum polarization produced by dust scattering depends sensitively on the grain size. At the wavelength of ALMA Band 7, the optimal size is of order  $10^2 \mu\text{m}$  (Kataoka et al. 2015). Such grains would typically produce a percent-level polarization with E-vectors along the minor axis of the inclined disk (e.g. Kataoka et al. 2016; Yang et al. 2016). To capture this effect, we add in Model Xi-100-Sca a scattering-induced polarization to Model Xi-100-NoSca according to the prescription given in equation (7.15), with  $p_{\text{sca}} = 0.01$ . The result is displayed in the last row of Fig. 7.3.

As expected, the polarization structure of Model Xi-100-Sca is very similar to that

of Model Xi-100-NoSca on the envelope scale, where the grains remain mostly aligned to the magnetic field in both cases (comparing the second and fourth row of Fig. 7.3). The main difference comes from the disk scale, where the scattering in the former has now produced a percent-level polarization with the B-vectors preferentially along the major axis of the disk, as suggested by the ALMA observations in Cox et al. (2018). This hybrid model, with polarization on the envelope scale dominated by magnetically aligned grains and that on the disk scale by scattering, is thus the best of the four representative models considered in this paper for interpreting the observational results.

## 7.5 DISCUSSION

We would like to point out that since the simulations in Lam et al. (2019) are isothermal, the temperature dependence in the gas alignment parameter  $\lambda$  (see equation 7.7) is neglected in our analysis in Section 7.4.2. However, we note that the increase in  $\lambda$  from the envelope to the disk scale is expected to be even faster when the temperature gradient is taken into account under the following considerations. Generally speaking, the temperature and thermal velocity (proportional to  $\sqrt{T}$ ) are expected to be higher at small radii. Assuming hydrostatic equilibrium, the thickness of the disk is proportional to the thermal velocity, and the gas density is inversely proportional to the disk height. This decrease in density as a result of the thicker disk cancels out the dependence of collision frequency (or the gas damping timescale; see equation 7.5) on the increasing temperature, resulting in a similar gas damping timescale. However, the higher temperature also reduces the magnetic susceptibility and increases the Larmor precession timescale (see equation 7.1), making magnetic alignment more difficult for dust grains in the disk. Therefore, including a temperature dependence in our analysis in Section 7.4.2 would not enhance magnetic

alignment on the disk scale, and thus our qualitative conclusion would be strengthened.

Though we present the observational data from eight sources as a combined plot in Fig. 7.1, it is important to consider the differences among individual sources. In particular, we note that some of the protostellar systems have higher disk-scale polarization level than the others. This can be seen in the left-hand panel of Fig. 7.1: While the majority of the cells at  $r/R_{10 \text{ percent}} \lesssim 0.5$  have polarization fraction  $\approx 0.01$ , there are systems showing  $p \approx 0.02 - 0.03$  at the inner-most region of the disk (also see Fig. 7.A.2). The detailed analysis of individual protostellar systems is beyond the scope of this paper, but we would like to note the possibility that though dust scattering works well for the general trend of the disk-scale polarization, magnetically aligned grains may still dominate the polarization observed in some protostellar systems if the grains have relatively small sizes and/or their magnetic susceptibility is greatly enhanced by SPIs.

We also note that, while the preference of the B-vectors to align with the major axis of the disk is clear in the ALMA data, they could be offset by up to  $\sim 45^\circ$  (see Section 7.2; also see Fig. 7.A.2). Since we derived the direction of the disk major axis from the outflow orientation, which has a relatively low uncertainty (typically  $\lesssim 10^\circ$ ; see e.g. Stephens et al. 2018), this offset is likely real if the outflow is launched perpendicular to the disk, as generally expected. It is possible that in the systems with large polarization-disk orientation offsets (Per 5, Per 11, Per 18, and Per 26; see Fig. 7.A.2), the scattering-induced polarization on the disk scale is contaminated by that from magnetically aligned grains, whose orientation can deviate significantly from the disk major axis (see, e.g. the top panel of Fig. 7.3). Higher resolution observations are needed to test this possibility.

## 7.6 SUMMARY

We have re-analyzed the ALMA Band 7 polarization data from Cox et al. (2018) for deeply embedded protostars in the Perseus molecular cloud on the scales of inner protostellar envelopes and disks. A simple dust polarization model was constructed based on recent theoretical work by Yang (2021) and the non-ideal MHD disk formation simulations of Lam et al. (2019) to explain the observational trends. Our main results are summarized as follows:

1. Using scatter plots, we quantified the observational trends first identified in Cox et al. (2018) that the polarization fraction stays relatively constant at a typical level of  $\sim 1$  percent on the disk scale ( $r \lesssim R_{10 \text{ percent}}$ ) and increases sharply going from the disk to the envelope scale (see the left-hand panel of Fig. 7.1). In addition, the polarization (B-)vectors tend to orient more perpendicular than parallel to outflow axis (right-hand panel of Fig. 7.1), indicating a preferential alignment with the disk major axis, under the assumption that all polarization is from magnetically aligned grains. These quantitative behaviors provide guidance to theoretical models of dust polarization in the earliest phases of low-mass star formation.

2. Using MHD simulations of disk formation enabled by a combination of ambipolar diffusion and turbulence (Lam et al. 2019), we showed that the observed sharp reduction of polarization fraction from the envelope to disk scale cannot be explained by the magnetic field geometry alone. The magnetic field on the disk scale is rather well ordered (see Fig. 7.2) and produces an intrinsic polarization fraction comparable to that in the envelope. Beam averaging can significantly reduce the polarization fraction on the disk scale, making it more consistent with the typically observed values. It cannot, however, make the orientations of the polarization (B-)vectors preferentially align with the system major axis (see Fig. 7.3, first row), which is one of the observed

trends.

3. Our MHD simulations show that the magnetic field strength increases from the envelope to the disk scale (Figs. 7.4a and d), which tends to increase the ability of the magnetic field to align the spinning grains. However, this tendency is overwhelmed by the much faster increase in density (Figs. 7.4b and d), making grain alignment more difficult through more frequent gas collisions. We show that large, mm-sized grains cannot be aligned by the magnetic field on the disk scale to produce the typically observed polarization level of  $\sim 1$  percent even if their magnetic susceptibility is enhanced by an uncomfortably large factor of  $10^3$  (see the second row of Fig. 7.3). In order for such large grains to be aligned well enough to account for the percent level polarization, the enhancement factor must reach a factor of  $\sim 2 \times 10^4$  (see the third row of Fig. 7.3), which is unlikely since it is close to the maximum factor estimated for the extreme case of metallic iron as the material for superparamagnetic inclusions. For smaller grains, the required enhancement factor is less extreme. For example, for  $1 \mu\text{m}$  grains, it is a factor of 20, which is still quite significant; it is unclear whether such an enhancement can be naturally achieved or not. Even if the required enhancement can be achieved, the resulting polarization (B-vector) orientation does not show a preference for the major axis on the disk scale, which is inconsistent with the observed trend.

4. The model most consistent with the observed trends is the one where the polarization on the envelope scale is dominated by magnetically aligned grains (with a relatively large maximum polarization fraction of order 10 percent) and by scattering on the disk scale. The former is consistent with the expectation that the grains in the low-density envelope remain relatively small and thus more easily aligned magnetically because of fast Larmor precession and long gas damping timescale. The latter requires grains of order 0.1 mm in order to efficiently produce polarization at (sub)millimeter

wavelengths through scattering.

# APPENDIX

## 7.A DEPROJECTED POLARIZATION RESULTS FOR INDIVIDUAL SOURCES

In this appendix, we describe the procedure for deprojecting the dust continuum map to obtain the distributions of the polarization fraction and orientation as a function of the radius for 8 of the 10 protostellar systems reported in Cox et al. (2018). As discussed in Section 7.2, we define a disk plane for each source based on its outflow direction inferred from the MASSES survey (Stephens et al. 2017, 2018)). The inclination angle of a system to the plane of the sky could be more uncertain unless a well-defined dust disk is observed and fitted. This is the case for three of our eight targets using the analysis from the VANDAM (Segura-Cox et al. 2018). We thus use the protostellar disk-fitted inclination angles for these three systems (Per-emb-11, Per-emb-14, Per-emb-50). For the remaining protostellar systems without well-established disks, we adopt a single value of  $45^\circ$ ; the exact value adopted for the inclination angle does not change our conclusions qualitatively.

To compare the polarization data from disks with different sizes, we normalize the distance from the center by a characteristic radius  $R_{10 \text{ percent}}$ . As described in

Section 7.2, it is the radius of a circle that encloses the same area as the ellipse at 10 percent maximum intensity from 2D Gaussian fitting of the ALMA Band 7 Stokes I image. It is not our intention to claim that  $R_{10 \text{ percent}}$  represents the actual disk radius, although the transition from disk-scale to envelope-scale polarization patterns does seem to happen between  $\sim 1$  and  $2 R_{10 \text{ percent}}$  for all protostellar systems investigated in this study (see e.g. Fig. 7.1).

The effects of the deprojection and radius normalization are illustrated in Fig. 7.A.1 for Per-emb-14. The middle column shows the polarization fraction as a function of distance to the center of the system (defined as the location of the peak intensity), both before (top) and after (middle) the deprojection, and after the normalization with  $R_{10 \text{ percent}}$  (bottom). The normalization suggests that the transition from flat (disk-scale) to steep (envelope-scale)  $p - r$  correlation happens roughly at  $R_{10 \text{ percent}}$  (vertical dotted line in the middle panel). The right column of Fig. 7.A.1 shows the corresponding polar plot of the polarization orientations. Note that our deprojection routine only provides a correction on the distance to the system center and does not modify the orientation of the polarization segments; this is the reason why the distributions of polarization orientations in the polar plots (the right-hand panels of Fig. 7.A.1) are barely impacted by the deprojection process.

Fig. 7.A.2 summarizes the deprojection results for the eight ALMA targets considered in this study except for Per-emb-14, which is presented in Fig. 7.A.1. The deprojection parameters (position angle, inclination angle, normalized radius  $R_{10 \text{ percent}}$ ) for individual systems are listed in Table 7.A.1. The disk-to-envelope transition of the  $p - r$  correlation at the distance  $\sim 1 - 2R_{10 \text{ percent}}$  is clear in all systems. We would like to point out that such transition is not an artificial result of our deprojection routine; in fact, it could also be seen even before deprojection (see e.g. Fig. 7.A.1), and the deprojection simply highlights this transition.

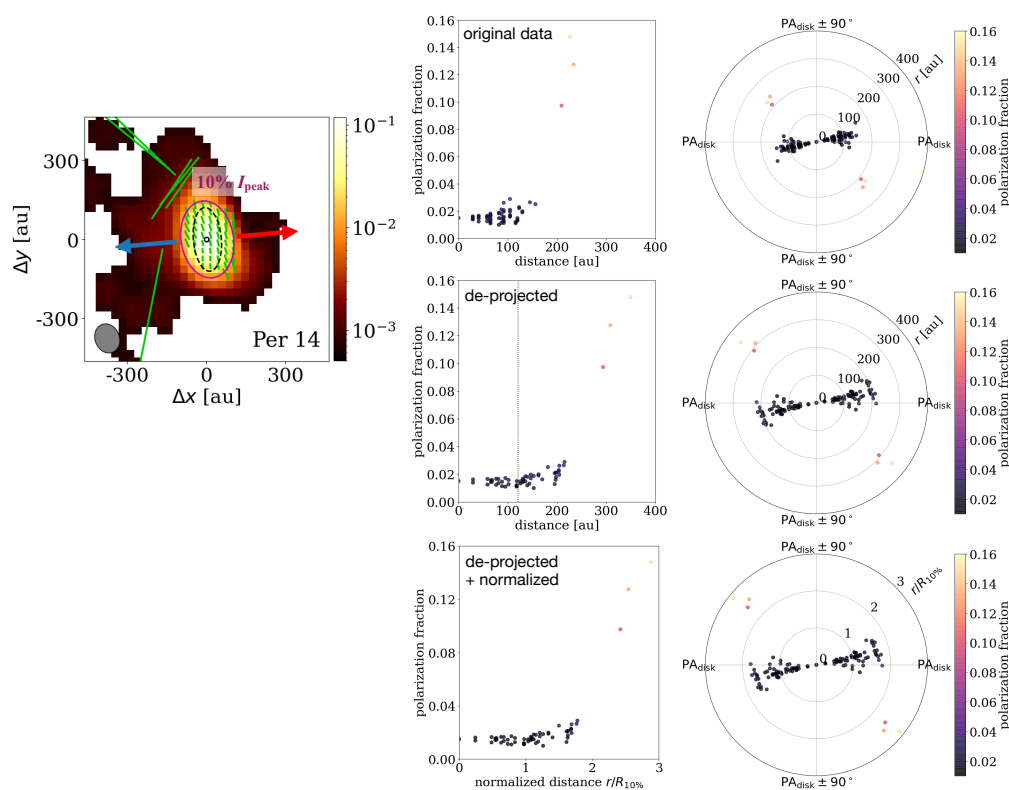


Figure 7.A.1: Demonstration of the deprojection and renormalization effects on observation data, using Per 14 as the example. *Left*: total intensity map (in Jy per beam) and polarization (B-)vectors from ALMA Band 7 observation presented in Cox et al. (2018), with outflow directions indicated by blue and red arrows and beam in the lower left corner. The Gaussian-fitted 10 percent peak intensity contour (*purple ellipse*) and the inferred disk adopted in the deprojection process (radius =  $R_{10\%}$  percent and inclination =  $45^\circ$ ; *black dashed ellipse*) are also marked. *Middle and right*: similar to Fig. 7.1 but for the original (*top*), deprojected (*middle*), and deprojected and normalized (*bottom*) data of Per 14. The polarization fraction is color coded, with the color bar shown on the right.

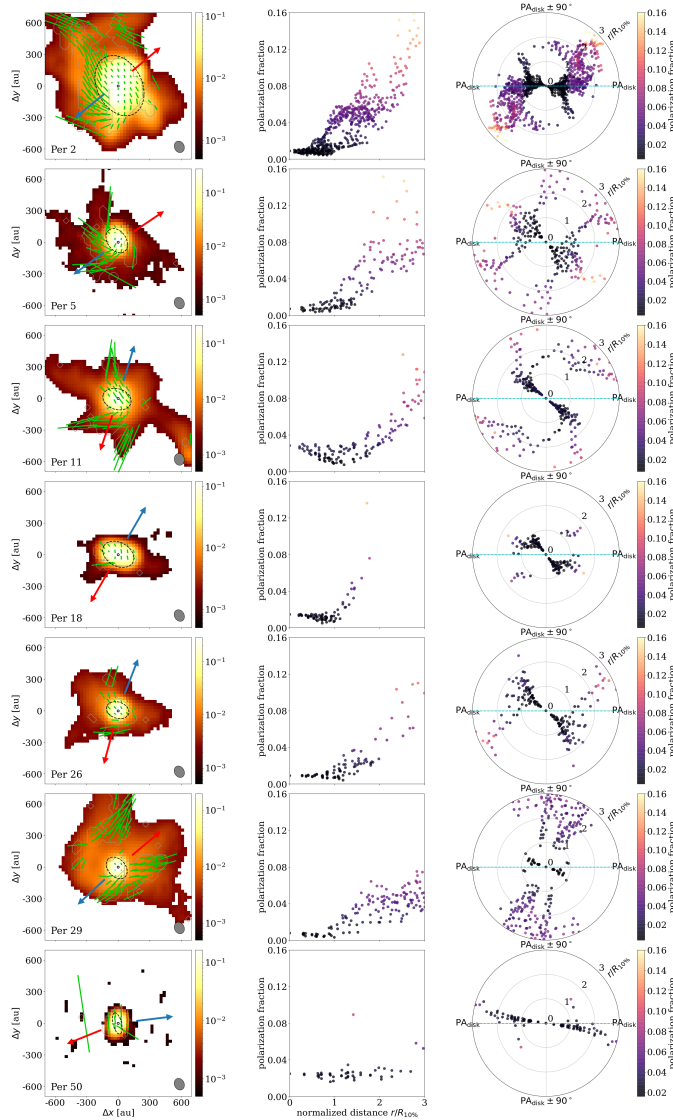


Figure 7.A.2: Summary of the ALMA Band 7 polarization observations towards the eight protostellar systems investigated in this study (with the exception of Per 14) and the deprojection results. Plotted are the ALMA Band 7 polarization B-vector map (*left column*) superposed on the dust continuum (background color map in Jy per beam with mask  $I > 5\sigma_I$ , outflow direction indicated by red and blue arrows and beam in the lower right corner), the scatter plots of the polarization fraction as a function of the normalized distance (*middle column*; darker color means more pixels), and the scatter plots of the B-vector orientations ( $0^\circ$  for north, *right column*) with the “disk plane” defined from the outflow direction marked as the dashed horizontal cyan line (i.e. the polar plots are rotated so that the position angle of the disk is horizontal). The polarization fraction is color coded, with the color bar shown on the right.

Table 7.A.1: Deprojection parameters for individual sources.

Target	PA <sup>a</sup> (°)	Inclination <sup>b</sup> (°)	$R_{10 \text{ percent}}$ (AU)	Regridded 0.1 arcsec	Regridded 0.2 arcsec
Per 2	39	45	311	301	313
Per 5	35	45	126	126	139
Per 11	72	44 <sup>c</sup>	138	137	154
Per 14	5	64 <sup>c</sup>	123	121	134
Per 18	60	45	161	158	166
Per 26	72	45	109	109	125
Per 29	42	45	117	117	136
Per 50	14	67 <sup>c</sup>	103	103	126

<sup>a</sup> The disk major axis is taken to be perpendicular to the outflow direction given in Stephens et al. (2018).

<sup>b</sup> Assumed to be 45° unless otherwise noted.

<sup>c</sup> From Segura-Cox et al. (2018).

## 7.B STRANDS IN POLARIZATION FRACTION–RADIUS HISTOGRAMS

In this appendix, we discuss the origin of the strands seen in the polarization fraction–radius histograms from both synthetic and real observation data (e.g. Fig. 7.1 and Fig. 7.3). Note that these strands are composed by  $p$ – $R$  bins with higher counts of pixels from the map, and these bins must be spatially connected in the radial direction to form strands. Their origin can thus be understood by considering the variation of polarization fraction azimuthally at a constant radius. Using the smoothed Model Xi-100-Sca as an example, we follow the spatial distribution of one particular strand (from  $p \approx 0.06$ ,  $r = 200$  AU, to  $p \approx 0.04$ ,  $r = 300$  AU; see the top-left panel of Fig. 7.B.1) in the physical space by plotting the polarization fraction as a function of the azimuthal angle  $\phi$  of each pixel on the map at 200, 250 and 300 AU (Fig. 7.B.1, top-middle). When transforming these curves into the counts in bins of the  $p$ – $R$

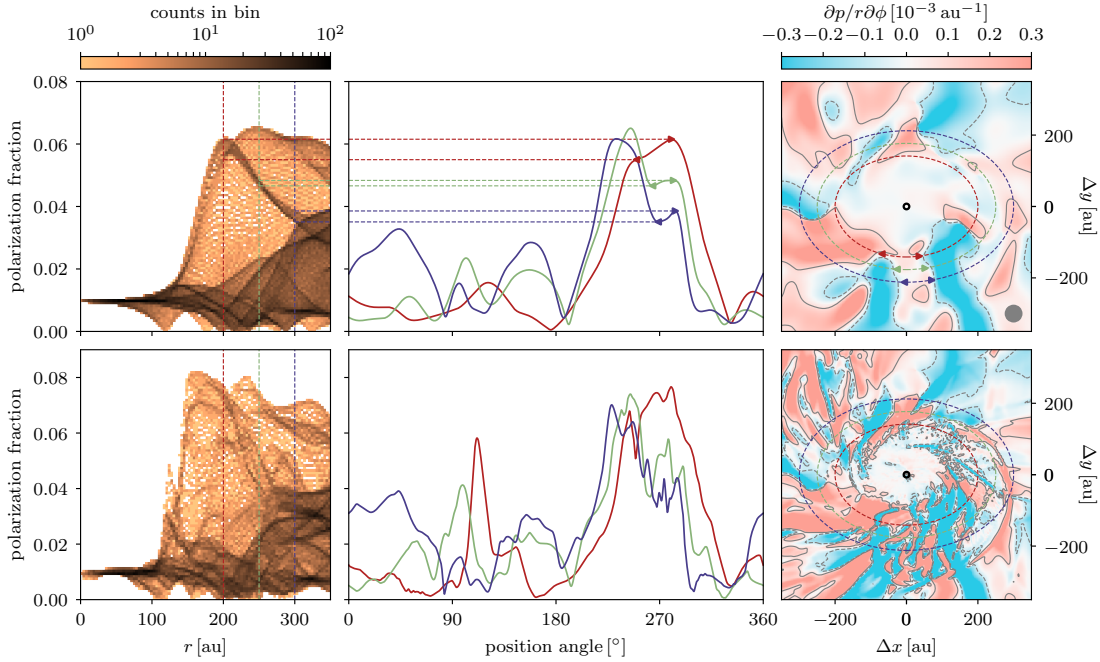


Figure 7.B.1: Illustration of the origin of the strands seen in the polarization fraction–radius histogram. Plotted are Models Xi-100-Sca with (*top*) and without (*bottom*) Gaussian beam smoothing (without masking) after deprojection. *Left*: 2D histogram of the polarization fraction–radius correlation. *Middle*: polarization fraction plotted against deprojected position angle  $\phi = \arctan 2(y, x)$  at  $r = 200$  (*red*),  $250$  (*green*) and  $300$  (*blue*). *Right*: ellipses of constant deprojected radii plotted on a map of azimuthal gradient of polarization fraction  $\partial p/r\partial\phi$ ; contours are at levels  $\pm 10^{-4} \text{ AU}^{-1}$ . The left/right triangle markers mark the region that has small gradient, which corresponds to the origin of the particular strand (see text). The beams used for smoothing are plotted in grey in the bottom-right corner.

histogram, if there is little variation in polarization fraction within a certain range of angles, the count of pixels in the corresponding  $p - R$  bin is higher, because mathematically, the sampling frequency for the  $p - R$  histogram is inversely proportional to the gradient  $\partial p/r\partial\phi$ .

To further illustrate the idea, we plot the azimuthal gradient of the polarization fraction ( $\partial p/r\partial\phi$ ) in the right column of Fig. 7.B.1 (top row). Using the same strand discussed above as an example (which is marked by the left/right triangles in the

middle panel of Fig. 7.B.1), the variation in polarization fraction is relatively small in the region on the map corresponding to the strand, which is located at the lower-side of the disk ( $\sim 270^\circ$ ; see the left/right triangles on the map). Indeed, the  $\partial p/r\partial\phi$  values are consistent with that of the aforementioned strand as we expected.

We would also like to point out that the feature of strands is not exclusive to the smoothed model but an intrinsic property of the synthetic observation. As illustrated in the bottom row of Fig. 7.B.1, although less visible, the strands can still be seen easily in the unsmoothed model at similar locations. This feature is highlighted in the smoothed model because of the reduction of local variations in polarization fraction due to Gaussian beam averaging, which could also explain the prominent strands seen in the ALMA data (see Fig. 7.A.2).

We also note that the gradient of polarization fraction is spatially coherent in a sense that the gradient has the same  $\pm$  sign (pink/cyan color in the right-hand panels of Fig. 7.B.1) in patches slightly spiralling inwards in the counter-clockwise direction. Such behavior is more significant in the unsmoothed model (bottom-right map in Fig. 7.B.1). When comparing these patterns to the 3D disk structure (see e.g. Fig. 3 in Lam et al. 2019), we find these spirals coincide with the trajectory of the infalling materials and the warped pseudo-disk. A detailed analysis of this behavior is beyond the scope of this paper and is postponed to a future investigation.

## 7.C EXTINCTION OF POLARIZED EMISSION

To properly account for the extinction of polarized emission, one needs to solve the vector radiation transfer equation:

$$\frac{d}{\rho ds}\mathbf{S} = -\mathcal{K}\mathbf{S} + B_\nu(T)\mathbf{a}. \quad (7.11)$$

where  $\mathbf{S} = (I, Q, U)$  is the radiation (Stokes) vector,  $s$  the distance along the light path, and  $B_\nu(T)$  the Planck function. The extinction matrix  $\mathcal{K}$  and absorption vector  $\mathbf{a}$  are related to the extinction and polarization opacities,  $C_e$  and  $C_p$ , by (see e.g. the POLARIS code Reissl et al. 2016)

$$\mathcal{K} = \begin{pmatrix} C_e & C_p \cos 2\psi & C_p \sin 2\psi \\ C_p \cos 2\psi & C_e & 0 \\ C_p \sin 2\psi & 0 & C_e \end{pmatrix}, \quad (7.12a)$$

$$\mathbf{a} = \begin{pmatrix} C_e & C_p \cos 2\psi & C_p \sin 2\psi \end{pmatrix}^T, \quad (7.12b)$$

where  $\psi$  is the angle between the magnetic field and the direction of positive  $Q$  in the sky plane. Taking into account of the magnetic alignment condition, as specified by the magnetic alignment probability  $A$ , defined in equation (7.10), we have the extinction and polarization opacities given by:

$$C_e = \kappa \left\{ 1 - \alpha \left[ A \left( \frac{\cos^2 \gamma}{2} - \frac{1}{3} \right) - \frac{1 - A}{6} \right] \right\}, \quad (7.13a)$$

$$C_p = \kappa \alpha A \cos^2 \gamma, \quad (7.13b)$$

where  $\kappa$  is the dust opacity (cross-section per gram of gas rather than dust), which is taken to be  $\kappa = 1.75 \times 10^{-2} \text{ cm}^2 \text{ g}^{-1}$  (assuming a gas-to-dust mass ratio of 100) at Band 7 (Ossenkopf & Henning 1994, logarithmically interpolated at  $870 \mu\text{m}$ ).

One way to solve the vector radiative transfer equation (7.11) is through the formal solution for the Stokes vector

$$\mathbf{S} = \int \mathcal{T}(s) \frac{\mathbf{a} + \mathbf{a}_{\text{sca}}}{\kappa} \rho ds \quad (7.14)$$

where the vector

$$\mathbf{a}_{\text{sca}} = \begin{pmatrix} 0 & -p_{\text{sca}}(1-A)C_e & 0 \end{pmatrix}^T \quad (7.15)$$

accounts for the scattering-induced polarization included in one of the models in those simulation cells where the magnetic alignment condition is not met (i.e.  $A = 0$ ), and the matrix  $\mathcal{T}(s)$  is obtained from the integral

$$\mathcal{T}(s) = \Pi_s^\infty e^{-\mathcal{K}(s')\rho ds'} \quad (7.16)$$

where  $\Pi_s^\infty$  denotes the (order-preserved) geometric integration along the light path from the point of interest ( $s$ ) to the “observer” at infinite distance of a function with a matrix exponential. Note that the Stokes parameters (I, Q, U) obtained from equation (7.14) at a given frequency  $\nu$  are normalized by the product  $\kappa B_\nu(T)$  at the frequency, as in equation (7.8) for the optical thin limit. Indeed, equation (7.14) reduces back to equation (7.8) by setting  $A = 1$  (magnetically aligned everywhere) and  $\kappa \rightarrow 0$  (optically thin).



## Part III

# Code Development

CHAPTER 8

# SELF-GRAVITY SOLVER – MULTIPOLE EXPANSION

*The self-gravity solver described in this Chapter has been used in the papers Barger et al. (2021), Jin et al. (2022, accepted), Jones et al. (2022, accepted), Tu et al. (2022, accepted), and in an ongoing astrochemical project by Prof. Garrod's group.*

Gravity is arguably the most indispensable piece of physics in star formation; it is the weight of clouds and cores that leads to their collapse. Given a density profile, the gravitational potential can be obtained by solving Poisson's equation

$$\nabla^2\Phi_g = 4\pi G\rho, \tag{8.1}$$

and the gravitational acceleration is

$$\mathbf{g} = -\nabla\Phi_g. \tag{8.2}$$

Its solution is straightforward when the mass of the system is dominated by a limited

number of point sources. However, this is not the case in the early phases of star formation and it is critical to consider the effects of self-gravity. For example, the mass of circumstellar disks as discussed in Chapter 6 is about 10% of the protostellar mass, which has significant effects on the dynamics. In fact, the gravity of the disks is responsible for the development of spirals and disk fragmentation shown in the rightmost column of Fig. 6.6.

Existing self-gravity solvers use techniques including but not limited to successive overrelaxation, fast Fourier transform, and multigrid to achieve computational time scaling of  $\mathcal{O}(n^{1.5})$ ,  $\mathcal{O}(n \log(n))$ , and  $\mathcal{O}(n)$ , respectively, where  $n$  is the number of cells. On paper, multigrid solvers appear to be optimal for a large number of cells. However, implementing a multigrid solver is known to be challenging, and the implementation details also affect the convergence rate as well as performance. Another solver, multipole expansion, is based on expanding the solution into an infinite series of spherical harmonics (Müller & Steinmetz 1995). This solution can be approximated by truncating the series at  $l = l_{\max}$  and  $m = m_{\max}$ , where  $l$  and  $m$  are the degree and order of spherical harmonics. After the truncation, the method has a computational time scaling of  $\mathcal{O}(n l_{\max} m_{\max}) = \mathcal{O}(n)$  if  $l_{\max}$  and  $m_{\max}$  are constants. Multipole expansion solvers are particularly well-suited for solving problems with spherical geometry such as core-collapse supernovae (Couch et al. 2013). Spherical polar coordinates with logarithmic spacing in the radial direction also provide high dynamic ranges in length-scale automatically, making it especially suitable for simulating star and disk formation. For this reason, we follow Müller & Steinmetz (1995) and implement multipole expansion solver in *Athena++*. It enables the use of the *Athena++* for 2D (axisymmetric) disk formation and evolution studies that include chemistry and grain growth.

## 8.1 MATHEMATICAL BASIS

### 8.1.1 Expansion in spherical harmonics

It is well-known that the solution to Poisson's equation can be written as an integral

$$\Phi_g(\mathbf{x}) = -G \int d^3\mathbf{x}' \frac{\rho(\mathbf{x}')}{|\mathbf{x} - \mathbf{x}'|}. \quad (8.3)$$

In order to express the solution in terms of spherical harmonics, we can first write  $|\mathbf{x} - \mathbf{x}'|$  into a sum of spherical harmonics using the generating function of the Legendre polynomial and the addition theorem for spherical harmonics as in Müller & Steinmetz (1995):

$$\frac{1}{|\mathbf{x} - \mathbf{x}'|} = \sum_{l=0}^{\infty} \sum_{m=-l}^l \frac{4\pi}{2l+1} Y_l^m(\theta, \phi) Y_l^{m*}(\theta', \phi') \frac{r_{<}^l}{r_{>}^{l+1}}, \quad (8.4)$$

where  $r_{<} = \min(r, r')$  and  $r_{>} = \max(r, r')$ . Therefore, the solution becomes

$$\begin{aligned} \Phi_g &= -G \sum_{l=0}^{\infty} \sum_{m=-l}^l \frac{4\pi}{2l+1} Y_l^m(\theta, \phi) \int d^3\mathbf{x}' Y_l^{m*}(\theta', \phi') \frac{r_{<}^l}{r_{>}^{l+1}} \rho(\mathbf{x}') \\ &= -G \sum_{l=0}^{\infty} \sum_{m=-l}^l \frac{4\pi}{2l+1} Y_l^m(\theta, \phi) (r^{-l-1} M_{l,\text{in}}^m(r) + r^l M_{l,\text{out}}^m(r)), \end{aligned} \quad (8.5)$$

with the inner and outer multipole moments function

$$\begin{aligned} M_{l,\text{in}}^m(r) &= \int_{4\pi} d\Omega' Y_l^{m*}(\theta', \phi') \int_0^r dr' r'^{l+2} \rho(\mathbf{x}'), \\ M_{l,\text{out}}^m(r) &= \int_{4\pi} d\Omega' Y_l^{m*}(\theta', \phi') \int_r^{\infty} dr' r'^{-l+1} \rho(\mathbf{x}'), \end{aligned} \quad (8.6)$$

$$d\Omega = \sin \theta d\theta d\phi.$$

We note that, although the spherical harmonics are usually written in the complex form using complex exponentials, the real form has the same algebraic properties.

Using the real form also has the benefit of reducing the computational cost. Therefore, we can replace both  $Y_l^m$  and  $Y_l^{m*}$  by

$$Y_{lm} = \begin{cases} \sqrt{2} \sqrt{\frac{2l+1}{4\pi} \frac{(l-|m|)!}{(l+|m|)!}} P_l^{|m|}(\cos \theta) \sin(|m|\phi) & \text{if } m < 0 \\ \sqrt{\frac{2l+1}{4\pi}} P_l^m(\cos \theta) & \text{if } m = 0 \\ \sqrt{2} \sqrt{\frac{2l+1}{4\pi} \frac{(l-m)!}{(l+m)!}} P_l^m(\cos \theta) \cos(m\phi) & \text{if } m > 0, \end{cases} \quad (8.7)$$

where  $P_l^m$  is the associated Legendre polynomial. With an additional assumption that the density is piecewise constant so that it can be moved outside of the integrals, the multipole moments in equation (8.6) can be evaluated exactly with the help of the recurrence relations of associated Legendre functions and the indefinite integrals of associated Legendre functions (equations 5, 6, 12, and 26 in DiDonato 1982).

### 8.1.2 Implementation

Computing the integrals in equation (8.6) for all radii directly would lead to a computational time scaling of  $\mathcal{O}(n_r^2 n_\theta n_\phi)$ , where  $n_r$ ,  $n_\theta$ , and  $n_\phi$  are the numbers of cells in the  $r$ -,  $\theta$ -, and  $\phi$ -direction, respectively. Therefore, as in Müller & Steinmetz (1995), the partial integrals over the volume of each shell are first computed. Then, the multipole moments as a function of the radius would be the cumulative sum of the partial integral in the radial direction.

Since the integrals less the density are time-independent, they are constant coefficients that can be precomputed and stored at the beginning of the simulation in order to improve the performance. However, in theory, there are  $l_{\max} m_{\max}$  coefficients per cell, which makes storing the coefficients directly unrealistic when  $l_{\max}$  is large. Nonetheless, the three-dimension integrals can each be separated into three one-dimension integrals, and a lot of them are in fact shared by the cells with

the same indices on the grid. The memory complexity is, therefore, reduced from  $O(l_{\max} m_{\max} n_r n_\theta n_\phi)$  to  $O(l_{\max} m_{\max}(n_r + n_\theta + n_\phi))$ .

In our implementation, we precomputed and stored the coefficients for computing multipole moments during the initialization phase. A one-dimensional logarithmic grid, which matches the grid of the hydro quantities, for storing and interpolating the multipole moments at different radii is constructed. Then, at each time-step, the multipole moments are computed and interpolated to each cell, using which and the spherical harmonics the gravitational potential is computed and stored at the cell centers.

## 8.2 POTENTIAL OF MACLAURIN SPHEROIDS

### 8.2.1 Analytical solution

A MacLaurin spheroid is a uniform spheroid with uniform density. Mathematically,

$$\rho(x, y, z) = \begin{cases} \rho_0 & \text{if } \frac{x^2}{a^2} + \frac{y^2}{b^2} + \frac{z^2}{c^2} < 1, \\ 0 & \text{otherwise.} \end{cases} \quad (8.8)$$

As discussed in Couch et al. (2013), the gravitational potential of a MacLaurin spheroid can be expressed analytically. MacMillan (1958) derived a solution for an

ellipsoid that can be expressed using Carlson's symmetric form of elliptic integral:

$$\begin{aligned} \Phi_g = 2\pi a b c \rho_0 & \left\{ R_F(\tilde{a}^2, \tilde{b}^2, \tilde{c}^2) - \frac{1}{3} \left[ R_J(\tilde{a}^2, \tilde{b}^2, \tilde{c}^2, \tilde{a}^2) x^2 + \right. \right. \\ & \left. \left. R_J(\tilde{a}^2, \tilde{b}^2, \tilde{c}^2, \tilde{b}^2) y^2 + R_J(\tilde{a}^2, \tilde{b}^2, \tilde{c}^2, \tilde{c}^2) z^2 \right] \right\}, \\ R_F(x, y, z) &= \frac{1}{2} \int_0^\infty \frac{dt}{\sqrt{t+x}\sqrt{t+y}\sqrt{t+z}} \\ R_J(x, y, z, p) &= \frac{3}{2} \int_0^\infty \frac{dt}{(t+p)\sqrt{t+x}\sqrt{t+y}\sqrt{t+z}} \\ \tilde{a}^2 &= a^2 + \kappa, \quad \tilde{b}^2 = b^2 + \kappa, \quad \tilde{c}^2 = c^2 + \kappa, \end{aligned} \tag{8.9}$$

where  $\kappa = 0$  if  $x^2/a^2 + y^2/b^2 + z^2/c^2 < 1$ . Otherwise,  $\kappa$  is the positive root of the equation

$$\frac{x^2}{a^2 + \kappa} + \frac{y^2}{b^2 + \kappa} + \frac{z^2}{c^2 + \kappa} = 1. \tag{8.10}$$

Having an analytical solution makes it an excellent test for self-gravity solvers, as illustrated in the following.

## 8.2.2 Numerical results

We computed the potential of an oblate spheroid with an ellipticity of  $e = 0.9$ , i.e.,  $a = b$  and  $c \approx 0.436a$ , both analytically and numerically. The L2-norm of percentage error is computed for the different  $l_{\max}$  used and plotted in solid blue in Fig. 8.2.1. Theoretically, the error should converge to zero for large  $l_{\max}$ . However, the L2-norm converges to  $\lesssim 10^{-3}$  for large  $l_{\max}$ . We find that the converged value is limited by the resolution of the grid. With a grid with twice the resolution, the initial convergence rate is about the same while the error converges to a smaller value  $\lesssim 3 \times 10^{-4}$ .

Fig. 8.2.1 also show the results with higher ellipticities  $e = 0.99$  and  $0.999$ . As expected, the error converges slower for a higher ellipticity. The results can be ex-

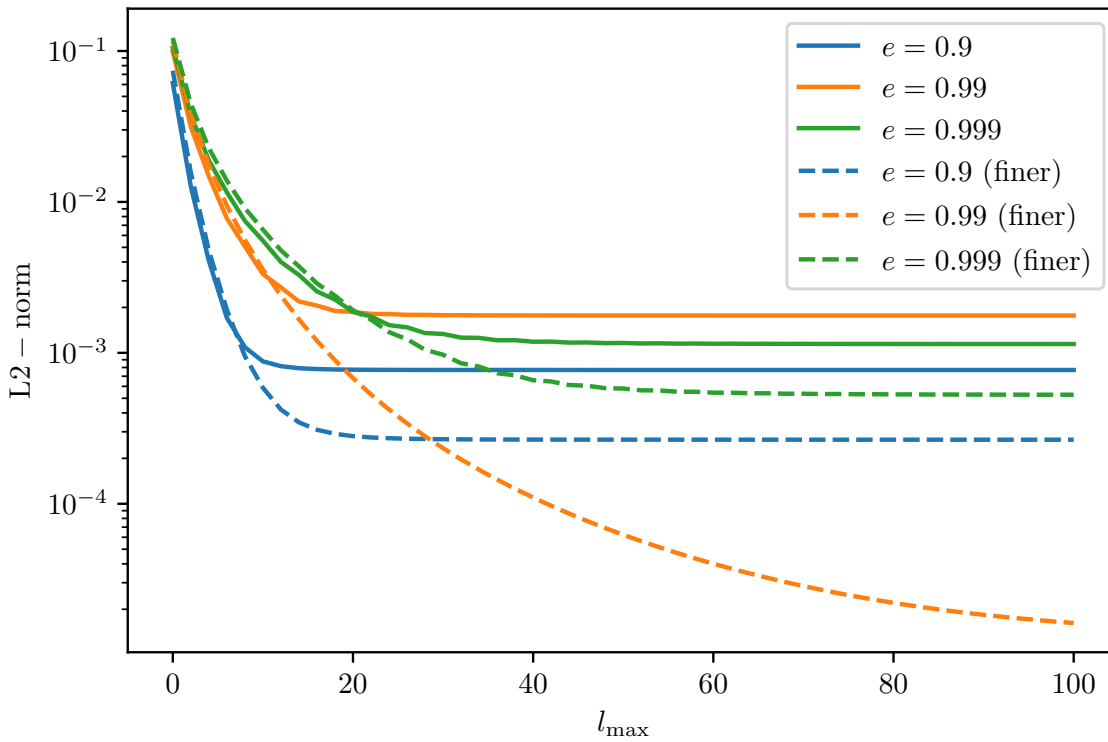


Figure 8.2.1: L2-norm of the percentage error of the potential of MacLaurin spheroids computed with different  $l_{\max}$ . The error of three spheroids with ellipticities  $e = 0.9$ ,  $0.99$ , and  $0.999$  are shown in blue, orange, and green, respectively. The results using coarse and fine grids are shown with solid and dashed lines, respectively.

plained with the zonal spherical harmonics  $m = 0$ . The zonal spherical harmonics (of the associated Legendre polynomial) of degree  $l$  have values alternating between positive and negative  $l$  times, forming  $l + 1$  zones from pole to pole. Therefore, to resolve a thinner structure, a large  $l$  is required.

Couch et al. (2013) observed that, in their implementation of cell-centered solver, the error attains a minimum at  $l_{\max} = 24$  and increases linear with  $l_{\max}$ . They found the increase in error is in fact due to the self-potential error when the mass of a cell is treated as a point source. The effect is not seen in this implementation because, as noted by Couch et al. (2013), the integrals in equation (8.6) are evaluated exactly by treating the density to be piecewise constant. It is likely that a straightforward calculation of the integrals using the mass and the spherical harmonics at the cell center leads to similar results.

### 8.3 APPLICATION – HOT CORES

Astrochemical modeling of molecular clouds and hot cores has made great progress since Garrod et al. (2008), which included the time dependency of the physical conditions of star-forming regions as well as complex chemical reactions. As has been shown numerous times, the warming of the environment has a significant impact on the abundance of complex species (Jørgensen et al. 2020 and reference therein). During the warm-up phase, the simple species on grains become able to efficiently diffuse and react to form complex species, which can then desorb into gas phase to be observed. However, chemical models usually have an over-simplified treatment of temperature. The flows in star-forming regions are complicated. Some may land directly onto the stars, while others may go through the disks and slowly be accreted or ejected as outflows. To approach this problem, we applied the self-gravity solver described above and make use of the existing radiation solver to model the collapse

of a hot core.

Part of this work that is conducted in one dimension (under the assumption of spherical symmetry) is published in *Astronomy and Astrophysics*. For the published results including both the physical and chemical model, please see Barger et al. (2021). Another work that also employed the self-gravity solver is Jin et al. (2022), which is accepted for publication also in *Astronomy and Astrophysics*. In Jones et al. (2022), we applied the same method to simulate the first core. In the following, we will outline the two-dimension physical model of hot cores, of which the investigation is ongoing.

### 8.3.1 Accretion phase

As in Barger et al. (2021), we solved the radiation-hydrodynamic equations assuming 2-D axisymmetry using *Athena++* with the additional cosmic-ray heating term and viscous diffusion term included in equations (1.17). Specifically, the equations solved are

$$\begin{aligned}
\frac{\partial \rho}{\partial t} + \nabla \cdot (\rho \mathbf{v}) &= 0, \\
\frac{\partial \rho \mathbf{v}}{\partial t} + \nabla \cdot (\rho \mathbf{v} \mathbf{v} + P + \Pi) &= -\rho \nabla \Phi_g - \mathbf{G}_r, \\
\frac{\partial E}{\partial t} + \nabla \cdot [(E + P) \mathbf{v} + \Pi \cdot \mathbf{v}] &= -\rho \mathbf{v} \cdot \nabla \Phi_g - G_r^0 + \rho \epsilon_{\text{CR}}, \\
\frac{\partial I}{\partial t} + c \mathbf{n} \cdot \nabla I &= S(I, \mathbf{n}),
\end{aligned} \tag{8.11}$$

where  $\Pi_{ij} = \rho \nu (\partial_j v_i + \partial_i v_j - (2/3) \delta_{ij} \nabla \cdot \mathbf{v})$  is the viscous stress tensor and  $\nu$  is the viscosity. The cosmic-ray heating rate  $\epsilon_{\text{CR}}$  is set to  $c \kappa_{a,P} a_r T_0^4$  to maintain the temperature at the initial temperature  $T_0 = 5$  K.

The equations are solved in spherical polar coordinates on a grid with 256 logarithmically-spaced cells in the radial direction and 64 uniformly-spaced cells in the polar direction.

We assume mirror symmetry about the mid-plane, where we applied the standard reflecting boundary condition, and the standard polar boundary condition is used at the pole. An outflow boundary condition is used for the hydro and a reflecting boundary condition is used for radiation at the inner radial boundary. The gas that flows through the inner boundary sets the accretion rate and is added to the mass of the central star. We used the precalculated stellar model taken from Hosokawa & Omukai (2009) which assumes an accretion rate  $10^{-3} M_{\odot} \text{yr}^{-1}$  to set the radius and the stellar luminosity of the central star. The accretion luminosity is computed using

$$L_{\text{acc}} = \frac{GM_*}{R_*} \dot{M}, \quad (8.12)$$

where  $M_*$  is the mass of the central star,  $R_*$  is the stellar radius obtained from the stellar model, and  $\dot{M}$  is the mass accretion rate. The radiation due to the total luminosity is applied to the inner boundary pointing radially outward. An outflow boundary condition is applied at the outer radial boundary. As in Barger et al. (2021), the inner boundary is set to 10 AU to resolve the dust sublimation front (Kuiper et al. 2010).

To obtain a relatively stable accretion rate, we assume a singular isothermal sphere density profile with  $80 M_{\odot}$  enclosed in a 0.1-pc sphere and a solid-body rotation of  $5 \times 10^{-13} \text{rad s}^{-1}$ . The initial accretion rate is expected to be  $\sim 1.4 \times 10^{-3} M_{\odot} \text{yr}^{-1}$ , slightly higher than the assumed accretion rate used in the stellar model, in order to accommodate the slow-down in accretion due to the anticipated formation of a disk. To drive accretion, the standard  $\beta$ -prescription for the kinematic viscosity  $\nu$  is adopted:

$$\nu = \beta \Omega_{\text{K}}(r) R^2, \quad (8.13)$$

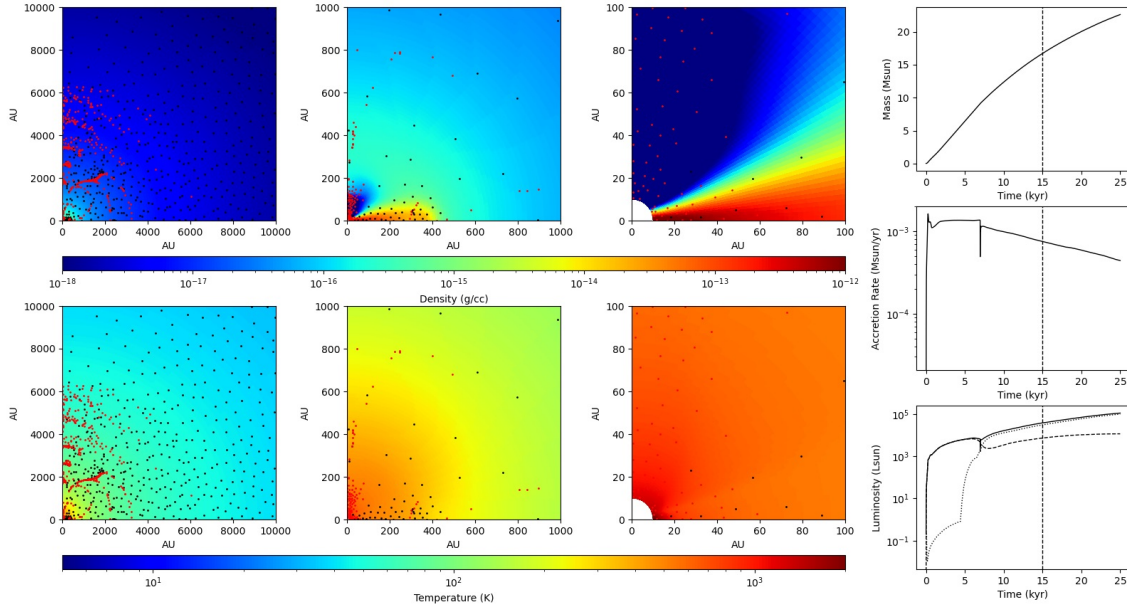


Figure 8.3.1: Snapshot of hot core simulation. The color on the top/bottom three panels shows the density/temperature at different scales. The points on the colored panels are the tracers. The color of the points denotes the tracer type with black, gray, and red representing mass-, space-, and gradient-tracers. The three panels on the right show the history of stellar mass (top), mass accretion rate (center), total luminosity (bottom solid), accretion luminosity (bottom dashed), and stellar luminosity (bottom dotted).

where  $R$  is the cylindrical radius and  $\Omega_K(r) = \sqrt{GM(r)/r^3}$ , with  $M(r)$  denoting the mass enclosed within a sphere of radius  $r$ . A value of 0.03 is used for the  $\beta$  parameter.

The simulation is run to 25 kyr since the accretion phase starts and a central stellar mass of  $\sim 23 M_\odot$  is obtained. Fig. 8.3.1 shows a snapshot of the simulation at 15 kyr. A rotationally-supported disk formed and the radiation of the central star cleared the polar region due to the radiation pressure.

In this phase, the gas is traced by about 2000 post-processing tracers. In order to obtain a fairly uniform tracer distribution in the final frame, the tracers are first initialized uniformly using a Poisson disk sampler in the last frame. Then, the velocity profiles of the (frequent) output of the simulation are taken and interpolated between

each output, which is used to integrate the tracers backward in time until the first frame. While integrating, tracers are constantly injected from the inner boundary to trace the gas that flows through the boundary.

To minimize the number of tracers used while maximizing the information needed for reconstructing the distribution of the gas, three types of samplers are used. The space-sampler is a regular Poisson disk sampler using the Bridson (2007) algorithm done in log-space. The algorithm begins with a few uniformly random samples. At each step, a candidate is chosen close to an accepted sample. A candidate is accepted if there is no sample closer than a certain distance. The process repeats until the space is completely sampled. Similar to space-sampler, the mass- and gradient-samplers use a modified Bridson algorithm. Instead of using a constant distance, the minimum accepted distance  $d$  is chosen locally based on the density and density gradient.

### 8.3.2 Condensation phase

Before the relatively short accretion phase, we extended the physical model backward in time analytically. The singular isothermal sphere profile used above is mapped smoothly to a uniform sphere with constant density  $\rho = 4.67 \times 10^{-21} \text{ g cm}^{-3}$ , corresponding to  $n_{\text{H}} = 2000 \text{ cm}^{-3}$  and a free-fall time of about 1 Myr. The mapping is performed by assuming mass conservation and that the flow does not cross each other. Each layer of the gas is assumed to move with initially roughly constant speed, which slows down close to the end of the condensation phase to match the initial conditions

of the accretion phase. Specifically,

$$\begin{aligned}
r(t, r_{\text{SIS}}) &= r_{\text{SIS}} + \Delta r \frac{\tau(t)}{\tau(0)}, \\
v_r(t, r_{\text{SIS}}) &= -\frac{\Delta r}{\tau(0)} \tanh\left(\frac{t_c - t}{t_s}\right), \\
\rho(t, r_{\text{SIS}}) &= \frac{M_{\text{core}}}{4\pi R_{\text{SIS}} r^2} \left[ \left( \frac{1}{3} \frac{r_{\text{US}}}{r_{\text{SIS}}} - 1 \right) \frac{\tau(t)}{\tau(0)} + 1 \right]^{-1}, \\
\tau(t) &= t_c - t - t_s \log\left( \tanh\left(\frac{t_c - t}{t_s}\right) + 1 \right), \\
r_{\text{US}} &\equiv \left( \frac{3}{4\pi} \frac{M_{\text{core}}}{\rho_0} \frac{r_{\text{SIS}}}{R_{\text{SIS}}} \right)^{1/3}, \quad \Delta r \equiv r_{\text{US}} - r_{\text{SIS}},
\end{aligned} \tag{8.14}$$

where  $r_{\text{US}}$  and  $r_{\text{SIS}}$  is the radial position of the tracer at the beginning of the condensation and accretion phases, respectively,  $t$  is the time since the beginning of the condensation phase,  $R_{\text{SIS}}$  is the radius of the core at the beginning of the accretion phases,  $M_{\text{core}}$  is the total mass of the core,  $\rho_0$  is the density of the uniform sphere, and  $t_c = 1 \text{ Myr}$  and  $t_s = 0.01 t_c$  are the condensation time and the length of the slow-down period.

The gas density, temperature, and velocity field sampled by each tracer particle as a function of time are then passed on to Prof. Garrod's group for astrochemical calculations and synthetic molecular line observations.

### 8.3.3 Work enabled by self-gravity solver

In combination with general barotropic EOS that is described in Chapter 9, the self-gravity solver has enabled the work published in Jones et al. (2022, accepted), of which the results will be summarized in Section 9.2. The self-gravity solver has also been used in Barger et al. (2021), Jin et al. (2022, accepted), and Tu et al. (2022, accepted), where radiation hydrodynamic simulations with self-gravity are carried out in spherical polar coordinates. In the following, the results of each paper are briefly

summarized.

Barger et al. (2021) presented the results of the first attempt in adopting physical conditions obtained from self-consistent 1-D radiation hydrodynamics simulations in hot-core chemical modeling. In the study, it is found that the gas-phase fractional abundances of the complex organic molecules (COMs) are different from previous modeling studies. The ice abundances and ice chemical composition are found to be affected by the gas density, which controls the mass accretion rate and accretion luminosity. Specifically, the higher accretion rate models agree better with typical observed values. Nonetheless, in general, gas-phase COMs are more abundant as the stellar mass, and hence, the stellar and accretion luminosities rise. There are some discrepancies between the 1D models and observations, which can be addressed with 2-D calculations that are ongoing.

In Jin et al. (2022, accepted), a methodology similar to Barger et al. (2021) was used to investigate the COMs in ice towards the first hydrostatic cores. It is found that the ice constituents have relative abundances comparable to typical observed values. Seven molecules are found to have abundances exceeding about 0.01% with respect to water ice. However, it is unlikely to be detected by the James Webb Space Telescope unless it is in COM-rich environments where solid-phase COM abundances exceed 1%.

In Tu et al. (2022, accepted), we carried out 2-D axisymmetric radiation hydrodynamic and grain growth simulation in spherical polar coordinates. “Terminal velocity approximation”, which is shown to be a valid assumption using Lagrangian particles, is adopted for the grain growth calculations. A growth timescale that is a function of local physical condition is obtained semi-analytically. By applying the physical conditions obtained from the radiation hydrodynamic simulation, it is found that the grain-grain collision induced solely by terminal velocity approximation is too slow to

grow grains from micron size to mm/cm size, which can be achieved by artificially increasing the collision speed by a factor of 4. The enhanced grain growth allows grains to settle faster towards the mid-plane, which further speeds up grain growth due to the increased dust-to-gas ratio.

## CHAPTER 9

# GENERAL BAROTROPIC EQUATIONS OF STATE

*The general barotropic EOS discussed in this Chapter was used in the paper Jones et al. (2022, accepted) and will be used in future refined non-ideal MHD disk formation simulations.*

As discussed in Chapter 1.2, the gas temperature can differ vastly between phases of star formation. As the density increases, the temperature increases at different rates. To accurately capture this process, complicated radiation hydrodynamics simulations with a realistic EOS have to be conducted (e.g. Tomida et al. (2013)). However, this kind of simulation is computationally expensive and the return is diminished when an accurate temperature is not the main goal. A compromise is to use a barotropic EOS that relates the density, temperature, and hence, pressure. This barotropic EOS is a much-needed improvement over the isothermal EOS used in the idealized simulations presented in Part II of the thesis because it controls the thickness of the formed disk, which is important for accurately computing the disk properties.

## 9.1 IMPLEMENTATION

The implementation of the general barotropic EOS is similar to the general EOS implemented in `Athena++`. The general barotropic EOS is implemented for the HLLE and HLLD solvers by replacing the pressure which is calculated using  $\rho c_s^2$  by that calculated using the barotropic EOS. Two new forms of barotropic EOS are implemented and discussed below.

### 9.1.1 Stiffened equation of state

Due to the low density, molecular clouds tend to be very efficient at cooling. Therefore, isothermal EOS is usually a reasonable assumption. However, one critical moment in protostellar collapse and star formation is when, as the density increases, the effective adiabatic index increases from 1 (isothermal at  $\sim 10$  K) to  $5/3$  (adiabatic with 3 degrees of freedom) when the core starts to become optically thick (Masunaga et al. 1998). Plotted in Fig. 9.1.1, an EOS that captures this effect is

$$T = T_0 \left[ 1 + \left( \frac{\rho}{\rho_{\text{crit}}} \right)^{\gamma-1} \right], \quad (9.1)$$

where  $T_0$  is temperature in the isothermal phase,  $\gamma = 5/3$  is the adiabatic index, and  $\rho_{\text{crit}} = 10^{-13} \text{ g cm}^{-3}$  is the critical density suggested by Masunaga et al. (1998). It is immediately clear that the EOS reduces to the isothermal EOS when  $\rho \ll \rho_{\text{crit}}$ , and  $T \propto \rho^{\gamma-1}$  when  $\rho \gg \rho_{\text{crit}}$ .

### 9.1.2 Smoothed multi-power-law equation of state

As the density continues to increase, the adiabatic index decreases first to  $7/5$  (adiabatic with 5 degrees of freedom) when the temperature reaches  $\sim 100$  K where the molecular hydrogen can be excited rotationally and vibrationally. When the gas

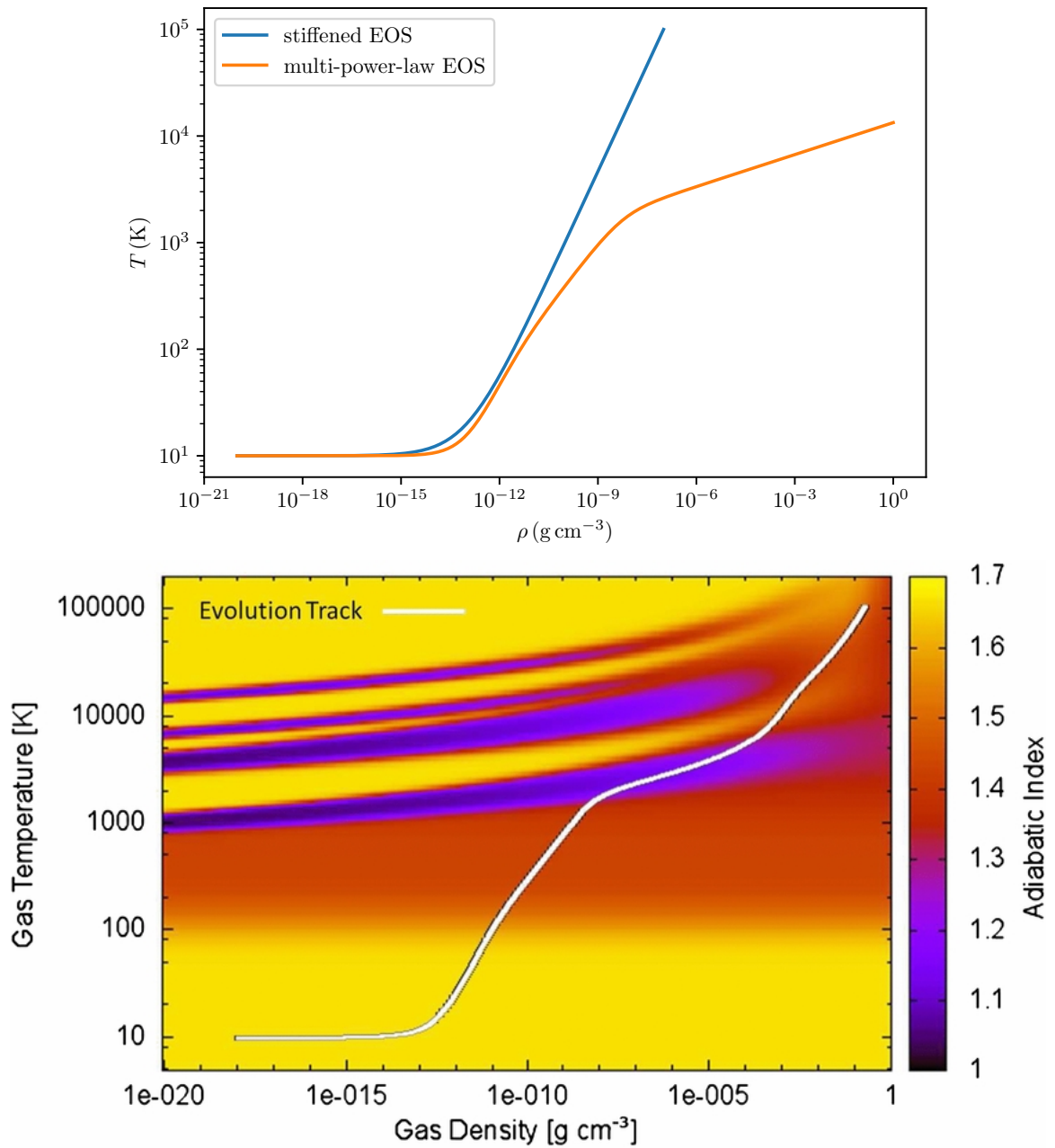


Figure 9.1.1: Temperature plotted as a function of density for different EOS fitted or obtained from simulations. The top panel show the “stiffened EOS” fitted from Masunaga et al. (1998) (blue) and “multi-power-law EOS” fitted from Tomida et al. (2013) (orange). The bottom panel shows an EOS obtained using realistic radiation magnetohydrodynamic simulation taken from Tomida et al. (2013).

temperature reaches 2000 K, the dissociation of molecular hydrogen begins and the effective adiabatic index decreases to  $\sim 1.1$  (e.g. Tomida et al. 2013). An EOS that mimics this behavior is to stitch together multiple power laws. To derive the equation, we start from the derivative

$$\frac{d \log T}{d \log \rho} = (\gamma_0 - 1) + \sum_{i=1}^n \frac{\gamma_i - \gamma_{i-1}}{1 + \exp(-\log \rho + \log \rho_{i-1,i})}, \quad (9.2)$$

where each term in the summation is a logistic function,  $\gamma_i$  is the  $i$ -th adiabatic index, and  $\rho_{i-1,i}$  is the  $i$ -th turn-over point (in ascending order). After rearranging and integrating,

$$\begin{aligned} \frac{d \log T}{d \rho} &= \frac{\gamma_0 - 1}{\rho} + \sum_{i=1}^n \frac{\gamma_i - \gamma_{i-1}}{\rho + \rho_{i-1,i}}, \\ T &= A \rho^{\gamma_0 - 1} \prod_{i=1}^n (\rho + \rho_{i-1,i})^{\gamma_i - \gamma_{i-1}}, \end{aligned} \quad (9.3)$$

where  $A$  is an arbitrary constant. It can be proven that it has the intended behavior by considering some density  $\rho$  that falls between two turn-over points,  $\rho_{j-1,j}$  and  $\rho_{j,j+1}$ , such that  $\rho \gg \rho_{k-1,k}$  for all  $k \leq j$  while  $\rho \ll \rho_{k,k+1}$  for all  $k \geq j$ . Therefore, all terms with  $i > j$  reduce to a constant, and the rest would be proportional to  $\rho^{\gamma_j - 1}$ .

To simulate the EOS in the Fig. 1 of Tomida et al. (2013), which is also shown in Fig. 9.1.1, the following parameters can be used:

$$\begin{aligned} A &= 10 \text{ K} \left/ \prod_{i=1}^n \rho_{i-1,i}^{\gamma_i - \gamma_{i-1}} \right., \quad \gamma_0 = 1, \quad \gamma_1 = 5/3, \quad \gamma_2 = 7/5, \quad \gamma_3 = 1.1, \\ \rho_{0,1} &= 10^{-13} \text{ g cm}^{-3}, \quad \rho_{1,2} = \rho_{0,1} \left( \frac{100 \text{ K}}{10 \text{ K}} \right)^{1/(\gamma_1 - 1)}, \quad \rho_{2,3} = \rho_{1,2} \left( \frac{2000 \text{ K}}{100 \text{ K}} \right)^{1/(\gamma_2 - 1)}. \end{aligned} \quad (9.4)$$

## 9.2 APPLICATION – CENTRIFUGAL BARRIER

Centrifugal barriers, features that rotate around protostars at a super-Keplerian speed, have been theorized to exist in early analytic models of rotating cloud collapse using a (non-interacting) test particle approach (Ulrich 1976; Cassen & Moosman 1981, CMU). However, the idea had once been dismissed probably due to its nonexistence in hydrodynamic simulations. It was brought to the attention of the star formation community recently by Sakai et al. (2014, 2017), who claimed observational evidence for the existence of centrifugal barriers. They presented a position-velocity diagram fitted remarkably well by the CMU model.

In Jones et al. (2022), we test the concept of centrifugal barriers through hydrodynamic simulations using the `Athena++` code with the multipole expansion self-gravity solver that I developed. In the simulations, we find the density exceeds the critical density  $10^{-13} \text{ g cm}^{-3}$ . Therefore, to ensure that the results are not affected by the choice of EOS, we adopted the stiffened EOS in this investigation. This work is accepted for publication in *Monthly Notices of the RAS*. In the following, we will outline the problem setup and summarize our results discussed in Jones et al. (2022).

### 9.2.1 Problem setup and results

In the work, we solve the following equations using `Athena++`:

$$\begin{aligned} \frac{\partial \rho}{\partial t} + \nabla \cdot (\rho \mathbf{v}) &= 0, \\ \frac{\partial \rho \mathbf{v}}{\partial t} + \nabla \cdot (\rho \mathbf{v} \mathbf{v} + P + \Pi) &= -\rho \nabla \Phi_{\text{g}}, \end{aligned} \tag{9.5}$$

where the gravitational potential  $\Phi_{\text{g}}$  is obtained by solving Poisson’s equation using the self-gravity solver described in Chapter 8. As in Section 8.3, the  $\beta$ -viscosity prescription is adopted with a wide range of  $\beta$  tested. Both uniform density and

singular isothermal sphere profiles with solid-body rotation are considered in the study to eliminate the effect of density profile on the results. The stiffened EOS described in Subsection 9.1.1 is used.

Super-Keplerian regions are identified in some of the simulations with large viscosity. However, we find that the results do not support the classical picture of centrifugal barriers since the radial infall of the envelope material is not slowed down primarily by the excess centrifugal force over the gravity. The super-Keplerian regions found in our simulations originated from viscosity transporting angular momentum from the center to the edge of the disks. Although the region is expected to quickly disappear as the disk expands, the ram pressure from the infalling envelope provides a constraint to the disk expansion and maintains the super-Keplerian rotation in the region.

## CHAPTER 10

## SINK PARTICLE TREATMENT

*The sink particle treatment discussed in this Chapter was used in the paper Lam et al. (2019) and will be used in future refined non-ideal MHD disk formation simulations.*

Sink particle treatments in one form or another have been one of the key ingredients in disk formation simulation. Studying the problem requires starting the simulation from prestellar cores or even earlier phases. The density would increase indefinitely due to the run-away collapse under the cores' own gravity. The constantly increasing density could cause numerical problems such as artificial fragmentation. In order to maintain the validity of the simulations, the Jeans condition, i.e. the Jeans length has to be resolved, has to be satisfied (Truelove et al. 1997). The numerical problem is, therefore, alleviated by applying adaptive mesh refinement (AMR). However, at the very center of every disk is a star, the interior of which has a Jeans length of  $10^{-3}$  AU, much smaller than the typical scale of a disk. Therefore, it is inevitable to truncate the refinement and use a sink particle to replace the over-dense region and suppress the fragmentation.

Sink particle treatment, or sink regions in general, has many variants. One of the examples is presented in Subsection 8.3, where the hole at the center of the

simulation is a sink that exists naturally in spherical polar coordinates. Due to the geometry of the problem and the logarithmic spacing that comes with spherical polar coordinates, it is a natural choice for studying disk formation. However, spherical polar coordinates suffer when the core is turbulent or instability develops, which can break the symmetry and cause the protostar to move. Therefore, disk formation in a realistic, turbulent cloud core is typically studied in Cartesian coordinates with a sink particle treatment as in Chapter 6. There are different implementations of sink particle treatment, and the one discussed below is based on Gong & Ostriker (2013) (hereafter referred to as GO13) that was implemented in an older version of *Athena* and is extended to work with the newer *Athena++* that has AMR capabilities.

## 10.1 DESIGN CHOICE AND IMPLEMENTATION

In most cases, sink particles are implemented in such a way that they would remove materials within a certain radius, and then act as point sources of gravity and sometimes provide feedback. In GO13, the sink particles are always at the central cell of a  $3 \times 3 \times 3$  region, which is defined as the controlled volume. At each time-step, threshold densities and momentum are calculated for all cells in the controlled volume by taking the average of the closest active cells. Anything that is above the threshold will be removed from the grid and added to the sink particle. The gravity of the sink particles is calculated using a particle mesh method. The calculation is combined with that of the grid by depositing, using triangular shaped cloud (TSC, Hockney & Eastwood 1981), the mass of the sink particles onto a temporary grid used by the self-gravity solver, and therefore, does not introduce any overhead. This implementation has been found to be robust in many studies (Gong & Ostriker 2015; Skinner & Ostriker 2015; Kim & Ostriker 2017), and therefore, forms the base of our treatment.

### 10.1.1 Creation

In *Athena++*, the time integration is divided into time-steps, and each time-step is integrated with multiple stages. The checks for creating sink particles are done at both the beginning of the simulation and at the end of each time-step. In order for a sink particle to be created, three criteria have to be satisfied. The first is the density threshold. As discussed earlier, it is essential to resolve the Jeans length by a certain number of cells. In order to suppress the artificial fragmentation, a sink particle should be created to replace the over-dense cells when the Jeans condition is violated. Truelove et al. (1997) suggest resolving the Jeans length by four cells, which gives a density threshold

$$\rho_{\text{Tr}} = \frac{\pi}{16} \frac{c_s^2}{G\Delta x^2}, \quad (10.1)$$

where  $\Delta x$  is the cell size. On the other hand, GO13 adopted a different threshold derived based on Larson (1969) and Penston (1969), who found a density profile

$$\rho_{\text{LP}}(r) = \frac{8.86}{4\pi} \frac{c_s^2}{Gr^2} \quad (10.2)$$

where the center formally reaches infinite density. The threshold used in GO13 is

$$\rho_{\text{LP}}(0.5\Delta x) = \frac{8.86}{\pi} \frac{c_s^2}{G\Delta x^2}, \quad (10.3)$$

which is larger than  $\rho_{\text{Tr}}$ . Although GO13 claims that the density at the exterior of the control volume is  $\rho_{\text{LP}}(2\Delta x) = 0.897\rho_{\text{Tr}}$ , in the worst case scenario, the density should be  $\rho_{\text{LP}}(1.5\Delta x) = 1.596\rho_{\text{Tr}}$ . Therefore, to be conservative,  $\rho_{\text{Tr}}$  is adopted as the threshold in our implementation.

The second criterion is that the newly created sink particle should be at least a

certain distance away from existing sink particles. This design choice is to avoid sink particles being created and merged with other sink particles in a short period, which avoids the creation of unnecessary accretion spikes to the parent sink particle (see Subsection 10.1.2 for more details).

The third, and last, criterion is that the sink particle needs to be at a gravitational potential minimum. When the previous two criteria are both satisfied, the potential of the over-dense cell, as well as that of its six neighbors, are checked. If all three criteria are satisfied, three parabolas are fitted independently in the  $x$ ,  $y$ , and  $z$  directions to the potentials. Since the potential is minimum in the center cell, the parabola fitted using this value and those of the two adjacent cells always exists and is unique, the vertex of which is also guaranteed to be within the center cell. After the parabolas are fitted, a sink particle with zero mass is created at the vertices. The velocity is obtained by interpolating the velocity on the grid trilinearly at the position of the sink particle.

### 10.1.2 Merging

The merge of sink particles happens right after the creation of sink particles. Two sink particles are flagged to be merged if they are closer than a certain distance, which is chosen to be  $2\Delta x$ . A straightforward implementation would have a time complexity of  $\mathcal{O}(n_{\text{sink}}^2)$ , where  $n_{\text{sink}}$  is the number of sink particles created. In disk formation simulations, usually, only a handful of particles would be created. However, the number could be much greater in other applications such as molecular cloud-scale simulations. Nonetheless, since the sink particles to be merged are physically close, the check has to be performed only on the sink particles in adjacent meshblocks, a subset of the whole computational domain, which should reduce the time complexity to linear.

After all checks are completed, the transaction occurs one by one using the total mass of the pairs as the priority. The sink particle with the higher mass of the two is considered the parent while the other is the child. The mass and momentum of the child would be transferred to the parent, and the parent would be moved to the center of mass of the two. The child is then flagged as merged. In the unlikely event that the total mass or the mass of each particle to has a tie, it is broken by the mass of the parent, then by the identifier of the parent, and finally by the identifier of the child. In the case where one of the sink particles in the pair is merged, the transaction is voided and the next transaction is processed. If there is at least one merging happened, the process beginning from the checking starts over again until no merging happens.

### 10.1.3 Advection and accretion

In GO13, the kick-drift-kick algorithm is implemented to ensure energy conservation. However, the sink particles are evolved using the same time-integrator as the hydro and magnetic field. We find that, with the higher-order time integrator implemented in `Athena++`, the energy conservation is at an acceptable level. The sink particles are coupled to the hydrodynamics through gravity and accretion. As in GO13, the mass of the sink particles is deposited onto the grid using TSC of size 3, which ensures an identical center of mass. The gravitational acceleration of the sink particles is obtained by, first, calculating the gravitational acceleration of each cell in the controlled volume. The accelerations of the cells are then averaged with weights determined by the TSC. Identical to GO13, the global integration time-step is restricted by the requirement that sink particles cannot travel further than one cell.

Another major change from GO13 is the accretion. As mentioned above, the gas above the accretion threshold in the control volume would all be accreted. However,

when the sink particles cross a cell, the control volume is shifted. This discrete behavior causes artificial spikes in the accretion rate, and therefore, is undesirable. Instead, we computed the density threshold  $\rho_{\text{acc}}$  for each cell individually using the six adjacent cells. Then, the TSC weight  $w$  is calculated, and only  $w \times \rho_{\text{acc}}$  is accreted to the sink particles. The momentum is treated similarly. However, in order to simulate the magnetic field decoupling from a star represented by a sink particle, the magnetic field is left untouched; i.e. sink particles do not carry magnetic flux.

### 10.1.4 Refinement

In theory, this implementation would work with any refinement level. When a sink particle touches meshblocks of different refinement levels, the size of the control volume should be set to 3 times the coarsest cell. However, possibly due to the numerical noise in the gravitational potential calculation currently implemented in *Athena++*, there is anomalous acceleration when a sink particle crosses the boundary between different refinement levels with this implementation. Consequently, sink particles are currently restricted to be at the highest refinement level. When sink particles are entering a coarser refinement level, the coarser grid is forced to refine.

## 10.2 APPLICATION – DISK FORMATION

Combining with the multi-power-law EOS described in Chapter 9, we can finally conduct a long-term simulation of disk formation using *Athena++*. As the first step, we repeat the calculations of Model M0.0AD1.0 in Chapter 6 using a much higher resolution in an attempt to confirm the validity of the results. The simulation box is initialized identically to the previous study. The computational domain is, however, twice as large, i.e. the box size is 10000 AU. The root grid has 128 cells in each direction. The central 5000 AU box is always refined at least once, which makes the

cell size at the center  $\sim 40$  AU initially. The maximum number of refinement levels is 6 such that the minimum cell size is  $\sim 1$  AU. The cells are refined following the Jeans condition such that the Jeans length is always resolved by four cells. To ensure the disk is well-resolved, the cells within 16 AU from the sink particles are refined to the highest level. The gravitational potential is computed using the multigrid solver.

As shown in Fig. 10.2.1, the central density reaches  $\sim 5 \times 10^{-12} \text{ g cm}^{-3}$ . In this instance, the pressure support is enhanced compared to the isothermal assumption. A first-core-like structure forms with a diameter of about 10 AU. The structure appears to be flattened by rotation. Eventually, a rotationally-supported disk forms as shown in Fig. 10.2.2. The magnetic field begins clearing the bipolar region by generating an outflow. Although the results are still preliminary and the simulation is still in a rather early phase, the formation of a rotationally-supported disk is consistent with the previous study.

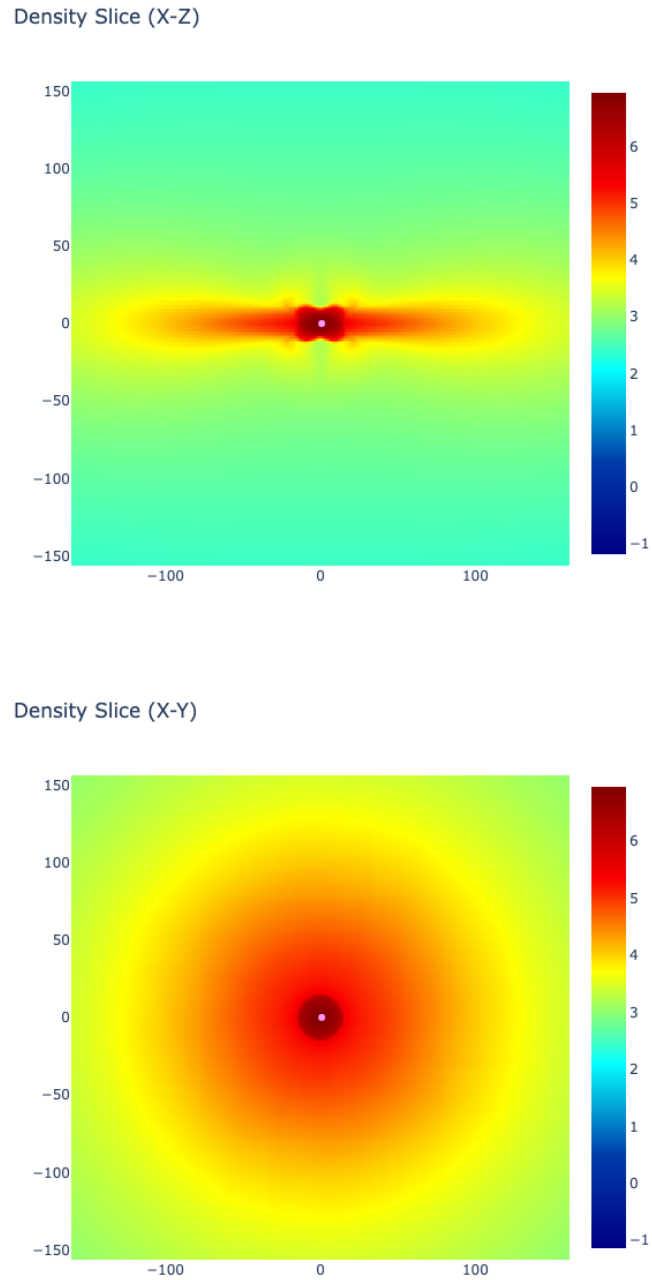
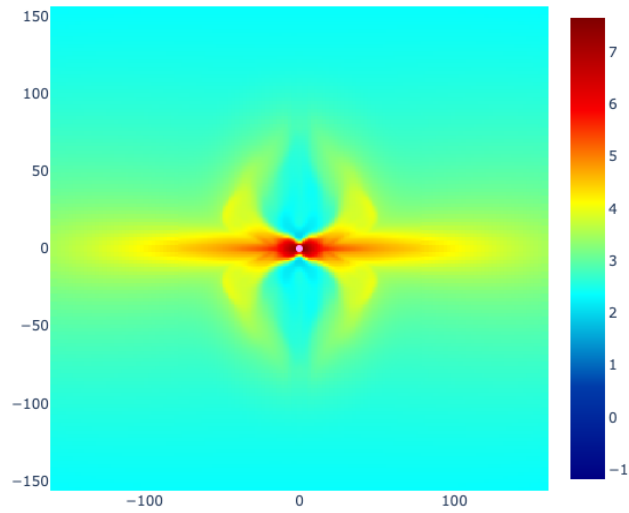


Figure 10.2.1: Edge-on (left) and face-on (right) density slices across the sink particle showing the formation of a first core. The color shows the density in the unit of  $5.94 \times 10^{-19} \text{ g cm}^{-3}$ . The sink particle representing the protostar is shown by a circle.

Density Slice (X-Z)



Density Slice (X-Y)

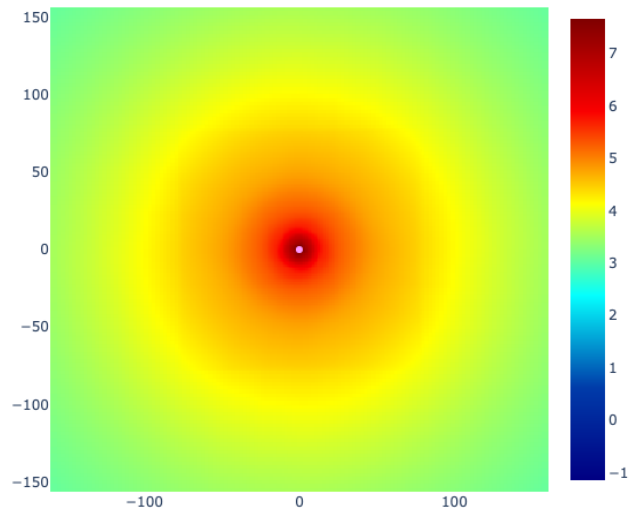


Figure 10.2.2: Edge-on (left) and face-on (right) density slices across the sink particle showing the onset of a rotationally supported disk. The color shows the density in the unit of  $5.94 \times 10^{-19} \text{ g cm}^{-3}$ . The sink particle representing the protostar is shown by a circle.



## Part IV

# Conclusion

## CHAPTER 11

# SUMMARY

This thesis approaches the formation of circumstellar disks around low-mass stars using numerical simulation in an effort to answer the questions of whether magnetized disks can form under realistic conditions and what the expectation is for an observed disk based on the simulations. Historically, disks are found to be readily suppressed by magnetic fields in simulations while observations of disks have become increasingly common thanks to ALMA. This discrepancy draws a lot of attention. Over the last decade, considerable research has been dedicated to answering these seem-to-be-trivial questions. As part of this effort, Chapters 6 and 7 contain the main results of this thesis.

In Chapter 6, we focus on the first question: can magnetized disk form in numerical simulations under realistic conditions. We carried out a large set of simulations with an initial pseudo-Bonnor–Ebert sphere profile and a strong but realistic uniform magnetic field. We confirm the suppression of disk formation and the existence of features such as pseudo-disks and DEMS (decoupling-enabled magnetic structure) under the ideal MHD assumption. By including turbulence that is prevalent in star-forming cores, we find short-lived disks can be formed with signs of enhanced rotation. We

attribute the formation of these short-lived disks to the early formation of DEMS, which allows leakage of magnetic flux. In addition, we discuss the possibility that warped pseudo-disks open up more channels for accretion, which in turn avoids the encounter of low- and high-angular momentum material, and therefore, angular momentum redistribution. Following turbulence, the effect of ambipolar diffusion (AD) is explored. We find that AD is efficient in decoupling the magnetic flux from the gas. Therefore, the reduced magnetic braking, as a result of flux redistribution and reduction of field pinching caused by AD, is responsible for re-enabling the formation of disks. In the presence of both processes, we further find that, although AD is more efficient, turbulence helps stabilize the disk. Lastly, we identify the disks formed in the simulation and measure their degree of magnetization. We find that the magnetization is far stronger than what is typically assumed in the literature to drive accretion in protoplanetary disks.

In Chapter 7, we carry out synthetic observations using the simulations obtained in the previous chapter to explain polarimetry observations of protostars. A reexamination of the data shows that the depolarization occurs in the disk scale, where the polarization aligns predominantly to the minor axes of the disks. By comparing the grain alignment time-scale with the gas damping time-scale, a model allowing grain misalignment is constructed. While depolarization is found in the synthetic observation, the trend that polarization favors aligning to the minor axis is not reproduced. However, by involving scattering, the results reproduce the observed trend. This phenomenon can be explained by the fact that density increases much faster than the magnetic field strength as the radius decreases.

To support projects by collaborators and in preparation for future investigations using *Athena++*, the development of self-gravity solver, general barotropic EOS, and sink particle treatment is described in Chapters 8, 9, and 10. In Chapter 8, we present

the multipole expansion solver that is implemented, together with the testing based on MacLaurin spheroid and an application of the module to simulate hot cores around a massive protostar. Two forms of general EOS are derived in Chapter 9, and their importance and application are discussed.

In Chapter 10, the sink particle treatment, the key ingredient that enables long-term disk formation simulation, is described. Based on GO13 which introduces an implementation of sink particle treatment in *Athena*, our freshly implemented sink particle treatment in *Athena++* not only preserves the strengths of the GO13's implementation but also improves its weaknesses discovered during the study in Chapter 6. Of the utmost importance is the improvement in eliminating artificial accretion spikes through gentler accretion. In this implementation, nearby meshblock refinement is enforced to make it compatible with AMR. The treatment is finally brought to the test in the high-resolution disk formation simulations that repeat those in Chapter 6. In the simulations, we discover a first-core-like structure enabled by the general barotropic EOS described in Chapter 9, as well as a rotationally-supported disk consistent with previous results.

## CHAPTER 12

**FUTURE WORK**

While this thesis begins with exploring the possibility of forming circumstellar disks from prestellar dense cores, over the past few years, the community is slowly reaching a consensus that non-ideal MHD effects rescue disk formation from the magnetic braking catastrophe. The focus has been shifting towards understanding the disk structures and properties, their evolution, and their relation to the surrounding environments. Disk formation is closely related to planet formation, and understanding the process of disk formation can certainly shed light on planet formation. In connection to this thesis, a straightforward extension to the current work is to perform the calculations similar to that in Chapter 6 for investigating the long-term results.

One of the major caveats in the previous investigation is the limited spatial resolution, which calls for AMR simulations. With all the numerical tools required now becoming available, we would be able to resolve disk structures and precisely assess their properties. Disk magnetization, which sets the accretion rate of a disk, is one of the properties that have great impact on planet formation. By measuring the magnetization, we can constrain the initial conditions needed for simulating the evolution of protoplanetary disks, which is suggested to be where most of the dust growth

happens.

While this thesis focuses only on the evolution until soon after the formation of circumstellar disks, gas-dust simulations that follow the evolution all the way from prestellar cores to protoplanetary disks can further expand our understanding of planet formation. The flows of gas during the formation of disks are complex and consist of turbulence, outflows, and accretion streams. Although the flows of dust can be vastly different from those of the gas, the former can still be largely modified by the latter. With the high-resolution simulation, the vertical structures and meridional motions of the disks can be resolved. These kinds of motions can stir up the dust at the mid-plane or circulate the dust within the disks, and therefore affect dust coagulation.

Finally, an ongoing ALMA large program, eDisk, may provide the best testing ground for our current knowledge in disk formation. With the proposed high-resolution continuum emission and CO isotopologue lines observations towards 17 embedded disks around Class 0/I protostars, we would be able to compare the observed dust with the gas structures in detail. These observed results might be further compared with what is predicted in future AMR simulations.

## BIBLIOGRAPHY

- Allen, A., Li, Z.-Y., & Shu, F. H. 2003, *Astrophysical Journal*, 599, 363, doi: 10.1086/379243
- Alves, J. F., Lada, C. J., & Lada, E. A. 2001, *Nature*, 409, 159
- Andersson, B. G., Lazarian, A., & Vaillancourt, J. E. 2015, *Annual Review of Astron and Astrophys*, 53, 501, doi: 10.1146/annurev-astro-082214-122414
- Bai, X.-N. 2017, *Astrophysical Journal*, 845, 75, doi: 10.3847/1538-4357/aa7dda
- Bai, X.-N., & Stone, J. M. 2011, *Astrophysical Journal*, 736, 144, doi: 10.1088/0004-637X/736/2/144
- Balbus, S. A., & Hawley, J. F. 1991, *Astrophysical Journal*, 376, 214, doi: 10.1086/170270
- Barger, C. J., Lam, K. H., Li, Z. Y., et al. 2021, *Astronomy and Astrophysics*, 651, A43, doi: 10.1051/0004-6361/202039226
- Barnett, S. J. 1915, *Physical Review*, 6, 239, doi: 10.1103/PhysRev.6.239
- Bean, C. P., & Livingston, J. D. 1959, *Journal of Applied Physics*, 30, S120, doi: 10.1063/1.2185850
- Bergin, E. A., & Tafalla, M. 2007, *Annual Review of Astron and Astrophys*, 45, 339, doi: 10.1146/annurev.astro.45.071206.100404
- Blandford, R. D., & Payne, D. G. 1982, *Monthly Notices of the RAS*, 199, 883, doi: 10.1093/mnras/199.4.883

- Bonnor, W. B. 1956, *Monthly Notices of the RAS*, 116, 351, doi: 10.1093/mnras/116.3.351
- Bridson, R. 2007, in *ACM SIGGRAPH 2007 Sketches*, SIGGRAPH '07 (New York, NY, USA: Association for Computing Machinery), 22–es, doi: 10.1145/1278780.1278807
- Cassen, P., & Moosman, A. 1981, *Icarus*, 48, 353, doi: 10.1016/0019-1035(81)90051-8
- Chandrasekhar, S., & Fermi, E. 1953, *Astrophysical Journal*, 118, 113, doi: 10.1086/145731
- Chen, C.-Y., & Ostriker, E. C. 2014, *Astrophysical Journal*, 785, 69, doi: 10.1088/0004-637X/785/1/69
- . 2018, *Astrophysical Journal*, 865, 34, doi: 10.3847/1538-4357/aad905
- Chen, C.-Y., Storm, S., Li, Z.-Y., et al. 2019, *Monthly Notices of the RAS*, 490, 527, doi: 10.1093/mnras/stz2633
- Couch, S. M., Graziani, C., & Flocke, N. 2013, *Astrophysical Journal*, 778, 181, doi: 10.1088/0004-637X/778/2/181
- Cox, E. G., Harris, R. J., Looney, L. W., et al. 2018, *Astrophysical Journal*, 855, 92, doi: 10.3847/1538-4357/aaacd2
- Crutcher, R. M. 2012, *Annual Review of Astron and Astrophys*, 50, 29, doi: 10.1146/annurev-astro-081811-125514
- Dapp, W. B., Basu, S., & Kunz, M. W. 2012, *Astronomy and Astrophysics*, 541, A35, doi: 10.1051/0004-6361/201117876
- Desch, S. J. 2007, *Astrophysical Journal*, 671, 878, doi: 10.1086/522825
- Desch, S. J., & Connolly, H. C., J. 2002, *Meteoritics and Planetary Science*, 37, 183, doi: 10.1111/j.1945-5100.2002.tb01104.x
- DiDonato, A. R. 1982, *Mathematics of Computation*, 38, 547. <http://www.jstor.org/stable/2007289>

- Draine, B. T. 1996, in *Astronomical Society of the Pacific Conference Series*, Vol. 97, *Polarimetry of the Interstellar Medium*, ed. W. G. Roberge & D. C. B. Whittet, 16. <https://arxiv.org/abs/astro-ph/9603053>
- Draine, B. T. 2011, *Physics of the Interstellar and Intergalactic Medium* (Princeton University Press)
- Draine, B. T., & McKee, C. F. 1993, *Annual Review of Astron and Astrophys*, 31, 373, doi: 10.1146/annurev.aa.31.090193.002105
- Draine, B. T., Roberge, W. G., & Dalgarno, A. 1983, *Astrophysical Journal*, 264, 485, doi: 10.1086/160617
- Ebert, R. 1955, *Zeitschrift fuer Astrophysik*, 37, 217
- Evans, C. R., & Hawley, J. F. 1988, *Astrophysical Journal*, 332, 659, doi: 10.1086/166684
- Fiege, J. D., & Pudritz, R. E. 2000, *Astrophysical Journal*, 544, 830, doi: 10.1086/317228
- Frisch, P. C., Dorschner, J. M., Geiss, J., et al. 1999, *Astrophysical Journal*, 525, 492, doi: 10.1086/307869
- Fu, R. R., Weiss, B. P., Lima, E. A., et al. 2014, *Science*, 346, 1089, doi: 10.1126/science.1258022
- Galli, D., Lizano, S., Shu, F. H., & Allen, A. 2006, *Astrophysical Journal*, 647, 374, doi: 10.1086/505257
- Galli, D., & Shu, F. H. 1993, *Astrophysical Journal*, 417, 220, doi: 10.1086/173305
- Garrod, R. T., Widicus Weaver, S. L., & Herbst, E. 2008, *Astrophysical Journal*, 682, 283, doi: 10.1086/588035
- Goldsmith, P. F. 2001, *Astrophysical Journal*, 557, 736, doi: 10.1086/322255
- Gong, H., & Ostriker, E. C. 2011, *Astrophysical Journal*, 729, 120, doi: 10.1088/0004-637X/729/2/120

- . 2013, *Astrophysical Journal, Supplement*, 204, 8, doi: 10.1088/0067-0049/204/1/8
- Gong, M., & Ostriker, E. C. 2015, *Astrophysical Journal*, 806, 31, doi: 10.1088/0004-637X/806/1/31
- González-Casanova, D. F., & Lazarian, A. 2017, *Astrophysical Journal*, 835, 41, doi: 10.3847/1538-4357/835/1/41
- González-Casanova, D. F., Lazarian, A., & Santos-Lima, R. 2016, *Astrophysical Journal*, 819, 96, doi: 10.3847/0004-637X/819/2/96
- Goodman, A. A., Benson, P. J., Fuller, G. A., & Myers, P. C. 1993, *Astrophysical Journal*, 406, 528, doi: 10.1086/172465
- Gray, W. J., McKee, C. F., & Klein, R. I. 2018, *Monthly Notices of the RAS*, 473, 2124, doi: 10.1093/mnras/stx2406
- Hennebelle, P., Commerçon, B., Chabrier, G., & Marchand, P. 2016, *Astrophysical Journal, Letters*, 830, L8, doi: 10.3847/2041-8205/830/1/L8
- Hockney, R. W., & Eastwood, J. W. 1981, *Computer Simulation Using Particles* (McGraw-Hill International Book Company)
- Hosokawa, T., & Omukai, K. 2009, *Astrophysical Journal*, 691, 823, doi: 10.1088/0004-637X/691/1/823
- Hull, C. L. H., Le Gouellec, V. J. M., Girart, J. M., Tobin, J. J., & Bourke, T. L. 2020, *Astrophysical Journal*, 892, 152, doi: 10.3847/1538-4357/ab5809
- Hull, C. L. H., & Zhang, Q. 2019, *Frontiers in Astronomy and Space Sciences*, 6, 3, doi: 10.3389/fspas.2019.00003
- Hull, C. L. H., Girart, J. M., Tychoniec, Ł., et al. 2017, *Astrophysical Journal*, 847, 92, doi: 10.3847/1538-4357/aa7fe9
- Jin, M., Lam, K. H., McClure, M. K., et al. 2022, arXiv e-prints, arXiv:2207.04269. <https://arxiv.org/abs/2207.04269>

- Jones, D. C., Lam, K. H., Li, Z.-Y., & Tu, Y. 2022, *Monthly Notices of the RAS*, doi: 10.1093/mnras/stac1842
- Jones, R. V., & Spitzer, Lyman, J. 1967, *Astrophysical Journal*, 147, 943, doi: 10.1086/149086
- Joos, M., Hennebelle, P., Ciardi, A., & Fromang, S. 2013, *Astronomy and Astrophysics*, 554, A17, doi: 10.1051/0004-6361/201220649
- Jørgensen, J. K., Belloche, A., & Garrod, R. T. 2020, *Annual Review of Astron and Astrophys*, 58, 727, doi: 10.1146/annurev-astro-032620-021927
- Kataoka, A., Machida, M. N., & Tomisaka, K. 2012, *Astrophysical Journal*, 761, 40, doi: 10.1088/0004-637X/761/1/40
- Kataoka, A., Muto, T., Momose, M., Tsukagoshi, T., & Dullemond, C. P. 2016, *Astrophysical Journal*, 820, 54, doi: 10.3847/0004-637X/820/1/54
- Kataoka, A., Muto, T., Momose, M., et al. 2015, *Astrophysical Journal*, 809, 78, doi: 10.1088/0004-637X/809/1/78
- Kim, C.-G., & Ostriker, E. C. 2017, *Astrophysical Journal*, 846, 133, doi: 10.3847/1538-4357/aa8599
- Ko, C.-L., Liu, H. B., Lai, S.-P., et al. 2020, *Astrophysical Journal*, 889, 172, doi: 10.3847/1538-4357/ab5e79
- Kölligan, A., & Kuiper, R. 2018, *Astronomy and Astrophysics*, 620, A182, doi: 10.1051/0004-6361/201833686
- Krasnopolsky, R., & Königl, A. 2002, *Astrophysical Journal*, 580, 987, doi: 10.1086/343890
- Krasnopolsky, R., Li, Z.-Y., & Shang, H. 2010, *Astrophysical Journal*, 716, 1541, doi: 10.1088/0004-637X/716/2/1541
- Krasnopolsky, R., Li, Z.-Y., Shang, H., & Zhao, B. 2012, *Astrophysical Journal*, 757, 77, doi: 10.1088/0004-637X/757/1/77

- Kuffmeier, M., Haugbølle, T., & Nordlund, Å. 2017, *Astrophysical Journal*, 846, 7, doi: 10.3847/1538-4357/aa7c64
- Kuffmeier, M., Reissl, S., Wolf, S., Stephens, I., & Calcutt, H. 2020, *Astronomy and Astrophysics*, 639, A137, doi: 10.1051/0004-6361/202038111
- Kuiper, R., Klahr, H., Beuther, H., & Henning, T. 2010, *Astrophysical Journal*, 722, 1556, doi: 10.1088/0004-637X/722/2/1556
- Kunz, M. W., & Mouschovias, T. C. 2010, *Monthly Notices of the RAS*, 408, 322, doi: 10.1111/j.1365-2966.2010.17110.x
- Kuruwita, R. L., & Federrath, C. 2019, *Monthly Notices of the RAS*, 486, 3647, doi: 10.1093/mnras/stz1053
- Kwon, W., Stephens, I. W., Tobin, J. J., et al. 2019, *Astrophysical Journal*, 879, 25, doi: 10.3847/1538-4357/ab24c8
- Lam, K. H., Chen, C.-Y., Li, Z.-Y., et al. 2021, *Monthly Notices of the RAS*, 507, 608, doi: 10.1093/mnras/stab2105
- Lam, K. H., Li, Z.-Y., Chen, C.-Y., Tomida, K., & Zhao, B. 2019, *Monthly Notices of the RAS*, 489, 5326, doi: 10.1093/mnras/stz2436
- Larson, R. B. 1969, *Monthly Notices of the RAS*, 145, 271, doi: 10.1093/mnras/145.3.271
- Lazarian, A. 2007, *Journal of Quantitative Spectroscopy and Radiative Transfer*, 106, 225, doi: 10.1016/j.jqsrt.2007.01.038
- Lazarian, A., Eyink, G., Vishniac, E., & Kowal, G. 2015, *Philosophical Transactions of the Royal Society of London Series A*, 373, 20140144, doi: 10.1098/rsta.2014.0144
- Le Gouellec, V. J. M., Hull, C. L. H., Maury, A. J., et al. 2019, *Astrophysical Journal*, 885, 106, doi: 10.3847/1538-4357/ab43c2
- Le Gouellec, V. J. M., Maury, A. J., Guillet, V., et al. 2020, *Astronomy and Astrophysics*, 644, A11, doi: 10.1051/0004-6361/202038404

- Lee, J. W. Y., Hull, C. L. H., & Offner, S. S. R. 2017, *Astrophysical Journal*, 834, 201, doi: 10.3847/1538-4357/834/2/201
- Lewis, B. T., & Bate, M. R. 2018, *Monthly Notices of the RAS*, 477, 4241, doi: 10.1093/mnras/sty829
- Li, C., & Chen, X. 2019, *Astrophysical Journal, Supplement*, 240, 37, doi: 10.3847/1538-4365/aafdaa
- Li, P. S., McKee, C. F., & Klein, R. I. 2015, *Monthly Notices of the RAS*, 452, 2500, doi: 10.1093/mnras/stv1437
- Li, Z.-Y., Banerjee, R., Pudritz, R. E., et al. 2014a, *Protostars and Planets VI*, 173, doi: 10.2458/azu\_uapress\_9780816531240-ch008
- Li, Z.-Y., Krasnopolsky, R., & Shang, H. 2011, *Astrophysical Journal*, 738, 180, doi: 10.1088/0004-637X/738/2/180
- Li, Z.-Y., Krasnopolsky, R., Shang, H., & Zhao, B. 2014b, *Astrophysical Journal*, 793, 130, doi: 10.1088/0004-637X/793/2/130
- Li, Z.-Y., & McKee, C. F. 1996, *Astrophysical Journal*, 464, 373, doi: 10.1086/177329
- Lin, Z.-Y. D., Li, Z.-Y., Yang, H., et al. 2020, *Monthly Notices of the RAS*, 493, 4868, doi: 10.1093/mnras/staa542
- Mac Low, M.-M., Norman, M. L., Konigl, A., & Wardle, M. 1995, *Astrophysical Journal*, 442, 726, doi: 10.1086/175477
- Machida, M. N., Inutsuka, S.-I., & Matsumoto, T. 2011, *Publications of the ASJ*, 63, 555, doi: 10.1093/pasj/63.3.555
- Machida, M. N., Inutsuka, S.-i., & Matsumoto, T. 2014, *Monthly Notices of the RAS*, 438, 2278, doi: 10.1093/mnras/stt2343
- MacMillan, W. 1958, *The Theory of the Potential*, Dover books on physics, engineering No. pt. 2 (Dover Publications). <https://books.google.com/books?id=FqU8AAAAIAAJ>

- Martizzi, D., Quataert, E., Faucher-Giguère, C.-A., & Fielding, D. 2019, *Monthly Notices of the RAS*, 483, 2465, doi: 10.1093/mnras/sty3273
- Masson, J., Chabrier, G., Hennebelle, P., Vaytet, N., & Commerçon, B. 2016, *Astronomy and Astrophysics*, 587, A32, doi: 10.1051/0004-6361/201526371
- Masunaga, H., & Inutsuka, S.-i. 2000, *Astrophysical Journal*, 531, 350, doi: 10.1086/308439
- Masunaga, H., Miyama, S. M., & Inutsuka, S.-i. 1998, *Astrophysical Journal*, 495, 346, doi: 10.1086/305281
- Matsumoto, T., Machida, M. N., & Inutsuka, S.-i. 2017, *Astrophysical Journal*, 839, 69, doi: 10.3847/1538-4357/aa6a1c
- Maurý, A. J., Girart, J. M., Zhang, Q., et al. 2018, *Monthly Notices of the RAS*, 477, 2760, doi: 10.1093/mnras/sty574
- McKee, C. F., & Ostriker, E. C. 2007, *Annual Review of Astron and Astrophys*, 45, 565, doi: 10.1146/annurev.astro.45.051806.110602
- Mellon, R. R., & Li, Z.-Y. 2009, *Astrophysical Journal*, 698, 922, doi: 10.1088/0004-637X/698/1/922
- Morrish, A. H. 2001, *The Physical Principles of Magnetism* (R. E. Krieger Publishing Company)
- Mostefaoui, S., Kita, N. T., Togashi, S., et al. 2002, *Meteoritics and Planetary Science*, 37, 421, doi: 10.1111/j.1945-5100.2002.tb00825.x
- Müller, E., & Steinmetz, M. 1995, *Computer Physics Communications*, 89, 45, doi: 10.1016/0010-4655(94)00185-5
- Nakano, T., & Nakamura, T. 1978, *Publications of the ASJ*, 30, 671
- Okuzumi, S., Takeuchi, T., & Muto, T. 2014, *Astrophysical Journal*, 785, 127, doi: 10.1088/0004-637X/785/2/127
- Ossenkopf, V., & Henning, T. 1994, *Astronomy and Astrophysics*, 291, 943

- Padovani, M., Brinch, C., Girart, J. M., et al. 2012, *Astronomy and Astrophysics*, 543, A16, doi: 10.1051/0004-6361/201219028
- Pattle, K., & Fissel, L. 2019, *Frontiers in Astronomy and Space Sciences*, 6, 15, doi: 10.3389/fspas.2019.00015
- Penston, M. V. 1969, *Monthly Notices of the RAS*, 144, 425, doi: 10.1093/mnras/144.4.425
- Planck Collaboration, Ade, P. A. R., Aghanim, N., et al. 2015, *Astronomy and Astrophysics*, 576, A104, doi: 10.1051/0004-6361/201424082
- Purcell, E. M. 1979, *Astrophysical Journal*, 231, 404, doi: 10.1086/157204
- Purcell, E. M., & Spitzer, Lyman, J. 1971, *Astrophysical Journal*, 167, 31, doi: 10.1086/151002
- Reissl, S., Wolf, S., & Brauer, R. 2016, *Astronomy and Astrophysics*, 593, A87, doi: 10.1051/0004-6361/201424930
- Roberge, W. G., Degraff, T. A., & Flaherty, J. E. 1993, *Astrophysical Journal*, 418, 287, doi: 10.1086/173390
- Sadavoy, S. I., Myers, P. C., Stephens, I. W., et al. 2018a, *Astrophysical Journal*, 859, 165, doi: 10.3847/1538-4357/aac21a
- . 2018b, *Astrophysical Journal*, 869, 115, doi: 10.3847/1538-4357/aaef81
- Sadavoy, S. I., Stephens, I. W., Myers, P. C., et al. 2019, *Astrophysical Journal*, Supplement, 245, 2, doi: 10.3847/1538-4365/ab4257
- Sakai, N., Sakai, T., Hirota, T., et al. 2014, *Nature*, 507, 78, doi: 10.1038/nature13000
- Sakai, N., Oya, Y., Higuchi, A. E., et al. 2017, *Monthly Notices of the RAS*, 467, L76, doi: 10.1093/mnrasl/slx002
- Santos-Lima, R., de Gouveia Dal Pino, E. M., & Lazarian, A. 2012, *Astrophysical Journal*, 747, 21, doi: 10.1088/0004-637X/747/1/21

- Segura-Cox, D. M., Looney, L. W., Tobin, J. J., et al. 2018, *Astrophysical Journal*, 866, 161, doi: 10.3847/1538-4357/aaddf3
- Seifried, D., Banerjee, R., Pudritz, R. E., & Klessen, R. S. 2013, *Monthly Notices of the RAS*, 432, 3320, doi: 10.1093/mnras/stt682
- Shu, F. H. 1977, *Astrophysical Journal*, 214, 488, doi: 10.1086/155274
- . 1992, *The physics of astrophysics. Volume II: Gas dynamics.* (University Science Books)
- Shu, F. H., Galli, D., Lizano, S., & Cai, M. 2006, *Astrophysical Journal*, 647, 382, doi: 10.1086/505258
- Skinner, M. A., & Ostriker, E. C. 2015, *Astrophysical Journal*, 809, 187, doi: 10.1088/0004-637X/809/2/187
- Soler, J. D., Hennebelle, P., Martin, P. G., et al. 2013, *Astrophysical Journal*, 774, 128, doi: 10.1088/0004-637X/774/2/128
- Soler, J. D., Alves, F., Boulanger, F., et al. 2016, *Astronomy and Astrophysics*, 596, A93, doi: 10.1051/0004-6361/201628996
- Stehle, R., & Spruit, H. C. 2001, *Monthly Notices of the RAS*, 323, 587, doi: 10.1046/j.1365-8711.2001.04186.x
- Stephens, I. W., Dunham, M. M., Myers, P. C., et al. 2017, *Astrophysical Journal*, 846, 16, doi: 10.3847/1538-4357/aa8262
- . 2018, *Astrophysical Journal, Supplement*, 237, 22, doi: 10.3847/1538-4365/aacda9
- Stone, J. M., Gardiner, T. A., Teuben, P., Hawley, J. F., & Simon, J. B. 2008, *Astrophysical Journal, Supplement*, 178, 137, doi: 10.1086/588755
- Stone, J. M., Tomida, K., White, C. J., & Felker, K. G. 2020, *Astrophysical Journal, Supplement*, 249, 4, doi: 10.3847/1538-4365/ab929b
- Takahashi, S., Machida, M. N., Tomisaka, K., et al. 2019, *Astrophysical Journal*, 872, 70, doi: 10.3847/1538-4357/aaf6ed

- Tassis, K., & Mouschovias, T. C. 2005, *Astrophysical Journal*, 618, 783, doi: 10.1086/424480
- Tazaki, R., Lazarian, A., & Nomura, H. 2017, *Astrophysical Journal*, 839, 56, doi: 10.3847/1538-4357/839/1/56
- Thorne, K., & Blandford, R. 2021, *Plasma Physics: Volume 4 of Modern Classical Physics*, Modern Classical Physics (Princeton University Press). <https://books.google.com/books?id=IAEREAAAQBAJ>
- Tobin, J. J., Looney, L. W., Wilner, D. J., et al. 2015, *Astrophysical Journal*, 805, 125, doi: 10.1088/0004-637X/805/2/125
- Tobin, J. J., Looney, L. W., Li, Z.-Y., et al. 2016, *Astrophysical Journal*, 818, 73, doi: 10.3847/0004-637X/818/1/73
- Tomida, K., Machida, M. N., Hosokawa, T., Sakurai, Y., & Lin, C. H. 2017, *Astrophysical Journal, Letters*, 835, L11, doi: 10.3847/2041-8213/835/1/L11
- Tomida, K., Okuzumi, S., & Machida, M. N. 2015, *Astrophysical Journal*, 801, 117, doi: 10.1088/0004-637X/801/2/117
- Tomida, K., Tomisaka, K., Matsumoto, T., et al. 2013, *Astrophysical Journal*, 763, 6, doi: 10.1088/0004-637X/763/1/6
- Tomisaka, K. 2000, *Astrophysical Journal, Letters*, 528, L41, doi: 10.1086/312417
- Toomre, A. 1964, *Astrophysical Journal*, 139, 1217, doi: 10.1086/147861
- Troland, T. H., & Crutcher, R. M. 2008, *Astrophysical Journal*, 680, 457, doi: 10.1086/587546
- Truelove, J. K., Klein, R. I., McKee, C. F., et al. 1997, *Astrophysical Journal, Letters*, 489, L179, doi: 10.1086/310975
- Tsukamoto, Y. 2016, *Publications of the Astronomical Society of Australia*, 33, e010, doi: 10.1017/pasa.2016.6
- Tsukamoto, Y., Iwasaki, K., Okuzumi, S., Machida, M. N., & Inutsuka, S. 2015a, *Monthly Notices of the RAS*, 452, 278, doi: 10.1093/mnras/stv1290

- . 2015b, *Astrophysical Journal, Letters*, 810, L26, doi: 10.1088/2041-8205/810/2/L26
- Tu, Y., Li, Z.-Y., & Lam, K. H. 2022, *Monthly Notices of the Royal Astronomical Society*, doi: 10.1093/mnras/stac2030
- Ulrich, R. K. 1976, *Astrophysical Journal*, 210, 377, doi: 10.1086/154840
- Valdivia, V., Maury, A., Brauer, R., et al. 2019, *Monthly Notices of the RAS*, 488, 4897, doi: 10.1093/mnras/stz2056
- Vaytet, N., Commerçon, B., Masson, J., González, M., & Chabrier, G. 2018, *Astronomy and Astrophysics*, 615, A5, doi: 10.1051/0004-6361/201732075
- Wurster, J., Bate, M. R., & Price, D. J. 2018, *Monthly Notices of the RAS*, 480, 4434, doi: 10.1093/mnras/sty2212
- Wurster, J., & Li, Z.-Y. 2018, *Frontiers in Astronomy and Space Sciences*, 5, 39, doi: 10.3389/fspas.2018.00039
- Wurster, J., Price, D. J., & Bate, M. R. 2016, *Monthly Notices of the RAS*, 457, 1037, doi: 10.1093/mnras/stw013
- Yang, H. 2021, *Astrophysical Journal*, 911, 125, doi: 10.3847/1538-4357/abebde
- Yang, H., Li, Z.-Y., Looney, L., & Stephens, I. 2016, *Monthly Notices of the RAS*, 456, 2794, doi: 10.1093/mnras/stv2633
- Yang, H., Li, Z.-Y., Looney, L. W., Girart, J. M., & Stephens, I. W. 2017, *Monthly Notices of the RAS*, 472, 373, doi: 10.1093/mnras/stx1951
- Yen, H.-W., Zhao, B., Koch, P., et al. 2020, *Astrophysical Journal*, 893, 54, doi: 10.3847/1538-4357/ab7eb3
- Zhao, B., Caselli, P., Li, Z.-Y., & Krasnopolsky, R. 2018, *Monthly Notices of the RAS*, 473, 4868, doi: 10.1093/mnras/stx2617
- Zhao, B., Caselli, P., Li, Z.-Y., et al. 2016, *Monthly Notices of the RAS*, 460, 2050, doi: 10.1093/mnras/stw1124

Zhao, B., Li, Z.-Y., Nakamura, F., Krasnopolsky, R., & Shang, H. 2011, *Astrophysical Journal*, 742, 10, doi: 10.1088/0004-637X/742/1/10

Zucker, C., Speagle, J. S., Schlafly, E. F., et al. 2019, *Astrophysical Journal*, 879, 125, doi: 10.3847/1538-4357/ab2388